

Tailoring the electronic structure properties of carbon based materials

Citation for published version (APA):

Podaru, N. C. (2011). *Tailoring the electronic structure properties of carbon based materials*. [Phd Thesis 1 (Research TU/e / Graduation TU/e), Applied Physics and Science Education]. Technische Universiteit Eindhoven. <https://doi.org/10.6100/IR716667>

DOI:

[10.6100/IR716667](https://doi.org/10.6100/IR716667)

Document status and date:

Published: 01/01/2011

Document Version:

Publisher's PDF, also known as Version of Record (includes final page, issue and volume numbers)

Please check the document version of this publication:

- A submitted manuscript is the version of the article upon submission and before peer-review. There can be important differences between the submitted version and the official published version of record. People interested in the research are advised to contact the author for the final version of the publication, or visit the DOI to the publisher's website.
- The final author version and the galley proof are versions of the publication after peer review.
- The final published version features the final layout of the paper including the volume, issue and page numbers.

[Link to publication](#)

General rights

Copyright and moral rights for the publications made accessible in the public portal are retained by the authors and/or other copyright owners and it is a condition of accessing publications that users recognise and abide by the legal requirements associated with these rights.

- Users may download and print one copy of any publication from the public portal for the purpose of private study or research.
- You may not further distribute the material or use it for any profit-making activity or commercial gain
- You may freely distribute the URL identifying the publication in the public portal.

If the publication is distributed under the terms of Article 25fa of the Dutch Copyright Act, indicated by the "Taverne" license above, please follow below link for the End User Agreement:

www.tue.nl/taverne

Take down policy

If you believe that this document breaches copyright please contact us at:

openaccess@tue.nl

providing details and we will investigate your claim.

Tailoring the electronic structure properties of carbon based materials

Nicolae Cătălin Podaru

Tailoring the electronic structure properties of carbon based materials

Nicolae Cătălin Podaru

Tailoring the electronic structure properties of carbon based materials

PROEFSCHRIFT

ter verkrijging van de graad van doctor aan de
Technische Universiteit Eindhoven, op gezag van de
rector magnificus, prof.dr.ir. C.J. van Duijn, voor een
commissie aangewezen door het College voor
Promoties in het openbaar te verdedigen
op donderdag 13 oktober 2011 om 16.00 uur

door

Nicolae Cătălin Podaru

geboren te Iași, Roemenie

Dit proefschrift is goedgekeurd door de promotor:

prof.dr.ir. R.A.J. Janssen

Copromotor:

dr.ir. C.F.J. Flipse

This research was financially supported by NanoNed, the Nanotechnology network in The Netherlands.

Podaru, Nicolae Cătălin

Tailoring the electronic structure properties of carbon based materials / by Nicolae Cătălin Podaru. - Eindhoven, Technische Universiteit Eindhoven, 2011.
Proefschrift.

A catalogue record is available from the Eindhoven University of Technology Library
ISBN: 978-90-386-2730-4

NUR 924

Trefwoorden: rastertunnelmicroscopie / grafiet / koolstof nanobuizen / elektronische structuur / krachtmicroscopie / polystyreen / persisterende stroom

Subject headings: scanning tunneling microscopy / highly oriented pyrolytic graphite / carbon nanotubes / electronic structure / atomic force microscopy / polystyrene / persistent current

Printed by: Gildeprint Drukkerijen B.V., Enschede

Contents

1	Introduction	1
1.1	General introduction	1
1.2	Tailoring electronic structure properties	2
1.2.1	Our approach	3
1.2.2	Thesis outline	3
	Bibliography	4
2	Theoretical background	9
2.1	Highly oriented pyrolytic graphite	9
2.2	Single walled carbon nanotubes	15
2.3	Persistent currents in normal metal rings	21
2.4	Coulomb gap	23
2.5	Fano resonance	25
	Bibliography	26
3	Experimental	31
3.1	Scanning tunneling microscopy	31
3.2	Atomic force microscopy	35
3.3	Superconducting quantum interference device	36
3.4	Hall effect measurements	38
	Bibliography	41
4	The role of H-adsorbed atoms on graphite: zero bias anomaly in the density of electron states	43
4.1	Introduction	43
4.2	Sample preparation procedure	44
4.3	Experimental results and discussion	46
4.3.1	Hydrogen on HOPG. Topological effects	46
4.3.2	Changes in the LDOS of graphite induced by H	51
4.3.3	On the origin of the V-shaped gap and of the sharp localized state	60
4.4	Charge density/mobility measurements of hydrogen treated graphite	67
4.4.1	Experimental procedure	67
4.4.2	Experimental results and discussion	68
4.5	Conclusions	71

CONTENTS

Bibliography	73
5 Tailoring the electronic structure properties of single walled carbon nanotubes by H chemisorption	79
5.1 Introduction	79
5.2 Sample preparation procedure	80
5.2.1 Gold substrate preparation	80
5.2.2 Nanotube dispersion	81
5.2.3 Hydrogen deposition	82
5.3 Experimental results and discussion	82
5.3.1 Determining the chiral indexes of arc-discharge carbon nanotubes	82
5.3.2 Chemisorbed hydrogen on metallic CNT	86
5.3.3 Zero bias anomaly and Fano interference in hydrogen treated metallic SWCNT	91
5.3.4 Chemisorbed hydrogen on semiconducting CNT	101
5.4 Conclusions	103
Bibliography	104
6 Towards persistent current measurements on nanoscopic gold rings	107
6.1 Introduction	107
6.2 Experimental	108
6.3 AFM studies of polystyrene particles and gold nanostructures	109
6.3.1 AFM characterization of the polystyrene particles	109
6.3.2 AFM characterization of gold nano-structures	111
6.4 DC SQUID measurements on ensemble of gold rings	115
6.5 Discussion	116
6.6 Conclusions and remarks	119
Bibliography	120
Summary	123
Samenvatting	125
Acknowledgements	127
Curriculum Vitae	129

Chapter 1

Introduction

1.1 General introduction

The nanoscopic electronic and vibrational structure properties of single crystal materials determine most of their physical properties, like for example thermal conductivity, magnetic ordering, electrical conductivity, melting temperature, and hardness. Tailoring the electronic and vibrational structure properties of known materials, different physical properties can be enhanced. One of the methods to modify the electronic structure properties of a bulk material is by doping. For example, doping high purity semiconductor materials with foreign atomic species resulted in a revolution of electronic devices, causing a complete transition from vacuum tube electronic components to all solid-state electronic components. It enhances devices such as diodes, transistors, light-emitting diodes and thyristors and ultimately allows integrating millions of electronic elements in the same volume as occupied by a vacuum tube component. In addition to nanoscale controllable electronic and vibrational properties of materials, the performance has been increased by the miniaturization of the electronic devices. Miniaturization enables integration of electronic devices and increases the device performance, i.e. operating frequency of microprocessors.

Carbon, a vastly present chemical element and a life building block, has been studied in detail along the years. Maybe one of its most startling allotropic forms is diamond. It has the largest hardness and the highest thermal conductivity of any bulk material. In addition, diamond presents a band gap of 5.5 eV thus transmitting the entire spectrum of visible light, making it in appearance colorless. These excellent optical and mechanical characteristics made diamond the most popular gemstone. With physical properties vastly different from diamond, graphite conducts electricity, and is soft. It is widely used in industry, from a simple lubricant material to neutron-moderator in nuclear power plants. The wide range of physical properties governing

1. Introduction

the carbon allotropes can be explained by looking at the chemical bonding. Carbon has four valence electrons in the $2s^2p^2$ -configuration and two electrons in the $1s$ -orbital. To form bonds, C atoms undergo hybridization. Three configurations are possible, sp - (i.e. acetylene), sp^2 - (i.e. graphite), and sp^3 - (i.e. diamond). The variety of hybridized states available allows carbon to be present in numerous molecular and crystalline structures.

Carbon based materials have been the first to be synthesized in all possible dimensions, from three-dimensional to zero-dimensional. Carbon nanotubes, fullerenes and ultimately graphene provided researchers the possibility to study and compare various electronic effects function of material physical dimensionality. Carbon based materials also present exotic physical effects, such as: Klein tunneling (graphene [1]), anomalous half-integer quantum Hall effect (graphene [2]), minimal conductivity at the neutrality point (graphene [2]), superconductivity upon alkali metal doping (graphite and fullerenes [3–5]) and others.

1.2 Tailoring electronic structure properties

The electronic structure properties of bulk materials are influenced by the so-called crystallographic defects. They represent symmetry breaking elements, deviations of the regular crystallographic structure (unit cell). There are three major groups of crystallographic defects: point defects, planar defects and bulk defects. Understanding the influence of crystallographic defects on the electronic structure properties of (poly-) crystalline materials, such as carbon-based materials, is a necessary requirement if these materials are to be used for possible future electronic devices. There are several types of point crystallographic defects: vacancy defects, interstitial defects, Frenkel defects, antisite defects and topological defects (Stone-Wales defects in nanotubes). Various theoretical studies have addressed the influence of point defects and extended defects in graphene, carbon nanotubes and graphite [6–25]. In general, point defects in the C honeycomb lattice give rise to quasi-localized electronic states at the Fermi level [6, 17]. The spatial extent of these electronic states is several nanometers around the defect site while forming the well known $(\sqrt{3} \times \sqrt{3})R30^\circ$ superstructure on both graphite and graphene [26–29, 32]. Point defects can be produced in graphite, graphene or carbon nanotubes by ion bombardment [30–32]. Ion bombardment induced defects are, in our estimate, hard to describe since except C atom removal from the lattice, defects such as Stone-Wales or un-saturated dangling bonds or foreign chemisorbed species (i.e. hydrogen) can saturate some of the dangling bonds. Thus, studying the role of point defects in carbon-based materials can be rather subjective of bombardment energy and experimental conditions.

1.2.1 Our approach

Since ion bombardment of carbon-based materials can create mixtures of point defects, we used a different approach to test the influence of point defects on carbon-based materials. Thus, instead of kicking out carbon atoms from the crystallographic structure, hydrogen will be chemisorbed on the carbon-based materials. The work of Hornakær et al. on H deposited on highly oriented pyrolytic graphite (HOPG) revealed the possibility of controllably creating metastable structures of atomic hydrogen on graphite (0001) [33]. However, their work did not investigate the electronic effects induced by hydrogen bonding on the graphite surface. We considered these well-defined structures suitable for studying the role of chemisorbed species on carbon-based materials. The same method of hydrogen deposition has been employed to study the electronic effects on single walled carbon nanotubes (SWCNT).

The aim of this thesis is to study the role of chemisorbed hydrogen on the electronic structure properties of highly oriented pyrolytic graphite and single walled carbon nanotubes. The study uses scanning tunneling microscopy in ultra high vacuum, at temperatures ranging from 5 K up to 120 K. The hydrogen coverage was varied between 0.01 and 0.2 monolayers for H chemisorbed on HOPG while it was maintained low for H chemisorbed on SWCNT.

Unrelated to the tailoring of the electronic structure properties of carbon based materials, we aimed to open a new path for bridging the gap between theory and experimental results related to the phenomenon of persistent currents in normal metal (gold) rings [34–44]. Our approach is to create nanoscopic rings by means of colloidal lithography [45] with a perimeter with the same order of magnitude as the mean free electron path in gold.

1.2.2 Thesis outline

Chapter 2 provides the reader with a short theoretical background on the electronic and vibrational structure properties of HOPG and SWCNT. In addition a short description of the Fano resonance and the Coulomb gap is given. The phenomenon of persistent currents is also summarized, with an emphasis on the experimental results obtained by other groups. *Chapter 3* describes the techniques used to study the effects mentioned above. Atomic force microscopy (AFM), scanning electron microscopy (SEM) and superconducting quantum interference device (SQUID) measurements were used to study the Au nano-structures while scanning tunneling microscopy and Hall effect measurements were well-suited to investigate the influence of chemisorbed hydrogen on HOPG and SWCNT.

Having established in Chapters 2 and 3 the theoretical and experimental background, the following chapters of this thesis summarize the obtained results. *Chap-*

1. Introduction

ter4 presents the changes in the local density of states of graphite upon hydrogen chemisorption. Peculiar changes in the local density of states (LDOS) are appearing at the Fermi level. Depending mainly on the system temperature and hydrogen coverage, the LDOS presents a pseudo V-shaped gap or Fano lineshape. In addition to these peculiar observations in the LDOS, on top of hydrogen islands (large coverage hydrogen condition) adsorbed on graphite it is shown that a band gap is obtained. In addition we will show that the hydrogen deposition method used does not induce any distinguishable levels of other type of point defects. Continuing the work presented in Chapter 4, we aimed to test if the results obtained on H chemisorbed on HOPG can be reproduced if on metallic SWCNT. *Chapter 5* describes these results. It will be shown that upon hydrogen chemisorption several effects can be observed. At large hydrogen coverage deposited on metallic SWCNT a metal to insulator transition is noticed, result in good agreement with studies of high H coverage on HOPG. Confined electronic states have also been observed between two large hydrogen patches. Other peculiar states have been observed around the Fermi level in the vicinity of small patches of hydrogen. If the SWCNT is semiconducting, upon hydrogen chemisorption it was noticed in the LDOS that an additional electronic states are developing in the intrinsic band gap of the SWCNT, reducing it.

The last chapter of this thesis, *Chapter 6*, describes the advantages and limitations given by the colloidal lithography when used to produce metallic rings intended to study the phenomenon of persistent currents. Although persistent currents have not been measured, this chapter may provide useful experimental guidelines for future endeavors. It will be shown that large arrays of Au nano-structures have been successfully produced, while the diameter of such a structure is less than 19 nanometers. Direct current SQUID measurements up to 5 T were performed but the results indicate both diamagnetic and paramagnetic behavior of these ensembles of Au nano-structures.

Bibliography

- [1] M.I. Katsnelson, K.S. Novoselov, and A.K. Geim. *Nature Physics* 1, 620 (2006).
- [2] K.S. Novoselov, A.K. Geim, S.V. Morozov, D. Jiang, Y. Zhang, S.V. Dubonos, and A.A. Firsov. *Nature* 438, 917 (2005).
- [3] T.E. Weller, M. Ellerby, S.S. Saxena, R.P. Smith, and N.T. Skipper. *Nature Physics* 1, 39 (2005).
- [4] A.F. Hebard, M.J. Rosseinsky, R.C. Haddon, D.W. Murphy, S.H. Glarum, T.T.M. Palstra, A.P. Ramirez, and A.R. Kortan. *Nature* 350, 600 (1991).

- [5] R.C. Haddon, A.F. Hebard, M.J. Rosseinsky, D.W. Murphy, S.J. Duclos, K.B. Lyons, B. Miller, J.M. Rosamilia, R.M. Fleming, A.R. Kortan, S.H. Glarum, A.V. Makhija, A.J. Muller, R.H. Eick, S.M. Zahurak, R. Tycko, G. Daddagh, and F.A. Thiel. *Nature* 350, 320 (1991).
- [6] N.M.R. Peres, F. Guinea, and A.H.C. Neto. *Phys. Rev. B* 72, 174406 (2005).
- [7] N.M.R. Peres, F. Guinea, and A.H.C. Neto. *Phys. Rev. B* 73, 125411 (2006).
- [8] R.Y. Oeiras, F.M. Araújo-Moreira, N. Veríssimo-Alves, R. Faccio, H. Pardo, and A.W. Mombrú. arXiv:0606533 (2006).
- [9] R. Faccio, H. Pardo, P.A. Denis, R.Y. Oeiras, F.M. Araújo-Moreira, M. Veríssimo-Alves and A.W. Mombrú. *Phys. Rev. B* 77, 035416 (2008).
- [10] J.J. Palacios, J. Fernández-Rossier, and L. Brey. *Phys. Rev. B* 77, 195428 (2008).
- [11] L. Pisani, B. Montanari, and N.M. Harrison. *New J. Phys.* 10, 033002 (2008).
- [12] V.M. Pereira, F. Guinea, J.M.B. Lopes dos Santos, N.M.R. Peres, and A.H. Castro Neto. *Phys. Rev. Lett.* 96, 036801 (2006).
- [13] V.M. Pereira, F. Guinea, J.M.B. Lopes dos Santos, N.M.R. Peres, and A.H. Castro Neto. *Phys. Rev. B* 77, 115109 (2008).
- [14] H. Amara, S. Latil, V. Meunier, Ph. Lambin, and J.-C. Charlier. *Phys. Rev. B* 76, 115423 (2007).
- [15] A.A. El-Barbary, R.H. Telling, C.P. Ewels, M.I. Heggie, and P.R. Briddon. *Phys. Rev. B* 68, 144107 (2003).
- [16] Y. Ferro and A. Allouche. *Phys. Rev. B* 75 155438 (2007).
- [17] P.O. Lehtinen, A.S. Forester, Y. Ma, A.V. Krasheninnikov, and R.M. Nieminen. *Phys. Rev. Lett.* 93, 187202 (2004).
- [18] O.V. Yazyev and L. Helm. *Phys. Rev. B* 75, 125408 (2007).
- [19] T.O. Wehling, A.V. Balatsky, M.I. Katsnelson, A.I. Lichtenstein, K. Scharnberg, and R. Wiesendanger. *Phys. Rev. B* 75, 125425 (2007).
- [20] T. Maltezopoulos, A. Kubetzka, M. Morgenstern, R. Wiesendanger, S.G. Lemay, and C. Dekker. *Appl. Phys. Lett.* 83, 1011 (2003).
- [21] L.C. Venema, J.W.G. Wildoer, J.W. Janssen, S.J. Tans, H.L.J. Temminck Tuinstra, L.P. Kouwenhoven, and C. Dekker. *Science* 283, 52 (1999).

1. Introduction

- [22] O. Gulseren, T. Yildirim, and S. Ciraci. *Phys. Rev. B* 65, 153405 (2002).
- [23] E. Mariani, L.I. Glazman, A. Kamenev, and F. von Oppen. *Phys. Rev. B* 76, 165402 (2007).
- [24] X. Sha and B. Jackson. *Surf. Sci.* 496, 318 (2001).
- [25] D.W. Boukhvalov, M.I. Katsnelson, and A.I. Lichtenstein. *Phys. Rev. B* 77, 035427 (2008).
- [26] H.A. Mizes and J.S. Forester. *Science* 244, 559 (1989).
- [27] K.F. Kelly, D.Sarkar, G.D. Hale, S.J. Oldenburg, and N.J. Halas. *Science* 273, 1371 (1996).
- [28] J.G. Kushmerick, K.F. Kelly, H.-P. Rust, N.J. Halas, and P.S. Weiss. *Phys. Chem. B* 103, 1619 (1999).
- [29] P. Ruffieux, O. Groning, P. Schwaller, L. Schlapbach, and P. Groning. *Phys. Rev. Lett.* 84, 4910 (2000).
- [30] K. Mochiji, S. Yamamoto, H. Shimizu, S. Ohtani, T. Seguchi, and N. Kobayashi. *J. Appl. Phys.* 82, 6037 (1997).
- [31] D. Marton, H. Bu, K.J. Boyd, S.S. Todorov, A.H. Al-Bayati, and J.W. Rabalais. *Surf. Sci.* 326, L489 (1995).
- [32] T. Kondo, Y. Honma, J. Oh, T. Machida, and J. Nakamura. *Phys. Rev. B* 82, 153414 (2010).
- [33] L. Hornakær, E. Rauls, W. Xu, Ž. Šljivančanin, R. Otero, I. Stensgaard, E. Lægsgaard, B. Hammer, and F. Besenbacher. *Phys. Rev. Lett.* 97, 186102 (2006).
- [34] M. Buttiker, Y. Imry, R. Landauer, and S. Pinhas. *Phys. Rev. B* 31, 6207 (1985).
- [35] L.P. Lévy, G. Dolan, J. Dunsmuir, and H. Bouchiat. *Phys. Rev. Lett.* 64, 2074 (1990).
- [36] V. Chandrasekhar, R.A. Webb, M.J. Brandy, M.B. Ketchen, W.J. Gallagher, and A. Kleinsasser. *Phys. Rev. Lett.* 67, 3578 (1991).
- [37] B. Reulet, M. Ramin, H. Bouchiat and D. Mailly. *Phys. Rev. Lett.* 75, 124 (1995).
- [38] E.M.Q. Jariwala, P. Miahanty, M.B. Ketchen, and R.A. Webb. *Phys. Rev. Lett.* 86, 3124 (2001).

- [39] W. Rabaut, L. Saminadayar, D. Mailly, K. Hasselbach, A. Benot, and B. Etienne. *Phys. Rev. Lett.* 102, 136802 (2009).
- [40] R. Deblock, R. Bel, B. Reulet, H. Bouchiat, and D. Mailly. *Phys. Rev. Lett.* 89, 206803 (2002).
- [41] D. Mailly, C. Chapelier, and A. Benoit. *Phys. Rev. Lett.* 70, 2020 (1993).
- [42] M. Buttiker, Y. Imry, and R. Landauer. *Phys. Lett. A* 96, 365 (1983).
- [43] H. Bluhm, N.C. Koshnick, J.A. Bert, M.E. Huber, and K.A. Moler. *Phys. Rev. Lett.* 102, 136802 (2009).
- [44] A.C. Bleszynski-Jaych, W.E. Shanks, B. Peaudecerf, E. Ginossar, F. von Oppen, L. Glazman, and J.G.E. Harris. *Science* 362, 272 (2009).
- [45] P. Hanarp, and J. Aizpurua. *Phys. Rev. Lett.* 90, 057401 (2003).

Chapter 2

Theoretical background

2.1 Highly oriented pyrolytic graphite

Highly oriented pyrolytic graphite, HOPG, is a highly ordered form of pyrolytic graphite with an angular spread of the c -axis of the crystallites of less than 1 degree [1]. HOPG is usually produced by stress annealing amorphous carbon at approximately 3300 K. Stress annealing implies that during the annealing procedure, mechanical pressure is applied to the precursor material. For HOPG, the pressure is applied uni-axially, the c -axis of the HOPG. A common use of HOPG is to test and calibrate surface sensitive techniques like AFM and STM since cleaving the sample with scotch tape can easily produce an atomically flat surface. HOPG is not only a suitable test sample but it is also attractive to the scientific community for various scientific studies as: superconductivity [2], metal-insulator transition [3], studies of quasiparticles and Dirac fermions [4], electron scattering effects around impurities or defects [5, 9], and electron-electron correlations [10].

Carbon materials in an ordered form are available in all the spatial dimensions, under the following categories: fullerenes (zero-dimensional), carbon nanotubes (one dimensional), graphene (two dimensional) and HOPG (three dimensional). Graphene is the first 2D material available to scientists. It consists of a sheet of sp^2 bonded carbon atoms, as visible in Figure 2.1a. All above-mentioned materials can be geometrically built from graphene. Thus, making a cage from graphene reveals a fullerene. If one rolls a sheet of graphene the carbon nanotubes can be constructed. Stacking graphene layers one on top of each other produces graphite. If the stacking is made along the c -axis of the graphene sheets, then HOPG is obtained. The stacking of the graphene layers is done following the ABAB periodicity. To understand what the ABAB periodicity means, note that Figure 2.1b indicates two non-equivalent atomic positions. Consider the top graphene layer from Figure 2.1b. The A site (also called

2. Theoretical background

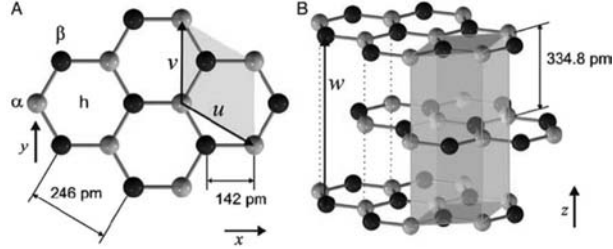


Figure 2.1: a) graphene with the lattice constant equal to 2.46 Å, marked in red are the β sites while in grey are marked the α sites. b) The unit cell of graphite depicted in green with the inter-planar distance the the HOPG crystal equal to 334.8 pm.

α site is marked in grey) has a C atom underneath, in the adjacent layer, while the B site (β site, marked in red) has no C atom underneath. The ABAB stacking of the graphene layers depletes the charge density at the Fermi level of the α sites due to the weak van der Waals forces, thus only the β sites are visible in STM imaging [6].

Electronic and vibrational structure properties of HOPG

The electronic structure properties of HOPG (0001) have been investigated both experimentally and theoretically [7]. Ooi et. al have shown, by LDA calculations, that the total density of states of HOPG within 1 eV around the Fermi level is parabolic. This can be observed in Figure 2.2a. It is important to mention that most of our scanning tunneling spectroscopy (STS) investigations of the DOS of graphite are made between - 0.5 eV and + 0.5 eV. In order to verify the similitude between the results of calculations and the experimental results, STS was conducted on HOPG (0001) far away from structural defects or step edges, since it is known that these features introduce localized states [8]. A typical graphite STS is presented in Figure 2.2b. The small overlap between the conduction band and the valance band in HOPG makes this material a semimetal. Furthermore, Hall measurements function of temperature indicate that the charge density in HOPG decreases when the temperature of the material is decreased. Also, anomalies have been mentioned while measuring the Hall effect in graphite [11] related to exciton pairing driven by magnetic field. It is also important to mention that HOPG is a layered compound. The electron mass $m_{e\perp} \gg m_{e\parallel}$, in literature [23] it can be found that $m_{e\perp} \simeq 10m_0$ and $m_{e\parallel} \simeq 0.05m_0$, m_0 is the electron rest mass. It can be considered that graphite is a quasi two dimensional material. The electron transport in graphite occurs mainly in each plane of the HOPG due to the hexagonal networks of overlapped π - orbitals. This type of charge carrier transport, especially at low temperature hints towards a quasi 2D

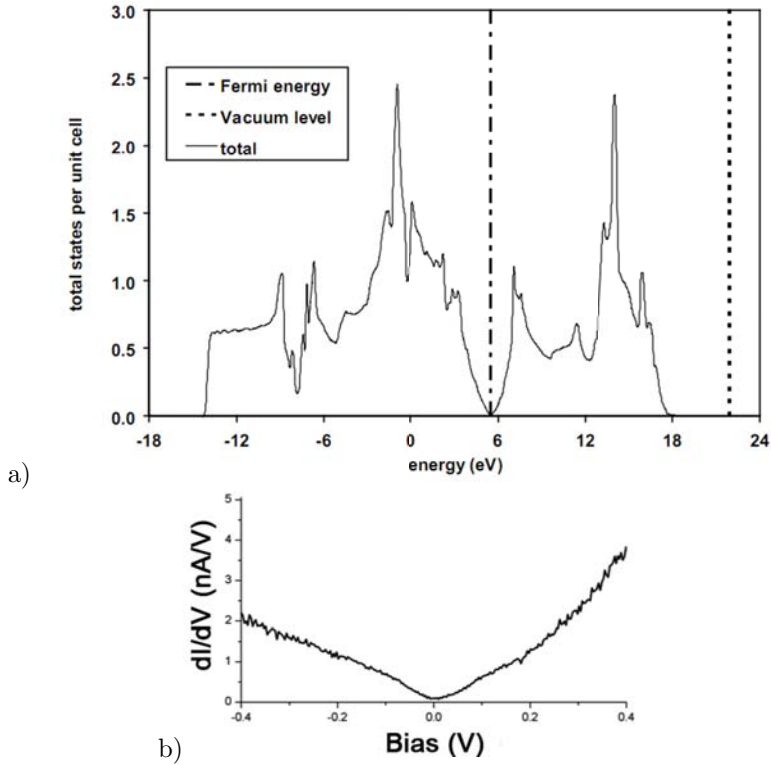


Figure 2.2: a) LDA calculation for graphite indicating a smooth parabolic DOS around the Fermi level, with a small finite value at it [7]. b) Similar to a), experimentally a smooth DOS is obtained from STS measurements, measurement parameters: $V_{ref\ RMS} = 6\text{ mV}$, $f = 730\text{ Hz}$.

2. Theoretical background

Table 2.1: Phonon modes in graphite

Phonon mode	DFT-LDA (meV)	Experimental (HREELS, STM-IETS)(meV)
ZA(Γ)	15	16
ZA(M)	59	57, 58
ZO (M)	78	81
SH(M)	77	100
ZO(Γ)	109	108, 111
LA(K)	124	134, 137
SH(M)	177	172, 180
LO(Γ)	197-202	198-205

charge carrier transport.

The phonon modes of graphite were investigated by high resolution electron energy loss spectroscopy (HREELS) [12–16] and inelastic scanning tunneling spectroscopy (IETS) [17]. The experimental results and density functional theory [17] calculations are summarized to the results depicted in Table 2.1, where Z stands for out of plane, S for shear, A for acoustical and O for optical. The phonon modes have been calculated and measured for all three symmetry points: Γ , K and M. As it can be observed, a good agreement between experimental work and theoretical work has been achieved. The IETS measurements were performed at 6.5 K. Another contribution to the IET spectrum was identified as the plasmon mode of graphite, found at 40 meV, observable in Figure 2.3. In the free electron model the energy of the plasmon energy can be expressed as follows: $E_p = \hbar \sqrt{\frac{ne^2}{m\epsilon_0}}$ and it can be seen that the plasmon energy is directly proportional with the square root electron density n and inverse proportional with the square root of the electron mass, m . Since the electron mass can be considered constant within a small temperature variation, the only variable that can produce an energy shift of the plasmon at 40 meV is the change in the electron concentration with temperature. In metals the electron density is several orders of magnitude larger than in graphite, the plasmon energy is located usually at more than 15 eV. Since the conduction electrons are at the E_F , the interaction between the plasmon and the conduction electrons is not influencing the conduction properties of the metal.

HOPG modified by structural defects or chemisorbed species

HOPG, as any other material, does not come defect-free. Although the density of structural defects (Stone-Wales, missing atoms) on flat atomic terraces is rather low both experimental and theoretical research show for graphite or graphene unexpected phenomena as ferromagnetism [18, 19]. Since the density of structural defects on native HOPG is low, low energetic or high energetic ion bombardment of the graphitic

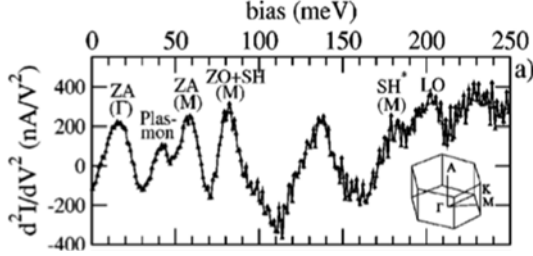


Figure 2.3: Inelastic tunneling spectrum of HOPG. The inelastic excitations due to the plasmon or the phonon modes are peaks in the d^2I/dV^2 [17].

surface has been used to create structural defects [9, 20]. The point defects obtained with low energy hydrogen ions [9] are creating charge density oscillations due to the interference of electron waves. This effect, as described by Ruffieux et. al. [9], has three fold symmetry and is still present at 20 up to 25 lattice constants. It was concluded that the presence of a single scattering center on the top layer of graphite creates long-range electronic effects. However, if the number of structural defects and/or foreign chemisorbed atoms (hydrogen in the case of Ruffieux et. al.) is increased, more complicated electronic patterns appear on the top graphite layer due to multiple electron scattering on these defects/chemisorbed species. It was also found that if a single H atom is chemisorbed on a β site, due to the electron scattering the charge density on the adjacent α sites is increased, making the α sites visible to STM topography imaging. This observation implies that around such a chemisorbed H atom the DOS of graphite is drastically modified since also the α sites are visible. Another STS study done by Niimi et. al. [21] involving zigzag and armchair step edges that are presumably H terminated, revealed a clear peak in the LDOS at negative bias voltages from -100 to -20 mV close to the zigzag edges, while such a peak was not observed near the armchair edge. This peak was associated with an edge state theoretically predicted by Fujita et. al. [22]. The edge state is no longer visible 5 nm away from the step edge. Due to the presence of the edge state in the LDOS of graphite, all the STS characterization of hydrogenated HOPG in this thesis is done at least 20 nm away from the step edges or grain boundaries.

Hydrogen is the simplest atom to model in theoretical calculations and hence the structural effects of H or D chemisorption on HOPG have been intensively studied. First of all, according to the Born-Oppenheimer approximation H and D are indistinguishable and therefore it can be assumed that their chemical reactivities are identical. That is why, in the rest of this thesis, unless mentioned otherwise, the discussion is valid for both hydrogen and deuterium. Several works calculated the

2. Theoretical background

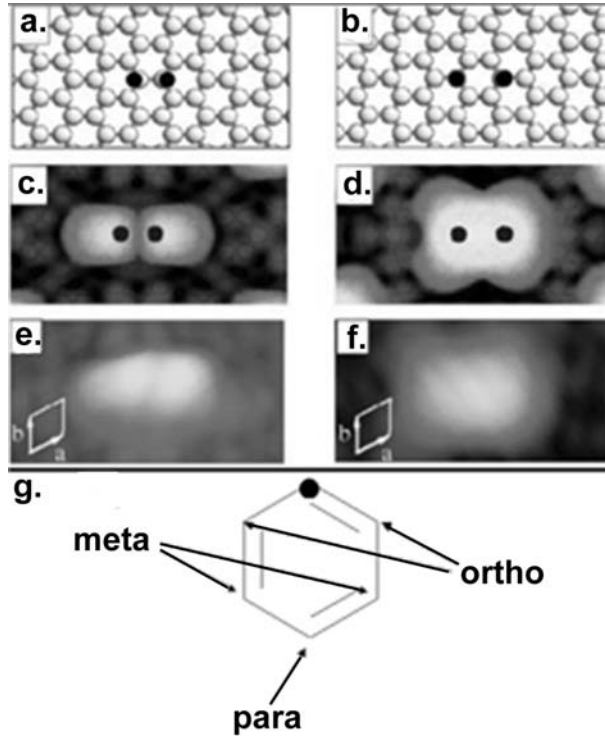


Figure 2.4: The black circles depict the H atomic positions on the graphite lattice for: a) dimer A. b) dimer B. STM simulated topography result from DFT calculations depicting c) dimer A. d) dimer B. STM topography images of: e) Cigar shaped structure similar to dimer A. f) Squared shape topographical observation corresponding to dimer B as expected from d) [27].

hydrogen adsorption energies [24–26] for various positions on the graphite lattice and it has been found that the preferential site for H adsorption is the top position of the C atom constituting the graphite lattice. Bonding a single H atom to a C atom from the graphite lattice changes locally the sp^2 character of the bonded C atom in an sp^3 character. Surface relaxation also occurs and LDA calculations [26] have shown the puckering of the bonded C atom above the surface plane with 0.3 \AA . Another effect of the surface relaxation is the modification of several bond lengths and bond angles around the hydrogen functionalized carbon from the graphite plane. These effects have also been shown on graphene [25].

STM studies of H chemisorbed on graphite were conducted in order to study eventual recombination pathways for the hydrogen [27]. Metastable structures consisting of two hydrogen atoms chemisorbed were identified with the help of simulated STM

images from DFT calculations. The agreement between experiment and theory can be observed in Figure 2.4, where the shape of the two type of dimers (A and B) closely match. Temperature programmed desorption (TPD) experiments reveal that dimer A is more stable than dimer B, since the desorption temperature for dimer A is higher than for dimer B (600 K in comparison to 475 K). To understand the formation of the metastable structures, Hornekær et al. [27] found theoretically and proven experimentally that if a single H is chemisorbed on C, the adsorption barrier for another H atom is almost vanishing for two positions of the HOPG hexagonal lattice. The positions are ortho (dimer A) and para (dimer B) in respect to the first chemisorbed hydrogen, thus explaining the presence of metastable structures. In Figure 2.4g, a schematic representation of the ortho, meta and para positions is depicted in respect to a radical, named B in a benzene ring.

Chapter 4 will present and discuss the modification of the electronic structure properties in the vicinity (less than 12 nm away) of the hydrogen patches at various temperatures. It will be shown that modifications of the LDOS of HOPG in the proximity of H patches are temperature dependent and H coverage dependent. Furthermore, the topological change of the HOPG surface upon hydrogen chemisorption will be presented.

2.2 Single walled carbon nanotubes

The discovery of carbon nanotubes, first reported by Sumio Iijima in 1995 [28] was a result of the extensive research initiated by the discovery and synthesis of the C_{60} molecule. Carbon nanotubes were first suggested by M. Dresselhaus at the Workshop of Fullerenes and Solid State Derivates, Philadelphia, US, 2-3 August 1991 [29]. The first carbon nanotubes were produced with the arc-discharge method. Other methods to produce carbon nanotubes are: laser ablation [30], chemical vapor deposition (CVD) [31], a variation of the CVD method CoMoCat (where the abbreviation is a compilation of cobalt, molybdenum and catalytic) [32–34] and HiPCO (high pressure CO conversion) [35]. A carbon nanotube is defined by its chiral vector C , which indicates the way a graphene sheet is rolled up. The chiral vector is usually defined in terms of the unit vectors a_1 and a_2 of the honeycomb graphene lattice in such a way that $C = n \cdot a_1 + m \cdot a_2$. Due to symmetry n and m must satisfy $0 \leq m \leq n$.

The tube diameter and the chiral angle of the nanotubes can be expressed by the indices m and n , denoted as (n, m) . As a function of the chirality index (n, m) three classes of nanotubes can be identified as: armchair (n, n) , zigzag $(n, 0)$ and chiral (n, m) (Figure 2.5). If the geometrical structure of the carbon nanotubes is known, the electronic properties of the carbon nanotubes can be calculated with the tight binding

2. Theoretical background

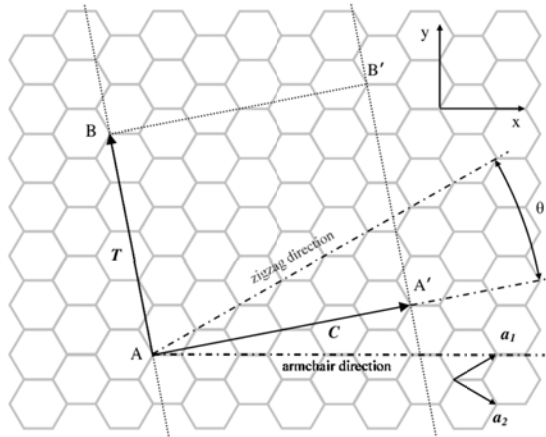


Figure 2.5: The chiral vector C defined on an unrolled honeycomb lattice. To construct the nanotube from the chiral vector, site A and A' as well as site B and B' on the lattice should be connected, resulting in a (4,2) nanotube in this case. Vector T is the translation vector, giving the length of the unit cell.

approximation, that does give results consistent with experiments [36–38]. From the calculation, the DOS of the nanotubes can be obtained as depicted in Figure 2.6. For example, a nanotube with the chiral index (4,4) the crossing of the bands near the Fermi level yields a small and constant DOS, while further away from the Fermi level the one-dimensional nature of the energy bands lead to van Hove singularities (VHS). If there is no crossing at the Fermi level of the bands then a zero-density of states will appear in the DOS. This means that there is an energy gap, E_{gap} , equal to the distance between the first two van Hove singularities. This band gap is also shown in Figure 2.7. Zigzag nanotubes are usually semiconducting tubes, except for the tubes with a chiral index $(n, 0)$ with n a multiple of 3. This condition originates from the fact that when k is in the circumferal direction it is equal to a multiple of $\frac{2\pi}{3a}$, one of the cross sections is crossing the K-point. The complete classes of armchair tubes are metallic tubes while the chiral tubes exist in both regimes, semiconducting and metallic. Chiral tubes are metallic when the chiral indices $2n + m$ is a multiple of 3. Also, the metallic zigzag and all armchair nanotubes satisfy the same condition. A simple map for small-diameter nanotubes indicating the metallic or semiconducting character is shown in Figure 2.8 [40].

So far, the electronic structure properties of carbon nanotubes were discussed in the isolated and ideal case. However, in order to correctly predict the electronic structure properties during STM experiment, for example, one must consider the nanotube-substrate interaction. Since in this thesis only CNTs on gold surface were

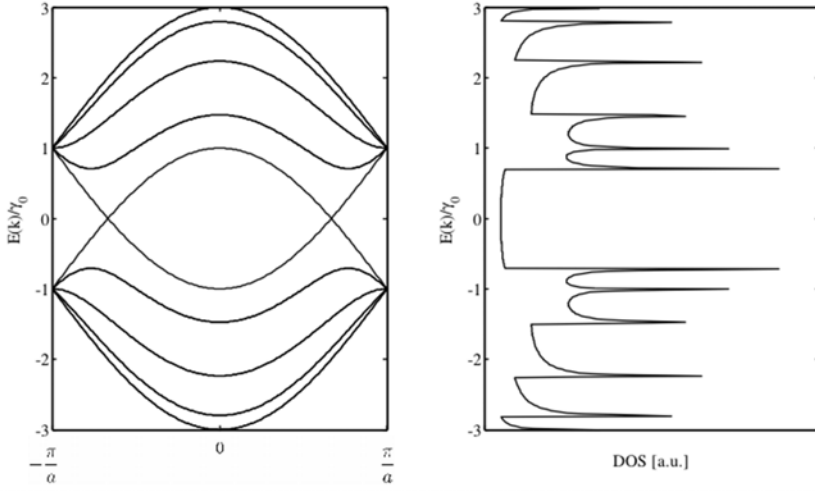


Figure 2.6: Energy band diagram (a) and DOS (b) for a metallic (4,4) nanotube.

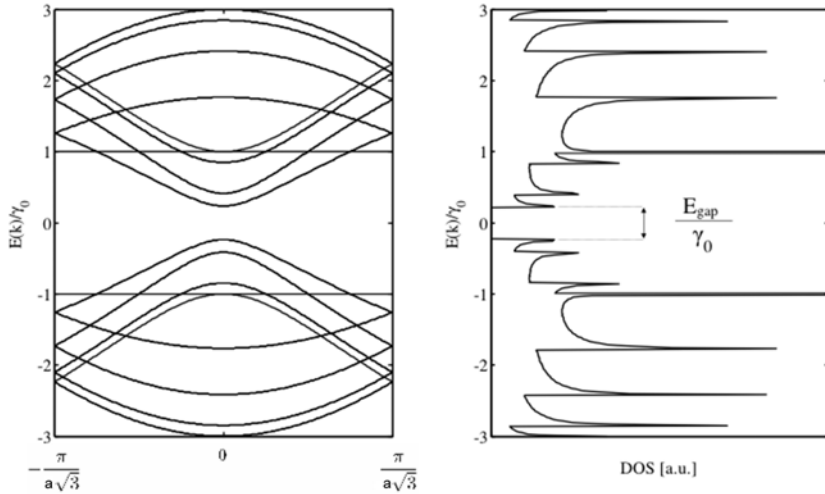


Figure 2.7: Energy band diagram (a) and DOS (b) for a semiconductor (8,0) nanotube [39].

2. Theoretical background

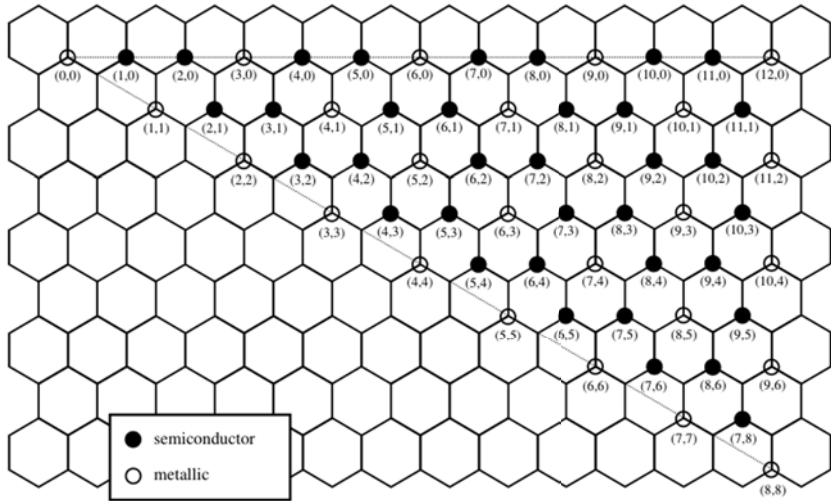


Figure 2.8: Diagram classification according to the chirality indicating the metallic or semiconductor character of the SWCNT.

studied with STS experiments, we will now focus on the nanotube-gold substrate interaction. The interaction between the carbon nanotube and the substrate is first of all assumed to be only determined by van der Waals forces [41, 42]. The binding energy is calculated to be in the order of 2 meV per atom. The binding energies for all the carbon atoms lying on the substrate add up to an energy that will maintain the nanotube fixed on the surface while imaging it with STM or AFM. Since the work function of Au(111) is 5.3 eV and for the CNT is 4.5 eV, there is charge transfer between the tube and the sample. Thus, as it is expected, a shift of the Fermi level of the CNT. Tight binding calculations indicate that this shift is in the order of 0.2 eV, consistent with experimental observations [43, 44]. This effect is presented in Figure 2.9 where the calculated and measured DOS of the nanotube on the gold substrate is presented in order to indicate the Fermi level shift.

Until now, it was shown how the substrate modifies the DOS of a defect free CNT. Since structural defects or adsorbed atomic species are also present or are used to test various predictions, it is important to verify the role of structural defect of adsorbed foreign atoms on the DOS of the CNTs. The Stone-Wales defect (SW-defect) [45], also known as the pentagon/heptagon pair, consists of two pentagons and two heptagons in the hexagonal graphene lattice. It is the most common defect in CNTs. The chiral angle of a nanotube determines the orientation of a Stone-Wales defect with respect to the axis of the tube. This orientation and the electronic structure properties of the CNT determine the effects of the SW-defect on the LDOS.

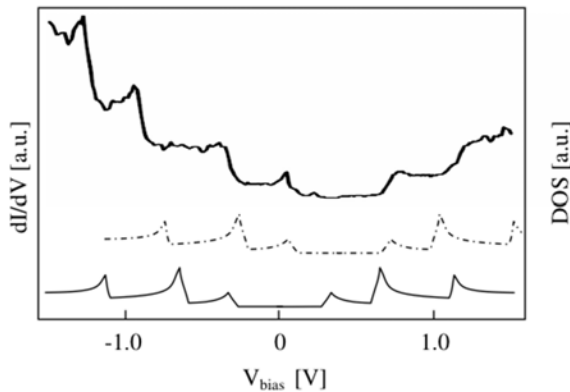


Figure 2.9: Tunneling spectroscopic data is shifted ~ 0.3 eV towards the valance band. The lower solid line is the calculated DOS for an isolated (16,0) nanotube, dashed line is the DOS shifted by ~ 0.3 eV to match the experimental STS data [37].

The theoretical work [46] made for a (7,7) armchair, a (12,0) zigzag and a (9,6) chiral tube reveals the appearance of two peaks in between the first pair of Van-Hove singularities in the LDOS of the CNT, specified as quasibound (virtual bound) states. From semiconductor physics these states are also called shallow states. The explanation of these states can be understood if one considers that the six-membered carbon rings are more stable than five- or seven-membered rings and therefore a heptagon will try to give up an electron to its neighbors. It means that it plays the role of a donor in a semiconducting nanotube. Consequently, a pentagon acts as an acceptor [47]. It is also mentioned that the spatial extent of such a defect disappears at 2 nm away from it. A similar result [48] as the one described above was obtained for a substitutional boron (acceptor) and nitrogen (donor) impurities. The quasibound states can be observed in Figure 2.10 [46].

In the case of a single vacancy, one carbon atom missing due to irradiation or ion bombardments, the lattice of the CNT reconstructs, resulting in the formation of a pentagon. The formation of this new bond in the pentagon with respect to the tube axis and curvature will alter the formation energies of the orientational options (the three fold symmetry is broken) [49]. Ruffieux et al. report a strong modification of the electronic structure near the Fermi level [9]. This is described as a local charge enhancement having three-fold symmetry, reflecting the nearest-neighbor directions of a single vacancy defect site. Besides these modifications, defects also mediate a redistribution of the electron density on a large scale. Tight binding calculations by Lu et al. show that single vacancies in the tubes yield typical defect states with sharp

2. Theoretical background

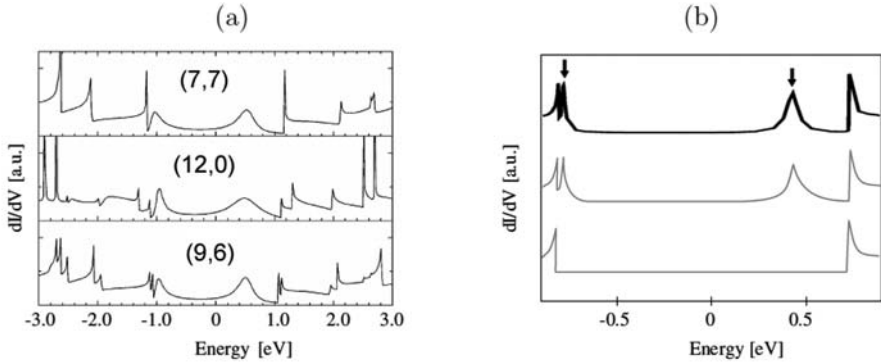


Figure 2.10: a) LDOS at SW defect on a (7,7) armchair, (12,0) zigzag and (9,6) chiral nanotube [46] - all three CNT s are metallic - and (b) LDOS at a SW defect on a metallic (10,10) armchair nanotube reveals shallow quasibound states assigned to the pentagons acting as acceptor level (at ~ -0.7 eV) and the heptagons acting as donor level (at ~ 0.5 eV).

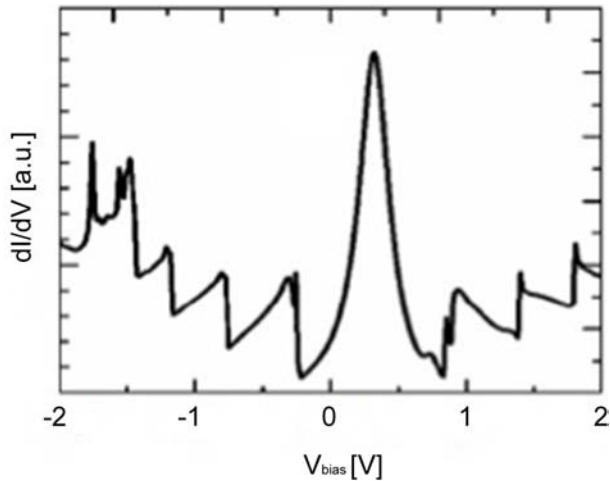


Figure 2.11: LDOS for a single vacancy in a metallic (10,10) armchair nanotube [51].

peaks at about 0.2 eV above the Fermi level for a metallic (8,8) and a semiconductor (14,0) tube [50]. The origin of the level close to the Fermi energy is attributed to the remaining dangling bond. Experimental STS results [51] confirm the presence of this level in accordance with the calculations, as observable in Figure 2.11. In Chapter 5 of this thesis STS results of LDOS modification of CNT upon H chemisorption will be presented. Our results will be compared and discussed in relation to the results presented above.

2.3 Persistent currents in normal metal rings

If at the ends of a normal metal wire a potential difference is set, an electrical current will start to flow. If the potential difference between the ends of the wire is cancelled, charge transport along the wire will stop due to various inelastic scattering processes like electron-phonon or electron-electron scattering. Consider now a nanoscopic metallic ring threaded by a magnetic flux, ϕ . Also consider that its circumference is smaller than the electron's phase coherence length, L . The induced current in a metallic ring for such conditions will last forever [52], supercurrents. The electron's phase coherence is the distance for which an electron travels in a medium without any inelastic scattering. Superconducting materials present a zero electrical resistance and are perfect diamagnetic materials (the Meissner effect). In 1983 Buttiker, Landauer and Imry have theoretically shown that persistent current exists also in normal metallic rings threaded by a magnetic flux [55]. To verify experimentally that persistent currents in normal metallic rings exist, the experimentalist must be aware of several conditions that have to be fulfilled. As mentioned above, electron-phonon scattering decohere the electron's wave function. In order to prevent the electron-phonon scattering, the temperature of the metallic ring must be as low as possible (usually up to hundreds of mK, for microscopic sized rings). Another requirement to observe persistent currents is related to the circumference of the ring itself. It should be comparable with the electron's coherence length. Since the electron's coherence is material dependent, the diameter of the metallic or semiconducting rings varies from several nm up to several μm .

The Aharonov-Bohm effect, also called Ehrenberg-Siday-Aharonov-Bohm effect, is a quantum mechanical phenomenon and describes how a charged particle is affected by an electromagnetic field in regions from which the particle is excluded due to the Meissner effect. A charged particle traveling around a loop experiences a phase shift of the wave function as a result of the closed magnetic field, although the field is zero in the region where the particle passes. The phase acquired by the electron wave function is proportional to $e/\hbar\phi$. The electron wave function must be continuous

2. Theoretical background

around the loop, thus the current passing through the loop will adjust in such a way that the acquired phase is an integer multiple of 2π . Thus, the amplitude of the persistent current is a function of magnetic flux quantum. The flux quantum can be calculated for superconducting materials with the following formula: $\Phi_0 = 2\pi\hbar c/2e \cong 2.0678 \times 10^{-15} \text{ Tesla}\times\text{m}^2$. For a normal metal ring the electrons are not paired, thus the flux quantum becomes: $\Phi_0 = 2\pi\hbar c/e \cong 4.1356 \times 10^{-15} \text{ Tesla}\times\text{m}^2$. The amplitude of the persistent current is e/τ_d , where τ_d is the time in which an electron travels around the loop. In comparison to superconducting persistent currents where the disorder potential is not important and the current itself is diamagnetic, the direction of the current in the loop depends on the amount of electrons available in the system. The current amplitude is proportional to the Thouless energy (a characteristic energy scale for disorder conductors). The Thouless energy is derived by scaling the Anderson localization [53,54]. The Anderson localization is the phenomenon in which electron wave interferences occur due to multiple-scattering paths. If the scattering inside a medium is large, the severe interferences can completely halt the waves inside the medium. Disorder plays an important role [55,56] on the value of the amplitude of the persistent current, several recent calculations indicating an enhancement or a total annihilation of the persistent current.

The presence of a persistent current in loops can be determined by the phase of the persistent current. It can be assumed that due to the phase randomness of each loop from the ensemble, a measurement would not give any result. Surprisingly, experimentally it was shown that the ensemble average does have a periodicity of $\Phi_0/2$, while the average persistent current on the loop is $0.05 e/\tau_d$. The measurements were performed on an ensemble of about ten million copper rings with micrometric dimensions [57,58]. The ensemble average is found to be non-zero if electron-electron interactions are considered to play a role in the physics of persistent currents. For attractive electron-electron interactions a diamagnetic response of the persistent current is generated, while in a repulsive regime of the electron-electron interactions the magnetic moment generated will be along the external magnetic field.

The order of magnitude for the persistent current is given by the contribution of the last occupied level, $I_0 = ev_F/L$, where v_F is the Fermi velocity and L is the perimeter of the loop. If a perfect three dimensional system has more channels for electron conduction, the total current can be derived as: $I = I_0\sqrt{M}$, only if the conduction channels are not correlated. The parameter M can be expressed as equal to A/λ_F^2 , where A represents the section of the ring and λ_F^2 is the Fermi wavelength. If disorder is added in the system, the theory predicts a reduction of the persistent current, $I = I_0l/L$, where the elastic electron mean free path l is included. The time required by an electron traveling ballistically to make the complete circumference of

the loop is $\tau = L/v_F$, but in a diffusive regime the time required can be rewritten as: $\tau_D = L^2/D$, where $D = v_F l$. D is the diffusive constant. Other contributions to the final theoretical value are dependent on the finite temperature under which the experiment is conducted. A first contribution is an exponential decay of the current value due to the intermixing of adjacent channels, giving opposite contributions to the total persistent current. The mixing of the levels occurs if they are in a $k_B T$ interval. The mixing also depends on the Thouless energy, thus the amount of disorder in the system. Another effect introduced by temperature is the reduction of the electron coherence length, L_ϕ leading to the persistent current vanishing exponentially with L/L_ϕ .

Maily et al. measured the magnetic response of a single GaAlAs/GaAs mesoscopic ring. In contrast to the previous measurements of persistent currents in normal metals (Cu, Au), the measured persistent current corresponds with the theoretical value expected [59]. The concordance with the theory is achieved due to the large electron coherence length (comparable with the perimeter of the loop), the low sample disorder and small amount of conduction channels.

The measurements on ensemble of rings were performed on relatively large (micron-sized) rings [60] where the electron coherence length is much smaller than the circumference of the rings. As discussed in the previous paragraphs, there are strong deviations from the expected theoretical values of the persistent current in the case of a diffusive ring. What we propose is to reduce the size of metallic rings, made from Au, down to several tenths on nanometers in diameter by means of colloidal lithography [61]. This will ensure a closer to one ratio between the electron coherence length and the circumference of the ring, bringing the system in study closer to the experimental situation of Maily et. al. An exhaustive comparison and discussion over our nanoscopic rings and the previous experimental work done will be presented in Chapter 6 of this thesis.

2.4 Coulomb gap

Upon a single hydrogen chemisorption on graphite a re-hybridization of the sp^2 character of the bonded C atom to an sp^3 character occurs [24–26]. The re-hybridization process implies a charge transfer from graphite to the newly formed C–H bond. HOPG presents a small density of states at the E_F . Due to the charge transfer from the bulk graphite to the newly formed C–H bonds, a further reduction of the $n(E_F)$ of HOPG will occur upon hydrogen chemisorption.

Consider the case of a single H atom bonded to one carbon atom at the surface of HOPG. The chemisorbed H atom acts as a point charge in the sea of conduction

2. Theoretical background

electrons, the π electrons. The electrostatic potential introduced by the C–H bond is screened by the free charge carriers of HOPG. The Thomas-Fermi approximation assumes that a local internal chemical potential (μ) can be defined as a function of the electron concentration at a specific point. The Thomas-Fermi screening length, $1/k_s$, is defined as follows:

$$k_s^2 = 6\pi n_0 e^2 / \epsilon_F = 4(3/\pi)^{1/3} n_0^{1/3} / a_0 = 4\pi e^2 D(\epsilon_F), \quad (2.4.1)$$

where a_0 is the Bohr radius, n_0 is the electron concentration and $D(\epsilon_F)$ is the density of states of free electron gas. The Thomas-Fermi (TF) screening length for graphite at 77K, where $n_0 \simeq 2 \times 10^{18} \text{cm}^{-3}$ [62–65] and $a_0^* = 2.12 \text{pm}$, is 5 Å. However, screening in a two-dimensional electron gas can be very different in comparison to the TF screening in normal metals.

If a material (e.g. insulator) does not have enough screening electrons (under-screened regime) electron-electron interaction effects are enhanced.

Electron - electron interaction effects in disordered electronic systems have been investigated for two regimes. In the weak disorder / e-e interaction regime in 2D, the effect of interaction represents itself as a logarithmic suppression of the DOS at the Fermi level [66], thus $\delta N \propto -\ln(V)$. This dependency of the density of states function of energy is commonly known as the zero bias anomaly (ZBA). By scanning tunneling spectroscopy, the ZBA was identified for several systems [52, 67, 69]. Recent coarse-grained tunneling density of states (TDOS) calculations for impurities on graphene show the angular dependence of the ZBA around an impurity [79]. In the case of a strongly insulating regime, Efros and Shklovskii [70, 71] have shown that Coulomb interactions produce a non-perturbative gap in the DOS of the host material. This gap is commonly known in literature as the Coulomb gap. The effect of a Coulomb gap is non-perturbative since the conduction properties do not change. In contrast, in the weak e-e interaction regime, a weakly metallic $\ln(T)$ transport conductivity is observed. The general expression for the Coulomb gap $N(eV) \propto |E - E_F|^{d-1}$ is function of the system dimensionality, d . For a 3D system, the Coulomb gap is expected to present quadratic energy dependence. Recently, it has been observed for a nonmetallic doped semiconductor Si:B and thin films of Be [72, 73, 80]. Graphite is a quasi two-dimensional material due its band structure properties. Coupling the quasi-2D character with its semimetal character, Coulomb interaction effects can be important. In 2D, the Coulomb gap presents a linear dependence of the DOS function of energy, as follows:

$$N(eV) = \frac{\alpha(4\pi\epsilon_0\kappa)^2 |eV|}{e^4}, \quad (2.4.2)$$

where κ is the relative dielectric constant, ϵ_0 is the permittivity of free space, α is a constant of order unity and e is the elementary charge.

2.5 Fano resonance

The Fano resonance is an interference phenomenon between a discrete level and a continuum. The discrete level can be represented, e.g. in solid-state physics, by an energetic level of an adsorbed foreign atom. In this case, the free electrons of the host material represent the continuum. The interaction between the free electrons and the localized state modifies the electronic structure properties of both the continuum and the localized state. If the modified electronic structure is investigated with STS, the TDOS presents a specific signature of the interference state. The shape of this feature is known in literature as Fano line shape.

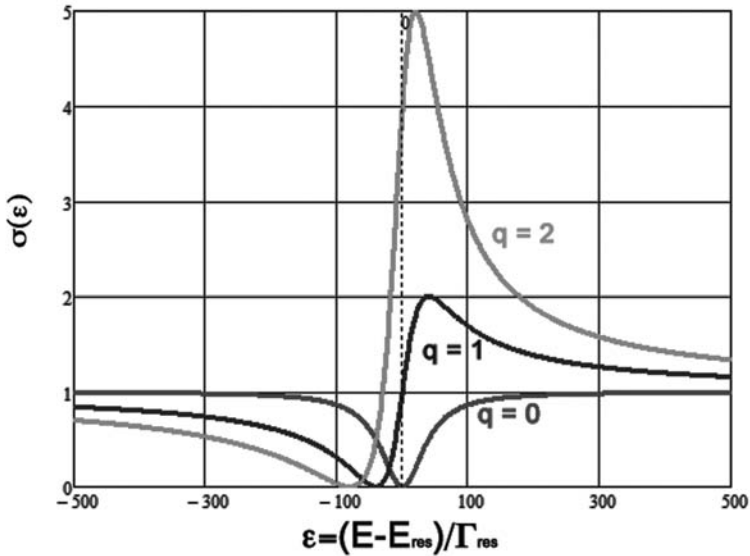


Figure 2.12: Simulated Fano line profiles for $q = 0, 1$ and 2 . For all three curves the resonance width, Γ_{res} the resonance E_{res} are set to 0.

The Fano line shape is observable in experimental works where phenomena like: Kondo processes [74–76], resonant scattering of a slow neutron in a nucleus [77] and auto-ionization in atomic spectroscopy [78] are present. The Fano resonance is a resonance for which the corresponding line profile in the cross-section has the so-called Fano shape. σ represents the total scattering cross-section and it is described by the following equation:

$$\sigma = \frac{(q\Gamma_{res}/2 + E - E_{res})}{(E - E_{res})^2 + (\Gamma_{res}/2)^2}, \quad (2.5.1)$$

where E_{res} and Γ_{res} represent the position, respectively the width of the resonance,

2. Theoretical background

from the Breit-Wigner formalism [77]. The q parameter is also known as the Fano parameter and represents the ratio between the resonant and direct (background) scattering probability. The Fano line profile can be simulated as a function of q .

As can be observed in Figure 2.12, the shape of the Fano line profile changes with q . If q tends towards infinity or 0, then the Fano line shape is replaced with a Lorentzian line profile. In Chapters 4 and 5 an analysis of the Fano line shapes observed in the H/HOPG and H/CNT will be presented.

Bibliography

- [1] E. Fitzer, K.-H. Kochling, H.P. Boehm, and H. Marsh. *Pure Appl. Chem.* 67:3, 473 (1995).
- [2] T.E. Weller, M. Ellerby, S.S. Saxena, R.P. Smith, and N.T. Skipper. *Nat. Phys.* 1, 39 (2005).
- [3] E.V. Konenkova, D. Grundler, M. Morgenstern, and R. Wiesendanger. *Tech. Phys. Lett.* 34, 30 (2008).
- [4] S.Y. Zhou, G.H. Gweon, A.V. Fedorov, C.D. Spataru, R.D. Diehl, Y. Kopelevich, D.H. Lee, S.G. Louie, and A. Lanzara. *Nature* 2, 595 (2006).
- [5] J.G. Kushmerick, K.F. Kelly, H.P. Rust, N.J. Halas, and P.S. Weiss. *J. Phys. Chem. B* 103, 10 (1999).
- [6] D. Tomanek and S.G. Louie. *Phys. Rev. B* 37, 8327 (1988).
- [7] N. Ooi, A. Rairkar, and J.B. Adams. *Carbon* 44(2), 231, (2006).
- [8] Y. Kobayashi, K.-I. Fukui, T. Enoki, and Y. Kaburagi. *Phys. Rev. B* 71, 193406 (2005).
- [9] P. Ruffieux, M. Melle-Franco, O. Gröening, M. Biemann, F. Zerbetto, and P. Gröening. *Phys. Rev. B* 71, 153403 (2005).
- [10] A. Gruneis, C. Attaccalite, T. Pichler, V. Zabolotnyy, H. Shiozawa, S.L. Molodtsov, D. Inosov, A. Koitzsch, M. Knupfer, J. Schiessling, R. Follath, R. Weber, P. Follath, R. Weber, P. Rudolf, L. Wirtz, and A. Rubio. *Phys. Rev. Lett.* 100, 037601 (2008).
- [11] Y. Kopelevich, J.C. Medina Pantojaa, R.R. da Silva, F. Mrowka, and P. Esquinazi. *Phys. Lett. A* 355, 233 (2006).

- [12] C. Oshima, T. Aizawa, R. Souda, Y. Ishizawa, and Y. Sumiyoshi, *Solid State Commun.* 65, 1601 (1998).
- [13] T. Aizawa, R. Souda, S. Otani, Y. Ishizawa, and C. Oshima. *Phys. Rev. B* 42, 469 (1990).
- [14] S. Siebentritt, R. Pues, K.H. Rieder, and A. M. Shikin. *Phys. Rev. B* 55, 7927 (1999).
- [15] Y. Kawashima and G. Katagiri. *Phys. Rev. B* 52, 10053 (1995).
- [16] R. Nicklow, N. Wakabayashi, and H.G. Smith. *Phys. Rev. B* 5, 4951 (1972).
- [17] L. Vitali, M.A. Schneider, and K. Kern. *Phys. Rev. B* 69, 121414(R) (2004).
- [18] N.M.R. Peres, F. Guinea, and A.H. Castro Neto. *Phys. Rev. B* 73, 125411 (2006).
- [19] J.M.D. Coey, M. Venkatesan, C.B. Fitzgerald, A.P. Douvalis, and I.S. Sanders. *Nature* 420, 156 (2002).
- [20] P. Ruffieux, O. Groening, P. Schwaller, L. Schlapbach, and P. Groening. *Phys. Rev. Lett.* 84, 4910 (2000).
- [21] Y. Niimi, T. Matsui, H. Kambara, K. Tagami, M. Tsukada, and H. Fukuyama. *Phys. Rev. B* 73, 085421 (2006).
- [22] M. Fujita, K. Wakabayashi, K. Nakada, and K. Kusakabe. *J. Phys. Soc. Jpn.* 65, 1920 (1996).
- [23] S. Cho, Y. Kim, A.J. Freeman, G.K.L. Wong, J.B. Ketterson, L.J. Olafsen, I. Vurgaftman, J.R. Meyer, and C.A. Hoffman. *Appl. Phys. Lett.* 79, 3651 (2001).
- [24] X. Sha and B. Jackson. *Surf. Sci* 496, 318 (2002).
- [25] D.W. Boukhvalov, M.I. Katsnelson, and A.I. Lichtenstein. *Phys. Rev. B* 78, 085413 (2008).
- [26] Y. Ferro, F. Marinelli, and A. Allouche *J. Chem. Phys.* 116, 8124 (2002).
- [27] L. Hornekær, Ž. Šljivančanin, W. Xu, R. Otero, E. Rauls, I. Stensgaard, E. Lægsgaard, B. Hammer, and F. Besenbacher. *Phys. Rev. Lett.* 96, 156104 (2006).
- [28] S. Iijima. *Nature* 354, 56 (1991).
- [29] private communication with P. Rudolf, (2011).
- [30] R.E. Smalley. *Acc. Chem. Res.* 25, 98 (1992).

2. Theoretical background

- [31] A. Ural, Y. Li, and H. Dai. *App. Phys. Lett.* 81, 3464 (2002).
- [32] B. Kitiyanan, W.E. Alvarez, J.H. Harwell, and D.E. Resasco. *Chem. Phys. Lett.* 317, 497 (2000).
- [33] <http://www.ou.edu/engineering/nanotube/comcat.html>.
- [34] D.E. Resaco, W.E. Alvarez, F. Pompeo, L. Balzano, J.E. Herrera, B. Kitiyanan, and A. Borgna. *Journal of Nanoparticles Research* 4, 131 (2002).
- [35] M.J. Bronikowski, P.A. Willis, D.T. Colbert, K.A. Smith, and R.E. Smalley. *J. Vac. Sci. Technol. A* 19, 1800 (2001).
- [36] R. Saito, M. Fujita, G. Dresselhaus, and M.S. Dresselhaus. *Phys. Rev. B* 46, 1804 (1992).
- [37] J.W.G. Wildoer, L.C. Venema, A.G. Rinzler, R.E. Smalley, and C. Dekker. *Nature* 391, 59 (1998).
- [38] T. Odom, J.L. Huang, P. Kim, and C.M. Lieber. *Nature* 391, 62 (1998).
- [39] F. Wittebrood. Master Thesis, Eindhoven University of Technology, 2007.
- [40] R. Saito, G. Dresselhaus, and M.S. Dresselhaus. *Physical Properties of Carbon Nanotubes*. Imperial College Press, London, (1998).
- [41] T. Hertel, R.E. Walkup, and P. Avouris. *Phys. Rev. B* 58, 13870 (1998).
- [42] S. Dag, O. Gulseren, S. Ciracia, and T. Yildirim. *Appl. Phys. Lett* 83, 3180 (2003).
- [43] Y. Xue and S. Datta. *Phys. Rev. Lett.* 83, 4844 (1999).
- [44] S.J. Tans, M.H. Devoret, H. Dai, A. Thess, R.E. Smalley, L.J. Geerlings, and C. Dekker. *Nature* 95, 166402 (2005).
- [45] A.J. Stone and D.J. Wales. *Chem. Phys. Lett.* 128, 501 (1986).
- [46] H.-T. Yang, L. Yang, J. Chen, and J. Dong. *Phys. Lett. A* 325, 287 (2004).
- [47] H. Kim, J. Lee, S.-J. Kahng, Y.-W. Son, S.B. Lee, J. Ihm, and Y. Kuk. *Phys. Rev. Lett.* 90, 216107 (2003).
- [48] H.J. Choi, J. Ihm, S.G. Louie, and M.L. Cohen. *Phys. Rev. Lett.* 84, 2917 (2000).
- [49] R.H. Telling, C.P. Ewels, A.A. El-Barbary, and M.I. Heggie. *Nature Materials* 2, 333 (2003).

- [50] A.J. Lu and B.C. Pan. *Phys. Rev. Lett.* 92, 105504 (2004).
- [51] A.V. Krasheninnikov, K. Nordlund, M. Sirvio, E. Salonen, and J. Keinonen. *Phys. Rev. B* 63, 245405 (2001).
- [52] Y. Imry. *Introduction to Mesoscopic Physics 2nd edition.*, Oxford Press University, Oxford (2002).
- [53] J.T. Edwards and D.J. Thouless. *J. Phys. C: Solid State Phys.* 5, 807 (1972).
- [54] P.W. Andreson. *Phys. Rev.* 109, 1492 (1958).
- [55] M. Buttiker, Y. Imry, and R. Landauer. *Phys. Lett. A* 96, 365 (1983).
- [56] H-F. Cheung, E. K. Riedel, and Y. Gefen. *Phys. Rev. Lett.* 62, 587 (1989).
- [57] A. Schmid. *Phys. Rev. Lett.* 66, 80 (1991).
- [58] V. Ambegaokar and U. Eckern. *Phys. Rev. Lett.* 67, 3192 (1991).
- [59] D. Mailly, C. Chapelier, and A. Benoit. *Phys. Rev. Lett.* 70, 2020 (1993).
- [60] A. Lévy, G. Dolan, J. Dunsmuir, and H. Bouchiat. *Phys. Rev. Lett.* 64, 2074 (1990).
- [61] P. Hanarp, M. Kall, and D.S. Sutherland. *J. of Phys. Chem. B* 107, 5768 (2003).
- [62] M.S. Dresselhaus and G. Dresselhaus. *Adv. Phys.* 30, 139 (1981).
- [63] B.T. Kelly. *Physics of Graphite*, Applied Science Publishers LTD (1981).
- [64] S.J. Williamson, S. Foner, and M.S. Dresselhaus. *Phys. Rev.* 140, A1429 (1965).
- [65] M.P. Sharma, L.G. Johnson, and J.W. McClure. *Phys. Rev. B* 9, 2467 (1974).
- [66] B.L. Altshuler, A.G. Aronov, M.E. Gershenson, and Y.V. Sharvin. *Sov. Sci. Rev. A* 9, 223 (1987).
- [67] M.E. Gershenson, V.N. Gubankov, and M. I. Falei. *Zh. Eksp. Teor. Fiz.* 41, 435, 1985. *ibid.*, *JETP Lett.* 41, 535 (1985).
- [68] Y. Imry and Z. Ovadyahu. *Phys. Rev. Lett.* 49, 841 (1982).
- [69] A.E. White, R.C. Dynes, and J.P. Garno. *Phys. Rev. B* 31, 1174 (1985).
- [70] A.L. Efros and B.I. Shklovskii. *J. Phys. C* 8, L49 (1975).
- [71] B.I. Shklovskii and A.L. Efros. *Electronic Properties of Doped Semiconductors*, Springer, New York (1984).

2. Theoretical background

- [72] J.G. Massey and M. Lee. *Phys. Rev. Lett.* 75, 4266 (1995).
- [73] J.G. Massey and M. Lee. *Phys. Rev. Lett.* 77, 3399 (1996).
- [74] H.B. Heersche, Z. de Groot, J.A. Folk, L.P. Kouwenhoven, and H.S.J. van der Zant. *Phys. Rev. Lett.* 96, 017205 (2006).
- [75] P. Wahl, L. Diekhoner, G. Wittich, M.A. Schneider, and K. Kern. *Phys. Rev. Lett.* 95, 166601 (2005).
- [76] M.A. Schneider, L. Vitali, P. Wahl, N. Knorr, L. Diekhoner, G. Wittich, M. Vogelgesang, and K. Kern. *Appl. Phys. A* 80, 937 (2005).
- [77] G. Breit and E. Wigner. *Phys. Rev* 49, 519 (1936).
- [78] U. Fano. *Nuovo Cimento* 12, 156 (1935).
- [79] E. Mariani, L.I. Glazman, A. Kamenev, and F. von Oppen. *Phys. Rev. B* 76, 165402 (2007).
- [80] V.Y. Butko, J.F. DiTusa, and P.W. Adams. *Phys. Rev. Lett.* 84, 1543 (2000).

Chapter 3

Experimental

3.1 Scanning tunneling microscopy

The scanning tunneling microscope (STM) was the first instrument that enabled scientists to achieve true atomic resolution in real space. The contribution to nanotechnology brought by STM rewarded its developers, Gerd Binnig and Heinrich Rohrer from IBM Ruschlikon, with the 1986 Nobel Prize in Physics. Consider U_0 the potential energy of a particle and E its total energy. In Newtonian physics, a particle can never be in a region where U_0 is greater than E . If a conducting probe is brought within a few atomic distances from a metallic surface, the principles of quantum mechanics allow the transmission of an electron from the tip to the sample through the potential barrier of the vacuum, a phenomenon called tunneling. Quantum mechanics also determines the decay of the wave function ψ inside the barrier to be:

$$\psi \propto e^{-z \sqrt{\frac{2m(U_0 - E)}{\hbar^2}}} \quad (3.1.1)$$

where z is the barrier width, m is the electron mass and $\hbar = \frac{h}{2\pi}$, the reduced Planck constant. The decay of the electron wave function during tunneling can be illustrated as in Figure 3.1.

The tunneling current between the STM probe and the sample is determined by the available density of states (DOS) of both tip and sample at energy E . Furthermore, the tunneling current depends on the DOS of the tip, ρ_t , and of the sample, ρ_s . The tunneling probability of the tunneling process is: $|M(E)|^2$. For $T=0$, the total tunneling current between tip and sample can be described by the Bardeen formula [2]:

$$I = \frac{4\pi}{\hbar} \int_0^{eV} \rho_s(E_{F_s} + E) \rho_t(E_{F_t} - eV + E) |M(E_{F_s} + E)|^2 dE \quad (3.1.2)$$

3. Experimental

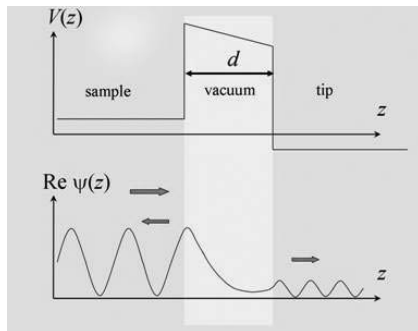


Figure 3.1: The electron wave function decay between sample and tip during tunneling through a barrier of width d .

where e is the electron charge and V represents the bias voltage applied between sample and tip. The Fermi energy, E_F , is the energy up to which the DOS is filled and it is material dependent. When two materials are brought in contact their Fermi energies will equalize. Since one of the contacts is biased then, $E_{F_s} = E_{F_t} - eV$. The tunneling current can be rewritten as:

$$I = \frac{2\pi e}{\hbar} \int_0^{eV} \sum_{i,j} |M_{ij}(E_{F_s} + E)|^2 dE \quad (3.1.3)$$

Thus, the tunneling matrix element $M_{ij}(E)$ contains valuable information about shape (s, p, d) of the wave functions of the tip and sample and their overlap at a specific energy E . Tersoff and Hamann [3] were the first to evaluate M considering that the tip wave function is modeled as a single s-orbital, $M_{ij} = M_j \propto \psi_{s_j}$. Because $|M_j|^2 = |\psi_{s_j}|^2 \equiv \rho_s$, equation 3.1.3 for small biases reduces to:

$$I \propto eV \rho_s(E_{F_s}) \quad (3.1.4)$$

which means that the tunneling current is directly proportional to the DOS of the substrate.

In equation 3.1.1 the barrier height, U_0 , can be considered to be the average barrier height between the tip and the sample $\frac{\phi_s + \phi_t + eV}{2}$, where the work function ϕ is defined as the minimum energy required to remove an electron from the material to the vacuum. Since $|M|^2$ is proportional to the overlap of the wave functions of the tip and sample and this wave function decays exponentially in vacuum, then the tunneling current I does also exponentially decrease as a function of the distance, z . In the constant current mode, the tunneling current, I_t is set at a specific setpoint value. Experimentally, the most common values for the setpoint current are between

1 pA and 10 nA. In order to maintain the pre-set tunneling current constant, a feedback loop is moving the tip towards or away from the sample. With piezo-electric materials very fine displacements (smaller than 10 pm) can be achieved, thus the tip can be scanned over the surface while maintaining the distance between the tip and sample. If the tip is moved over the surface then the change in the tip-sample distance, Δz , can be recorded for each point (x, y) . The result of scanning is a topographical image of the sample. The last statement is not entirely true since formula 3.1.4 shows that the apparent height is proportional to the DOS at the specific position. Scanning tunneling spectroscopy (STS) is a complementary method to extract information about the DOS at a specific position from STM experiments at the surface. In STS, the tip is positioned in a specific position, the feedback loop is switched off and the bias voltage between the tip and the sample is varied with a pre-defined number of steps and the current is recorded, thus obtaining a dependence of the tunneling current as a function of the applied bias. The first derivative of the $I(V)$ curve provides information about the charge density distribution of the sample. If the Tersoff-Hamann approximation is considered, the derivative of equation 3.1.4 is:

$$dI/dV(V) \propto \rho_s(x, y, E_{F_t} + eV). \quad (3.1.5)$$

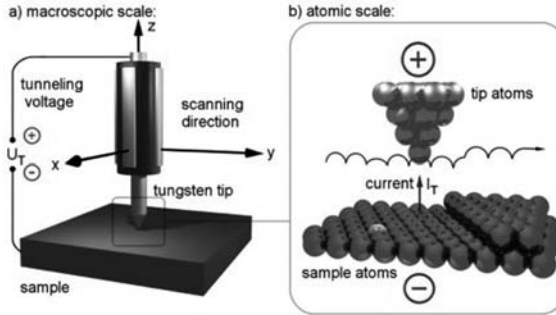


Figure 3.2: Schematic representation of an STM setup [1].

In this way, one can obtain the DOS at a specific position (x, y) of the sample surface. Two different experimental STM set-ups were used to obtain the experimental results that are described in this thesis. Both of them are commercial STM setups developed by Omicron GmbH. One of the setups is a variable temperature (VT) ultra high vacuum (UHV) - AFM with STM option; the other is a low temperature (LT) STM. The VT AFM/STM and was used to:

- determine the HOPG contamination after sample cleave, annealing steps, and

3. Experimental

prolonged exposure to the UHV environment;

- identify the structures [2] formed by hydrogen atoms on HOPG;
- correlate the HOPG exposure time to the H plasma with the measured coverage from STM topography;
- determine an appropriate Au(111) preparation procedure in order to obtain flat atomic terraces for CNT deposition and characterization;
- topological and spectroscopical analysis of H treated and non-treated carbon nanotubes.

In the VT ATM/STM no STS experiments were conducted at low temperatures since only the sample can be cooled to 25 K by heat exchange with a flow cryostat. However the STM tip is assumed to be close to RT. Phase transitions can occur while the temperature is varied (e.g. superconductivity). In order to test the temperature dependence of the hydrogen on the DOS of the carbon based material (HOPG, CNT), the STS work presented in this thesis is done on the LT-STM. The operating base pressure in the STM chamber is lower than 10^{-10} mbar. The minimum operating temperature that can be achieved with this setup is 4.8 K and this is done by a system of two separate bath cryostats, where the inner cryostat is filled with liquid helium and the outer cryostat with liquid nitrogen. If the outer shield is refilled with liquid nitrogen at each 5-6 hours, then the STM measurements can be performed at 4.8 K for 24 hours.

The STM tips used in this work were prepared from two different materials, tungsten (W) and PtIr. By electrochemical etching of a polycrystalline tungsten wire (ϕ 0.35 mm), W tips were prepared. In order to check the apex radius of the tip SEM experiments were also conducted and the tip apex was imaged. The STM tip radius is important for topography imaging and it is less relevant for scanning tunneling spectroscopy. Since the W tips are handled in ambient atmosphere tungsten oxide (WO_3) forms as a layer at the surface. In order to remove the oxide from the tips, they were annealed at temperatures in excess of 1200 °C by means of electron beam heating. Above the mentioned temperatures the tungsten oxide sublimates exposing a fresh W apex surface of the tip. A simpler and faster tip preparation procedure is achieved if PtIr wire (90%, 10%) (ϕ 0.35 mm) is mechanically cut. Since PtIr does not oxidize in ambient atmosphere the tip annealing step, as in the case of W tips, can be avoided. For good STM tips, both from W and PtIr, similar results (in terms of imaging and spectroscopy) have been achieved during the experimental work presented in this thesis, thus our results are not tip material dependent. Figure 3.2

illustrates the schematics of an STM setup on the left hand side while in the right hand side the STM tip and atomic surface is depicted.

3.2 Atomic force microscopy

As in any other scanning probe microscopy technique, atomic force microscopy (AFM) operates by monitoring and controlling the interaction between a sharp needle and a sample. The sharp needle is called AFM tip and the most common used materials are Si and Si₃N₄. The AFM tip is mounted on a cantilever. An AFM setup can operate in three regimes, namely: contact mode, tapping mode or non-contact mode. As the names suggest, in contact mode the AFM tip is brought into contact with the sample and just dragged along the surface. This working regime can be used for hard samples, were the forces applied on the surface do not damage the sample. In tapping mode, the tip is slightly touching the surface that is investigated and it is oscillating at the resonant frequency of the cantilever. If the excitation frequency externally applied is slightly off the resonant frequency of the cantilever, then the tip will not touch by purpose the sample, thus non-contact mode is achieved. It is preferable for soft samples to use the non-contact operating mode since the physical damage produced to a sample is kept to a minimum. The force governing the interaction between the tip and the sample is the van der Waals force, $F(r)$, and can be described by the equation 3.2.1 assuming that the tip can be modeled with a sphere:

$$F(r) = AR[\frac{1}{30}(\frac{\sigma}{r})^8 - (\frac{\sigma}{r})^2], \quad (3.2.1)$$

where $A = \frac{2}{3}\pi^2 w_0 \rho_{sp} \rho_{su} \sigma^4$, consists of the minimum energy of Lennard - Jones interaction potential (w_0), the number of density of atoms in the sphere, surface (ρ_{sp}, ρ_{su}) and the distance between two atoms σ , for which the potential is zero, thus the minimum energy w_0 . Figure 3.3 depicts the schematics of an AFM setup.

The cantilever deflection, described by Hooke s law, is a measure of the forces acting on the tip. To determine the forces acting between the tip and surface, a LASER beam is projected onto the cantilever and its reflection is projected on a photodiode segmented in four quadrants. By measuring the position of the reflected LASER spot in respect to the center of the photodiode the torsion and vertical displacement of the cantilever are determined. Making use of an electronic feedback system, the tip can be brought back to the initial, preset values making use of the piezo drives. In a simple case, if the distance between the tip and the sample has decreased, the control unit will contract the z -piezo element in order to maintain the constant height difference between the tip and the sample. Thus, the feedback system gives the information required to obtain all the information acquired during an AFM experiment. The xyz

3. Experimental

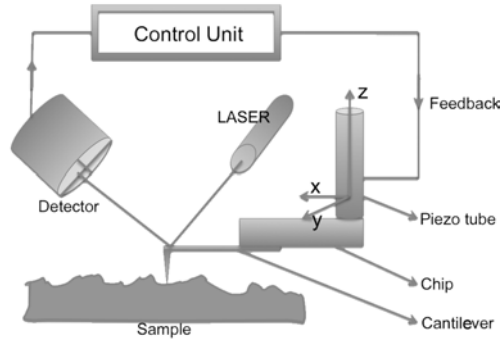


Figure 3.3: Schematic representation of an AFM setup.

scanner calibration was on monthly basis performed with AFM gratings purchased from NT-MDT [3].

Since its development by Binnig, Quate and Gerber in 1986, AFM has gained additional capabilities when the tips are coated with different materials. For example, coating an AFM tip with magnetic materials makes it possible to be sensitive not only to the surface topology but also to the magnetic properties of the sample in study. The radius of curvature of the AFM tip determines the lateral resolution of an AFM scan. Typically the radius of curvature is around ten nanometers but ultra-sharp tips can be also produced, for example by attaching a single carbon nanotube to the commercially available tip, thus improving the lateral resolution by a factor of ten. In this thesis the AFM technique was used in order to investigate the roughness of the surface during the gold nanorings preparation procedure. Since the typical height of the gold structures is in the order of 5 - 7 nanometers a low roughness of the substrate was required.

3.3 Superconducting quantum interference device

Arnold Silver, Robert Jaklevic, John Lambe, and James Mercereau of Ford Research Labs developed the first superconductive quantum interference device (SQUID) in 1964. SQUID is a sensitive magnetometer, used to measure very small magnetic fields, as low as 5 aT. The operating principle is based on the Josephson effect [4], postulated in 1962 by B. D. Josephson. The Josephson effect is the phenomenon of current flow across two weakly coupled superconductors (S), separated by a thin insulating (I) barrier, so that tunneling of Cooper pairs takes place. The S-I-S configuration is commonly known as a Josephson junction. The dynamics of the Josephson junctions

3.3 Superconducting quantum interference device

are determined by the equations:

$$U(t) = \frac{\hbar}{2e} \frac{\partial \phi}{\partial t}, \quad (3.3.1)$$

and

$$I(t) = I_c \sin(\phi(t)) \quad (3.3.2)$$

$U(t)$, $I(t)$ represent the voltage, the current across the junction. The phase of the current shift across the junction is $\phi(t)$, while I_c is the critical current across the junction. The critical current is defined as the exact point where the material loses its ability to carry electrical current without resistance. The value of the critical current is dependent on temperature and applied external electric field. There are three main effects following from equations 3.3.1 and 3.3.2: the direct current (DC), the alternating current (AC) and the inverse AC Josephson effects. The DC Josephson effect is the phenomenon of a direct superconducting current crossing the insulating barrier in the absence of any external electromagnetic field. The current is proportional to the sine of the phase difference across the insulator, and the value of the current is between $-I_c$ and I_c , by following equation 3.3.2. For the AC Josephson effect a fixed voltage U_{DC} is applied across the junction and as a consequence the phase will vary linearly with time, as observable from equation 3.3.1. Therefore, the current will be AC with an amplitude equal to I_c and a frequency of $\frac{2e}{\hbar}U_{DC}$. In this case the junction can be regarded as a perfect voltage to frequency convertor. In the inverse AC Josephson effect if the phase is $\phi(t) = \phi_0 + n\omega t + a \sin(\omega t)$ then the DC components of the current and the voltage become: $I(t) = I_c J_{-n}(a) \sin(\phi_0)$, $U_{DC} = n \frac{\hbar}{2e} \omega$. Thus, for distinct DC voltages, the junction may carry a DC current and acts like a perfect frequency to voltage convertor. For his work B. D. Josephson was awarded with the 1973 Nobel Prize in Physics.

The DC SQUID consists of a superconducting loop containing two Josephson junctions as depicted in Figure 3.4. The interference effect used in the DC SQUID is the modulation of the supercurrent by an applied magnetic field passing through the loop. This occurs since the magnetic field changed the phases of the wavefunctions across the junctions, hence the currents passing through. There are two junctions, but a single-valued phase restriction must be imposed in the following form: $2k\pi = \delta_1 + \delta_2 + \frac{2\pi}{\Phi_0} \Phi_x$. The junction currents are related to the wavefunction phases by: $I_1 = I_c \sin \delta_1$ and $I_2 = I_c \sin \delta_2$, where I_c is the critical current and at this point it is assumed that the two Josephson junctions are identical. Using Kirchhoff's law for a node reveals $I_0 = I_2 - I_1$. The wave functions adjust themselves to continuously satisfy the last four equations. The maximum current is:

$$(I_0)_{max} = \sqrt{2} I_c \sqrt{1 + \cos\left(\frac{2\pi}{\Phi_0} \Phi_x\right)} \quad (3.3.3)$$

3. Experimental

From equation (3.3.3) it is clear that the magnetic field modulates the passing current. In practice the Josephson junctions are never identical thus the equations can be rewritten as:

$$2k\pi = \delta_1 + \delta_2 + \frac{2\pi}{\Phi_0}(\Phi_x + LI_S) \quad (3.3.4)$$

$$I_1 = I_S - \frac{1}{2}I_0 = I_{C1} \sin \delta_1 \quad (3.3.5)$$

$$I_2 = I_S + \frac{1}{2}I_0 = I_{C2} \sin \delta_2 \quad (3.3.6)$$

where I_S is the current induced by the flux change through the coil (shielding current) and I_{C1} and I_{C2} are the critical currents of the junctions. This set of equations do not have an analytical solution but numerical solutions have shown that the critical supercurrent modulation still occurs with a period of Φ_0 with a non-sinusoidal form.

A DC SQUID is supplied with a constant current. The flux through the loop is modulated by a reference high frequency flux from a feedback coil with a magnitude less than Φ_0 in order not to mask any signal that should be actually detected. The lock-in amplifier is used to amplify the difference between the SQUID loop's signal and the reference signal. This difference is then used as a feedback signal for the feedback coil that has to cancel the input flux by increasing or decreasing the voltage across the SQUID loop.

This technique was used to determine the magnetization of nanoscopic gold nanorings. The results will be presented and discussed in Chapter 6.

3.4 Hall effect measurements

The van der Pauw method [5,6] is used to measure the Hall effect [7]. The results were acquired with an automated probe station setup. The resistivity measurements can be performed between room temperature (RT) and 4 K. The maximum magnetic field that can be applied to the sample is 1 T, while the sample is fixed on an electrically insulating plate that is mounted on a rod. The copper wires that are glued to the samples are connected to electrical pins, thus making the electrical connections between the sample and the electronics of the setup. The rod is then inserted in a vessel where He gas is pumped in. He gas is used as heat exchanger (better thermal stability). The He gas brings to this experiment two main advantages: shorter measurement times and chemical inertness. To perform temperature dependence measurements, the setup is equipped with a flow-cryostat. To stabilize the temperature at a desired set point, the resistive heating element is controlled by a PID feedback system. Furthermore, when the temperature or magnetic field reached the set point a time delay in the measurement can be prescribed (e.g. wait 2 minutes after set point

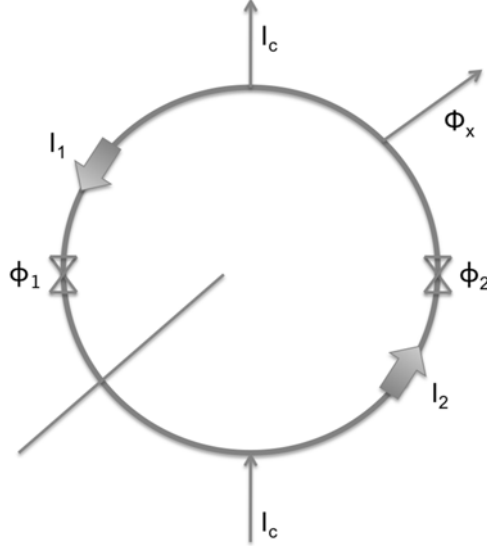


Figure 3.4: DC SQUID superconducting loop.

was reached and then acquire desired data). This stabilization interval should provide more accurate and reproducible results. The measurement itself is fully automated and computer-controlled.

On the sample four electrical contacts are placed. If a current I_{12} is applied between contacts 1 and 2, then a potential drop U_{34} is measured between contacts 3 and 4. Thus, the resistance is $R_{12\ 34} = U_{34}/I_{12}$ is measured. If a current is flown between contacts 2 and 3, then similar to above the resistance $R_{23\ 41}$ is determined. Van der Pauw showed that:

$$e^{-\pi R_{12,34} R_S} + e^{-\pi R_{23,41} R_S} = 1 \quad (3.4.1)$$

where R_S is the sheet resistance. The measurements should be reciprocal, meaning that flowing a current from contact 1 to contact 2 and measuring the potential difference between contacts 3 and 4 should provide similar results as if the current is flown between contacts 3 and 4, while the potential difference is measured between contacts 1 and 2. Mathematically, the above-mentioned statement translates into: $R_{12\ 34} = R_{34\ 12}$. To simplify equation 3.4.1:

$$R_{vertical} = \frac{R_{12\ 34} + R_{34\ 12}}{2} \quad R_{horizontal} = \frac{R_{23\ 41} + R_{41\ 23}}{2} \quad (3.4.2)$$

Under the condition that $R_{vertical} = R_{horizontal} = R$, equation 3.4.1 results in: $R_S = \pi R / \ln 2$. If the above-mentioned condition is however not fulfilled, a numerical solution can be found for equation 3.4.1 via iterative methods.

3. Experimental

If a charged particle (e.g. electron) is placed in a magnetic field, the Lorentz force ($F_L = QvB$) is affecting the particles trajectory function of the particle velocity v , magnetic field strength B and amount of charge possessed by it, Q . The electron velocity can be written as $v = \frac{I}{nAq}$, where I is the current value, n is the electron density, A is the cross-sectional area of the material and q represents the elementary charge.

Under the condition that the external magnetic field is applied perpendicular to the direction of current flow, the Lorentz force experienced by the electrons becomes: $F_L = \frac{IB}{nA}$. The Lorentz force produces accumulations of electrons in one part of the sample and depletion on another part, thus a potential difference across the sample, which is commonly known as Hall voltage. However, the current continues to flow along the sample, which indicates that the force on the electrons due to the electric field balances the Lorentz force. Thus the value of the electric field can be written as: $E = \frac{IB}{qnA}$. Thus, the magnitude of the Hall voltage is:

$$V_H = wE = \frac{wIB}{qnA} = \frac{IB}{qnd} \quad (3.4.3)$$

where w is the width of the material and d is the depth of the material. If the Hall voltage is expressed function of electron sheet density then: $V_H = \frac{IB}{qn_S}$.

Two sets of measurements are made: one of them with the magnetic field in the positive z -direction of the sample and the other one in the negative z -direction. The Hall voltages are recorded for both magnetic field directions. Then the differences between the voltages are calculated. In order to provide more accuracy to the measurements the reciprocity theorem suggests measuring the Hall voltage by reversing the direction of the current flow in the sample. The polarity of the Hall voltage measured provides information regarding the type of doping in the material. Thus, if it is positive a p -type material is measured, respectively, n -type if a negative voltage is measured. The sheet density is $n_S = \frac{IB}{q|V_H|}$.

The resistivity of a semiconductor material can be written as:

$$\rho = \frac{1}{q(n\mu_n + p\mu_p)} \quad (3.4.4)$$

where n and p are the concentration of electrons and holes in the material while μ_n and μ_p are the mobility of the electrons and holes. If the material is doped, then the mobility of the majority charge carriers is:

$$\mu_m = \frac{1}{qn_S R_S} \quad (3.4.5)$$

In conclusion, the Hall measurements provide information regarding: the resistance, the sheet resistance, the charge mobility and the charge density. The ability of Hall

measurements to provide the above-mentioned quantities is going to be used in order to determine any electrical conduction changes of graphite upon hydrogen chemisorption. The results are discussed in the following chapter.

Bibliography

- [1] S. Woedtke. Ph.D. thesis, Inst. f. Exp. u. Ang. Phys. der CAU Kiel, 2002.
- [2] L. Hornekær, Ž. Šljivančanin, W. Xu, R. Otero, E. Rauls, I. Stensgaard, E. Lægsgaard, B. Hammer, and F. Besenbacher. *Phys. Rev. Lett.* 96:156104, 2006.
- [3] www.ntmdt.com
- [4] B.D. Josephson. *Rev. Mod. Phys.* 46, 251 (1974).
- [5] L.J. van der Paauw. *Philips Research Reports* 13, 1 (1958).
- [6] L.J. van der Paauw. *Philips Technical Review* 20, 220 (1958).
- [7] E. Hall. *American Journal of Mathematics* 2, 287 (1879).

Chapter 4

The role of H-adsorbed atoms on graphite: zero bias anomaly in the density of electron states

4.1 Introduction

Graphite is composed of stacked layers of two-dimensional graphene. In the last years, numerous experimental and theoretical studies of graphene and bilayer graphene have been performed. A key feature of many layered materials is the anisotropy exhibited by its transport properties: while being metallic within the layers, the transport in the c -axis, perpendicular to the layers, may be coherent or incoherent and undergo a crossover with temperature from one regime to the other, thus changing the effective dimensionality of the system [1, 2]. Even when coherent electron excitations can be assumed within individual layers, there is no consensus about over what length and time scales the excitations are coherent between layers [1]. Electron correlations also play a key role in the physics of layered materials since correlation effects increase as dimensionality decreases. Therefore dimensionality is crucial for the electronic properties and to choose the appropriate model to study the system. Unconventional properties are derived from the anisotropy and periodicity along the axis perpendicular to the planes i.e. the structure of collective excitations absent in two dimensional (2D) and three dimensional (3D) electron gases [3]. These unconventional properties are distinctly different from that of the traditional Fermi liquids.

Graphite, an hexagonal layered material, presents an intra-plane hopping much larger than the inter-plane hybridization. Many of the transport properties established

4. The role of H-adsorbed atoms on graphite: zero bias anomaly in the density of electron states

in the past for this well-known material are being questioned at present. Recent conductivity measurements reveal a suppression of the c -axis conductivity much larger than what would be predicted by the band calculations of the interlayer hopping [2]. Band structure calculations are also challenged by very recent claims of observation of quantum Hall plateaus in pure graphite [4]. The unconventional transport properties of graphite such as the linear increase with energy of the inverse lifetime [5,6], suggest deviations from the conventional Fermi liquid behavior, which could be due to strong Coulomb interactions unscreened because of the lack of states at the Fermi level [7,8]. The experimental isolation of single graphite layer (graphene) [9] has enhanced the importance of graphite opening new possibilities in the application field. The properties of a few single layers of graphite have been measured and the experiments confirm the theoretical predictions of a physics governed by the 2D Dirac equation and a linear dispersion in the proximity of the K points [9,10].

In the presence of electron-electron interactions, tunneling processes are modified by inelastic scattering events. The influence of inelastic scattering on electron tunneling has been studied, using equivalent methods, in mesoscopic devices which show Coulomb blockade [11], Luttinger liquids [12–15], and dirty metals [16].

When electrons are confined to move in a plane (2D), different physics might come into play. For example, under normal circumstances, they are not expected to conduct electricity at low temperatures. The absence of electrical conduction in two dimensions (2D) at zero temperature has been one of the most cherished paradigms in solid-state physics. In fact, the 1977 physics Nobel Prize was awarded, in part, for the formulation of the basic principle on which this result is based. However, recent experiments [17] on a dilute electron gas confined to move at the interface between two semiconductors pose a distinct counterexample to the standard view. Transport measurements reveal [17] that as the temperature is lowered, the resistivity drops without any signature of the anticipated up-turn as required by the standard account. It is the possible existence of a new conducting state and hence a new quantum phase transition in 2D.

4.2 Sample preparation procedure

HOPG (NT–MDT) ZYA (0.4 - 0.7 degree mosaic spread) or ZYH (3.5 - 5.0 degree mosaic spread) [27] is cleaved with scotch tape under ambient atmospheric conditions. The sample is afterwards inserted into an UHV chamber (base pressure of 10^{-9} mbar) and it is annealed for two hours at approximately 800 °C so that any eventual adsorbents are removed. After the annealing step follows the hydrogen or deuterium deposition. In ambient conditions of temperature and pressure, on Earth, H and D

4.2 Sample preparation procedure

are found in a molecular state. To dissociate molecular H_2 (D_2), several methods can be used. One of the methods to atomize H_2 or D_2 is to make use of a hot filament (that can be covered by a catalytic metal in order to reduce the temperature of the filament) that is exposed to the gas flow, resulting in atomic H or D. Another way to achieve H_2 or D_2 atomization is to make use of a plasma discharge. Different types of plasma discharges can be used, creating either energetic or thermalized H^+ or D^+ ions. Previous studies of energetic (energy in the range of MeV) H^+ or Ar^+ irradiating HOPG indicated that the process is irreversibly destructive for the first several layers of graphite, thus leading to the removal of C atoms from the top layers [29]. These types of structural defects are hard to investigate since it is almost impossible to know precisely how many carbon atoms have been sputtered from the lattice, thus it is hard to repeat and theoretically model such an experiment.

To produce thermalized H^+ or D^+ , a radio-frequency (RF) plasma discharge (Oxford Applied Research Atom/Radical Beam source) operated at a base pressure of 10^{-2} mbar with a flow gas H_2 or D_2 is used. After the ions are created in the ionization chamber they are atomized by scatterings with a permeable quartz glass located at the plasma source nozzle. The RF plasma source used in these experiments operates by means of an electrical discharge created from inductively coupled RF excitation at 13.56 MHz. The nozzle of the plasma discharge chamber is located about 5 cm away from the graphite surface. The amount of D or H chemisorbed the top HOPG layer can be tuned by varying the sample exposure time. Exposure times varying between 5 seconds and 1 minute were performed. After the hydrogen has been deposited on HOPG, the sample is exposed to environment since the RF plasma source is not part of the UHV LT STM setup. The first step after inserting the H/HOPG sample into the LT STM setup is annealing. The annealing temperature is about 390 K, temperature where H or D dimers do not recombine to leave the surface [32]. This annealing step is necessary in order to eliminate any eventual water or adsorbents present on the surface of HOPG. Although sample contamination with foreign atomic species except H and D cannot be completely ruled out, several arguments can be brought to support of the idea that most of the surface structures investigated with the STM presented in this work are H and D chemisorbed patches. First, the purity of the H_2 (D_2) gas used in the plasma discharge is of 99.99 %. Second, any air contaminants (water or intercalates) will be removed by a second annealing step. It can also be debated that any metallic contaminants (e.g. Na) will oxidize as soon as the sample is taken into air. Third, there are several structures that can be identified by STM topography imaging of the modified surface. Lastly, temperature programmable desorption (TPD) experiments indicate specific desorption temperatures for the chemisorbed hydrogen. TPD experiments were used to check for eventual remaining contaminants

4. The role of H-adsorbed atoms on graphite: zero bias anomaly in the density of electron states

or defects induced by the hydrogen RF plasma discharge.

The sample is afterwards transferred in an adjacent UHV chamber, at the STM. All the samples were scanned on either the variable temperature (25 K - 1500 K) AFM/STM or the low temperature - STM (4.8 K - 300 K) (both by Omicron GmbH). The samples were investigated mainly at the following temperature: 5 K, 77 K, 120 K and RT. The base pressure when performing STS was never higher than 5×10^{-10} mbar at RT, important fact especially for low temperature investigations since the surface sticking coefficient is close to 1 when the temperature of the sample drops below 77 K.

4.3 Experimental results and discussion

4.3.1 Hydrogen on HOPG. Topological effects

To compare the topological changes and density of states changes of HOPG upon H or D chemisorption, we will make a start by showing experimental results obtained on clean HOPG. The ABAB stacking (or $\alpha\beta\alpha\beta$ stacking) of the graphene planes in a three dimensional crystal creates two non-equivalent sites, the α sites where the charge density at the Fermi level is suppressed due to the weak van der Waals forces and the β sites that do present charge density at the Fermi level and can be seen in the scanning tunneling microscopy (STM) imaging [30]. Depicted in Figure 2.1 is the crystallographic structure of HOPG. As observable, in each hexagon there are two sets of inequivalent atoms. Three atoms from the hexagonal lattice have a neighboring atom underneath (β sites), while the other three do not (α sites). Due to the $\alpha\beta$ stacking of the graphene layers in the crystal only the β sites are visible in the topography, Figure 4.1. The topography shows a very small corrugation as it can be seen in the topographical cross section.

After the graphite was treated in the hydrogen plasma, STM topography imaging reveals an increase in the sample corrugation, observable in Figure 4.2. To facilitate the visual topological comparison, Figure 4.1 and Figure 4.2 have the same scan size, 20×20 nm². For the moment, let us consider the hillock features to be created by chemisorbed hydrogen. As it can be observed from this topography imaging, sub-monolayer coverage is obtained while the sample is exposed to the plasma for about 15 seconds. Obviously, it is a sub-monolayer since the graphite lattice is still observable in between the hydrogen structures. The island growth mechanism of hydrogen on graphite has been also observed in other experiments [31].

Although HOPG surface contaminations from the plasma discharge cannot be excluded, several factors and sample preparation procedures indicate that the surface must actually be covered mostly with H. First of all, since the sample is taken in air

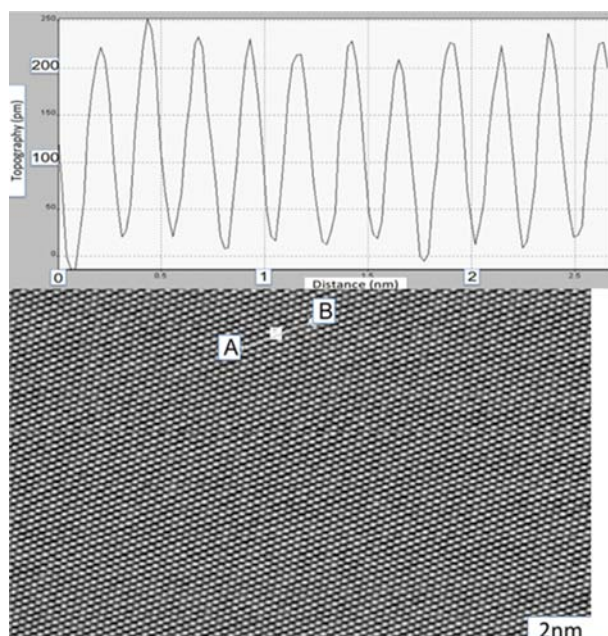


Figure 4.1: a) Topographical STM results of $19 \times 12 \text{ nm}^2$ depicting a clean, smooth periodic atomic structure, measurement parameters: $V = 124 \text{ mV}$ and $I = 0.47 \text{ nA}$. Overlaid, cross section indicating the lattice periodicity (2.46 \AA) and a corrugation of about 220 pm .

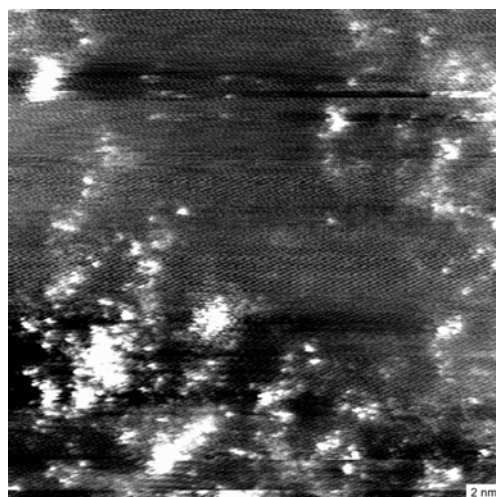


Figure 4.2: $20 \times 20 \text{ nm}^2$ STM topography of HOPG exposed to hydrogen plasma for 15 s. The bright features are attributed to hydrogen structures. Scanning parameters, $V = -325 \text{ mV}$, $I = 0.47 \text{ nA}$.

4. The role of H-adsorbed atoms on graphite: zero bias anomaly in the density of electron states

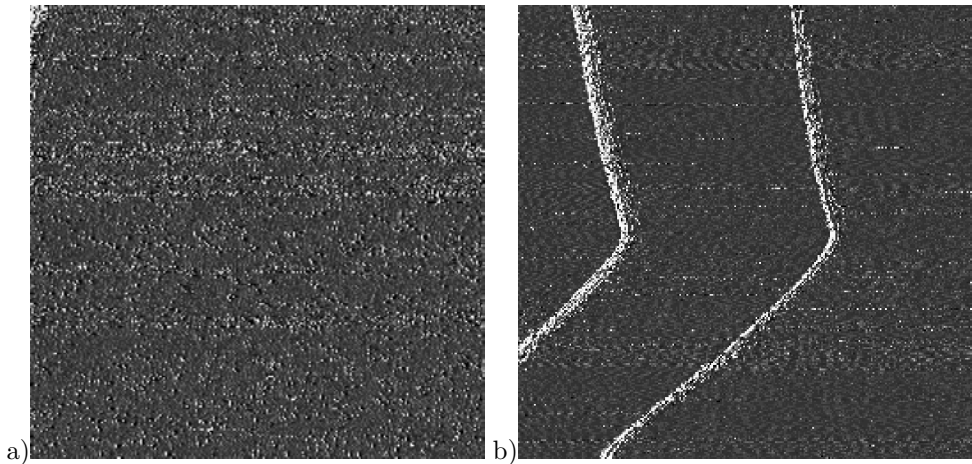


Figure 4.3: $550 \times 550 \text{ nm}^2$ STM topography of: a) 20 s hydrogen plasma exposed graphite surface; b) same sample as in a) after the annealing at 600 K. The scanning parameters are: $V = -230 \text{ mV}$, $I = 0.45 \text{ nA}$

(for a few minutes) after the plasma exposure, metallic contaminants can be excluded due to the oxidation processes. Another important factor to consider is the chemical inertness of graphite while in air. After the sample is introduced in the UHV setup where the STM experiments are made, another low temperature annealing step is done (390 K), thus removing water and other possible physisorbed species. Temperature programmable desorption (TPD) experiments correlated with DFT calculations [31] suggest that annealing the sample at 600 K should reveal the graphitic lattice since all the hydrogen should be desorbed at the specified temperature. Furthermore, if structural defects are created during the plasma treatment, a simple topography scan should reveal them. For comparison, before the annealing step performed at 600 K (Figure 4.3a) and after it (Figure 4.3b), STM experiments were performed. After the annealing step no hillock features are observable on the surface of HOPG. Furthermore, no indications of structural defects were detected. In conclusion, from the assumptions made and the TPD experiment, the plasma treatment is nondestructive for the top graphitic layer and mainly chemisorbed hydrogen must be present on the surface.

Another important method to identify the presence of chemisorbed hydrogen on graphite is by looking at possible atomic structures, previously identified [32]. In Figure 4.4a two dimers type A can be easily identified, while in Figure 4.4b a dimer B was identified. The type A and type B dimers are exemplified in Figure 2.4 of this thesis. The topography cross section above the structure, as indicated by the solid line

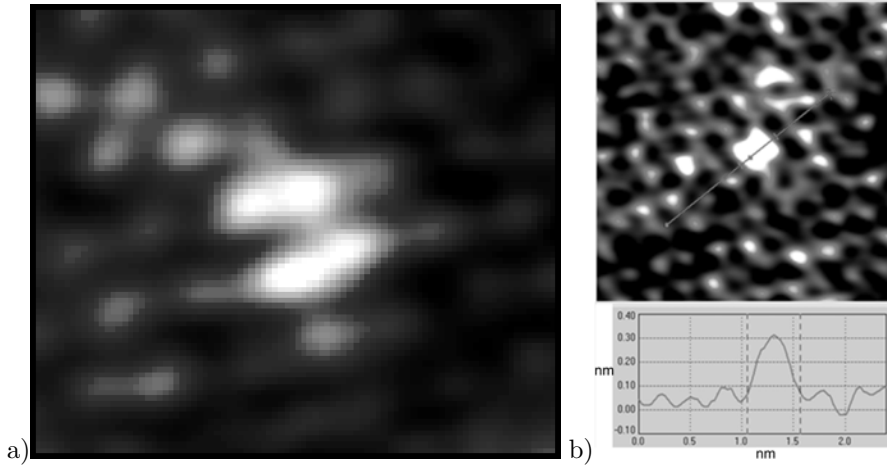


Figure 4.4: STM topography of: a) 2 dimers A (scan size: $2.5 \times 2.5 \text{ nm}^2$) and b) dimer B (scan size: $5 \times 5 \text{ nm}^2$), the corrugation of the hydrogen structure is, as it can be seen from the cross section of the topography, 0.3 nm; The scanning parameters are: $V = 120 \text{ mV}$, $I = 0.45 \text{ nA}$.

in Figure 4.4b, depicts a corrugation of about 0.3 nanometers, in close concordance with DFT calculations [33].

Based on STM topography results and on desorption experiments we show that upon hydrogen chemisorption the surface remains undamaged by the hydrogen deposition and also, previously reported structures of hydrogen on graphite are reproduced. One step further can be made to identify possible H positions on graphite for other structures observed in topography. Figure 4.5 depicts the hydrogen positions on a graphite lattice (right hand side images) in concordance to the topography results (left hand side images). The possible structures are identified by assuming that all the hillock features are due to chemisorbed H and that the atomic positions available to H chemisorption follow the rules described by Otero et al. [32]. By measuring the distances between the two types of dimers or single H positions the possible structures may be identified. To correctly identify H structures composed of three or more H atoms in close proximity more detailed studies are needed, but have not been pursued during this work. Occasionally, single H atoms (Figure 4.6a) have been identified on the graphite lattice. Single H atoms chemisorbed have been observed only at very low H coverage. It is safe to conclude that what we observe is a single H atom due to the triangular topographical appearance. STM simulated topography performed by Ž. Šljivančanin [35] and depicted in Figure 4.6b show a remarkable resemblance.

HOPG presents large (squared micrometers) flat atomic terraces but also step

4. The role of H-adsorbed atoms on graphite: zero bias anomaly in the density of electron states

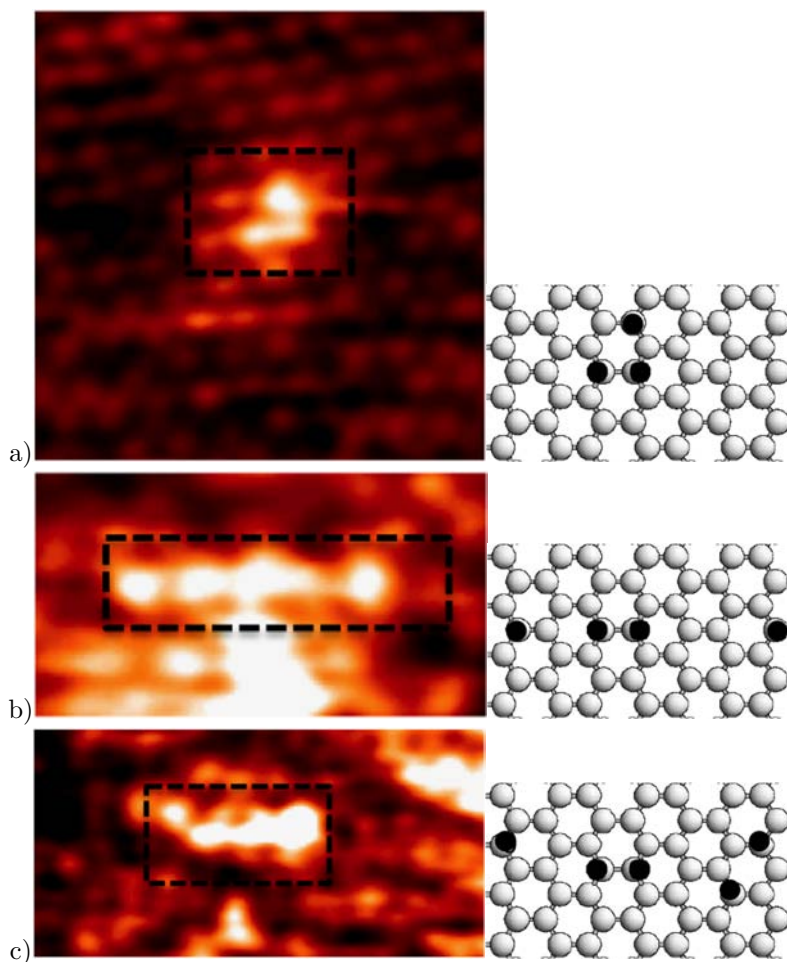


Figure 4.5: Possible hydrogen structures marked by the dashed black rectangle composed of three (a), four (b) and five (c) hydrogen atoms positioned as depicted in the right hand side of every image. The scan sizes are: a) $2.1 \times 2.1 \text{ nm}^2$, b) $1.8 \times 0.9 \text{ nm}^2$ and c) $2.5 \times 1.2 \text{ nm}^2$.

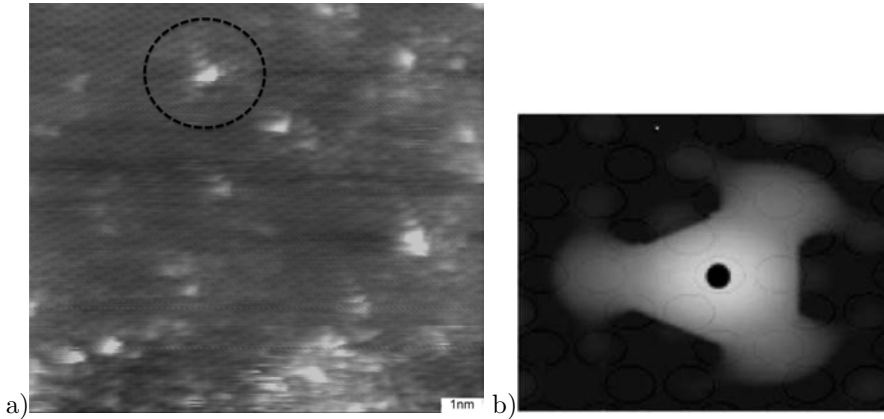


Figure 4.6: a) Single hydrogen atom chemisorbed on graphite marked by the dashed black circle. Within 1 nm from the single hydrogen chemisorbed the $\sqrt{3} \times \sqrt{3}R30^\circ$ reconstruction can be observed. b) STM simulated topography of a single H chemisorbed on graphite, density of states: 10^5 at a voltage of 0.1 eV.

edges and grain boundaries. Close to them, localized electronic states derived from the armchair or zigzag edges, defects are present in the LDOS of graphite at distances of up to 4 - 5 nanometers [34]. Since we are interested in the modification of the electronic structure properties of graphite upon hydrogen chemisorption all the spectroscopic data that is going to be presented in this thesis were collected at distances larger than 50 nanometers from step edges or grain boundaries.

4.3.2 Changes in the LDOS of graphite induced by H

The electronic structure properties of hydrogen modified HOPG (0001) are presented and discussed in the following two sub-sections. Scanning tunneling spectroscopy (STS) has been performed at two different levels of hydrogen coverage, 0.01 and 0.2 ML. The experiments have been performed at various temperatures, ranging between 4 K and 120 K. The majority of the results have been obtained at 4 and 77 K. The scanning tunneling spectroscopy data is presented as function of the distance from the hydrogen patches as well.

Before proceeding with the LDOS studies of the H/HOPG system, STS measurements on clean graphite were carried out at 77 K (Figure 2.2b) and 4.8 K, Figure 4.7. These typical STS curves for clean graphite match previously reported theoretical and experimental data [36].

4. The role of H-adsorbed atoms on graphite: zero bias anomaly in the density of electron states

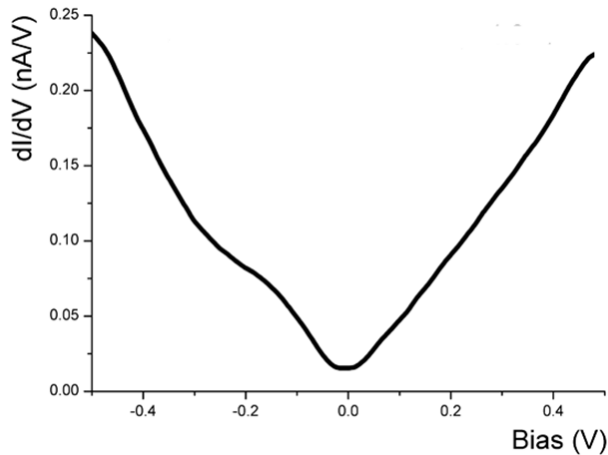


Figure 4.7: STS between -0.5 V and 0.5 V on clean graphite indicating a smooth density of states, acquired at 4.8 K. $V_{ref,RMS} = 8$ mV, $f = 730$ Hz.

V - shaped gap at the Fermi level

After hydrogen deposition, STS at 77 K was used to probe the density of states of graphite as function of distance from the hydrogen structures. The data were consistently reproduced in several experiments, with different W or PtIr STM tips, on ZYA or ZYH quality graded HOPG. In Figure 4.8a are two positions depicted: one very close (less than 1 nm away) to a hydrogen patch (black rectangle) and one at approximately four nanometers away from any hydrogen structures. In Figure 4.8 the STS spectra reveals an unexpected feature centered around the Fermi level. This V-shaped feature is unexpected since the density of states within the gap presents a smooth, linear dependence with the energy. A net zero conductance is measured at the Fermi level. Thus, this feature will be referred to as V-shaped gap.

The width of the V-shaped gap is about 90 meV. If the distance between the H structures and the position where the STS data is acquired is increased, the density of states of unperturbed graphite is measured, as exemplified in Figure 4.8c. The V-shaped gap is a local effect since the LDOS of graphite returns to the bulk graphite LDOS within 4 nanometers away from hydrogen patches. The hydrogen coverage for the data presented in Figure 4.8 is estimated to about 0.2 ML. The coverage is calculated by estimating the relative size of the hydrogen patches when compared to the total STM scan size and finally correlated with the crystallographic structure of a graphite layer. The number of hydrogen atoms is roughly estimated from the surface area of dimers, as measured from Figure 4.4.

The particular shape of the V-shaped gap motivated us to proceed with a more

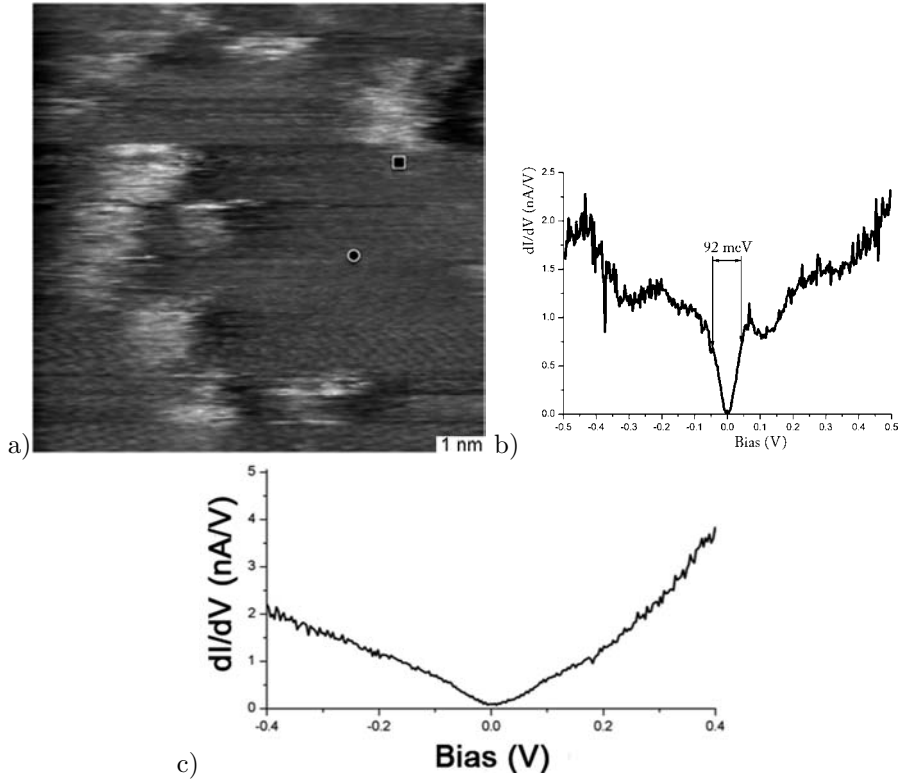


Figure 4.8: a) 77 K STM topography of H/HOPG, $10 \times 10 \text{ nm}^2$. The black rectangle depicts the location of the STS spectra in b) while the black circle is the position of the STS presented in c); b) STS spectra depicting a V-shaped gap at E_F with a width of 92 meV, acquired at less than 1 nm away from a hydrogen patch. c) STS spectra acquired at $\approx 4 \text{ nm}$ away from any hydrogen patch. $V_{ref,RMS} = 4 \text{ mV}$, $f = 873 \text{ Hz}$.

4. The role of H-adsorbed atoms on graphite: zero bias anomaly in the density of electron states

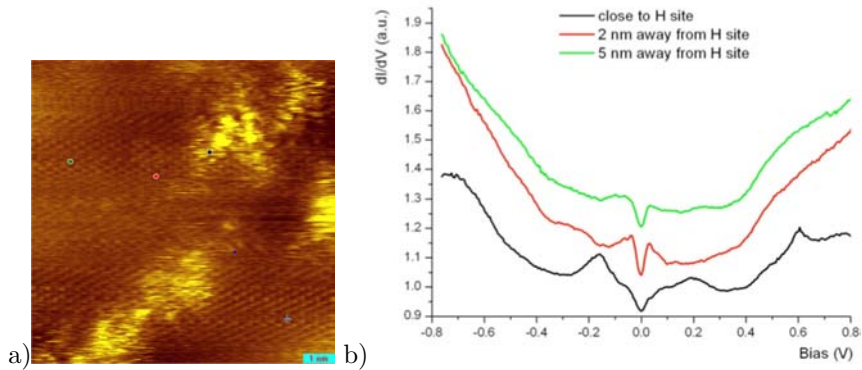


Figure 4.9: a) STM topography at 5 K of H/HOPG, $10 \times 10 \text{ nm}^2$. The colored circles correspond to the same colors with which the STS data in b) are represented. The distance from the hydrogen structures can be read in the upper right part of the b). $V_{ref,RMS} = 4 \text{ mV}$, $f = 972 \text{ Hz}$.

detailed investigation. The experiments were intended to explain under which conditions a gap develops and to ultimately understand the physical mechanism governing its appearance. The following questions can be addressed. Is the opening of the gap temperature dependent? Is the size of the gap temperature dependent? Is the spatial extent of the gap temperature dependent? A series of experiments were conducted to answer to all these questions.

First, the coverage of the sample was kept in the same range since the gap might be a function of both coverage and temperature. Although the coverage cannot be easily quantified, we maintained a constant sample exposure time to the hydrogen plasma. At 5 K, spatially resolved STS indicates the presence of a similar gap, as shown in Figure 4.9b. While very close (less than 1 nm away) to the hydrogen patch a similar gap. Even more interesting, the gap is present even at large distances, as it can be observed from the STS data presented in Figure 4.9b with the solid green line. Summarizing, at 5 K, the gap is observed at larger distances than measured at 77 K, which means that the spatial extent of the gap is larger at lower system temperature.

In addition to the gap, very close to hydrogen patches, extra electronic states are present (at energies around $\pm 200 \text{ meV}$), see Figure 4.9b, the solid black line. Although it is difficult to make a one to one correlation with LDA calculations for H atom, dimer A and dimer B performed by Ž. Šljivančanin due to the complexity of the hydrogen structures that can be observed in Figure 4.9a, electronic contributions from a single H atom and dimer B on HOPG are expected to be present at around $\pm 130 \text{ meV}$ respectively, $\pm 500 \text{ meV}$. The results of the LDA calculations are presented in Figure 4.10. It may be the case that the electronic states at $\pm 200 \text{ meV}$ and at

4.3 Experimental results and discussion

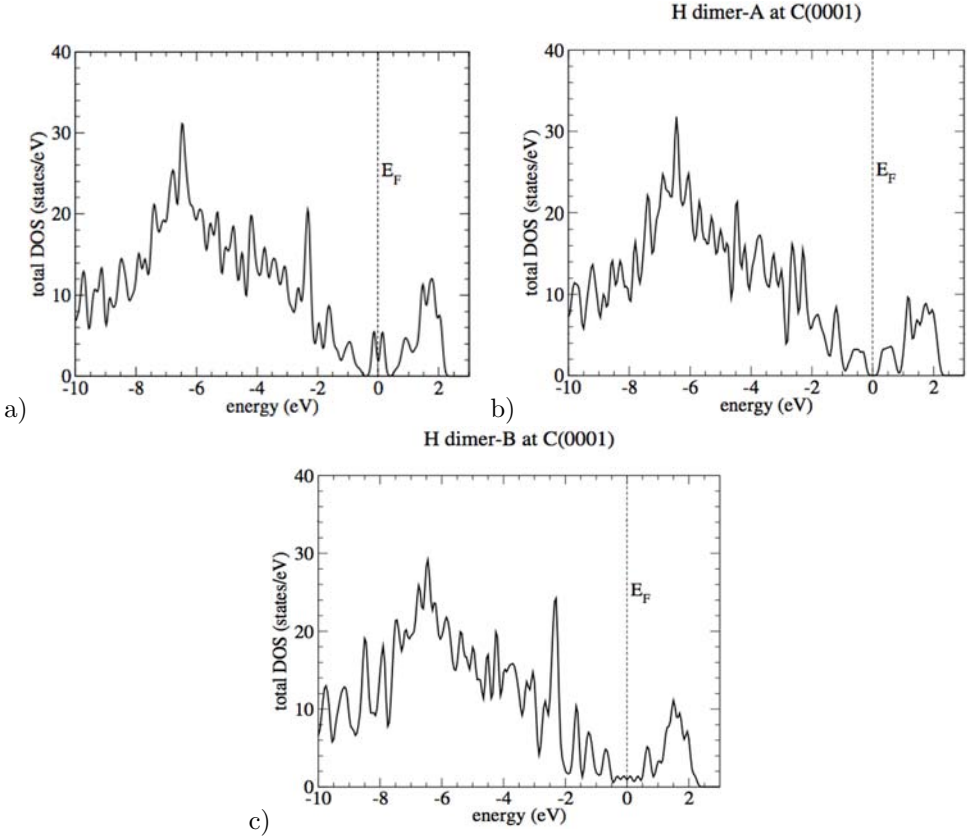


Figure 4.10: LDA calculations [35] of the TDOS for: a) single H on HOPG; b) dimer A on HOPG c) dimer B on HOPG.

+ 600 meV are for a H island composed of a single H next to a dimer type A since the values measured fit reasonably the LDA calculations, as shown in Figure 4.10. It is worth noticing that the LDA calculations do not predict the appearance of the V-shaped gap in the LDOS.

Second, a closer investigation of graphite density of states at 4 K (Figure 4.11) reveals that the observed gap is about 10 meV smaller than the gap size measured at 77 K. The presence of the V-shaped gap was measured up to 5.5 nm from the H patches. The exact spatial extent value was not measurable since the hydrogen islands were positioned at roughly 11 nm, furthest apart. Thus, it has been observed that upon temperature reduction the full-gap size is decreasing. Both curves from Figure 4.11 are spectroscopic data of the same point (3 nm away from a hydrogen island). It provides a good indication of the experimental setup stability during STS

4. The role of H-adsorbed atoms on graphite: zero bias anomaly in the density of electron states

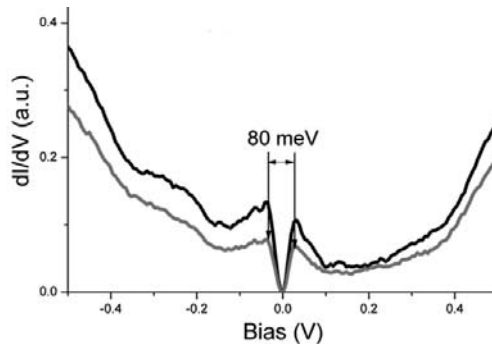


Figure 4.11: 80 meV full-gap measured with STS at 3 nanometers away from hydrogen structures on HOPG. Both lines depict the spectroscopic data acquired in the same position one after each other.

measurements.

Inelastic electron tunneling spectroscopy (IETS) was not pursued. However, since the V-shaped gap is relatively free of experimental noise, a mathematical derivative of one of the curves from Figure 4.11 was calculated. The derivative is presented in Figure 4.12. The two peaks with anti-symmetric intensity are symmetrically positioned around the Fermi level at about -16, respectively +16 meV. Table 2.1, which summarizes the vibrational modes of HOPG, indicates the presence of an out of plane acoustical phonon mode ($\text{ZA}(\Gamma)$) at 15 meV. This phonon mode has been observed for more than five mathematically derived STS curves.

Probing the LDOS of graphite at the same hydrogen coverage, but at 120 K, did not reveal the presence of this peculiar V-shaped gap. This is why STS experiments at temperatures above 77 K have not been further pursued.

Is it possible to measure the spatial extent of the gap by decreasing the amount H deposited on the graphite? To be able to answer this question a short exposure time of the graphite to the H plasma (8 sec) was used. In Figure 4.13a, a sample with low hydrogen coverage ($\simeq 0.01$ ML) has been scanned with STM. Easily observable, the hydrogen coverage in Figure 4.13a is lower than in Figure 4.8a) and b) while the distances between the hydrogen patches is for certain regions of the image larger than 20 nm. Since one might expect a random distribution of the H atoms on the graphite surface, it is important to notice that these large distances between the hydrogen patches are achievable due to the growth mechanism of H on HOPG (cluster formation) [31].

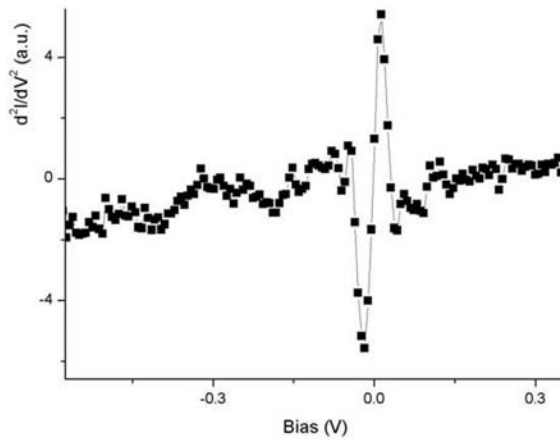


Figure 4.12: Mathematically derived IET spectrum from upper curve depicted in Figure 4.11. The most pronounced peak are located at -16, respectively +16 meV.

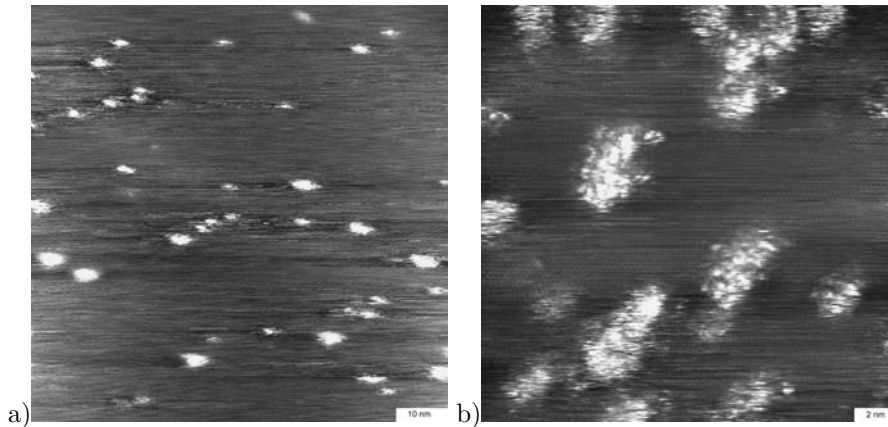


Figure 4.13: a) STM topography of $100 \times 100 \text{ nm}^2$ of H on HOPG. The estimated coverage is 0.01 ML, obtained for 8 s sample exposure to the H plasma. b) $20 \times 20 \text{ nm}^2$ topography of hydrogen islands surrounded by clean graphite regions supporting the island growth mechanism [31].

4. The role of H-adsorbed atoms on graphite: zero bias anomaly in the density of electron states

Sharp localized state in the LDOS of graphite

Interestingly, at 5 K with 0.01 ML H coverage the V-shaped gap was no longer observable, but around the Fermi level ($\simeq 80$ meV) a different feature was present. In Figure 4.14, the new feature in the density of states is illustrated at two experimental temperatures, 4 K and 77 K. Additionally, the feature in Figure 4.14b was less frequently measured than the V-shaped gap for the HOPG samples that had higher hydrogen coverage (0.2ML, as in the previous section), but was never observed at 5 K (for the same coverage). The spatial extent of this new state in the LDOS varies as a function of temperature, from more than 10 nm at 5 K to less than 3 nm at 77 K.

Thus, it has been observed that by reducing the amount of chemisorbed hydrogen on graphite a new feature is present in the LDOS, around the Fermi level. The energy window (within 200 meV around the Fermi level) in which these two peculiar LDOS features appear suggests that a transition may occur between the two upon a variation in hydrogen coverage of the sample. Still, the question regarding the spatial extent of these peculiar features in the LDOS of hydrogen treated graphite remains. In order to obtain a clear estimation of the spatial extent, a new experiment was proposed. Within the low sample coverage regime, STS experiments at intermediate temperatures (55, 30 and 15 K) were performed. A similarly shaped state was measured around the Fermi level. The results are depicted in Figure 4.14 and the results are plotted in Figure 4.16. For convenience, the spectra are shifted in respect to each other. It is important to notice that by increasing the distance from a hydrogen patch, the amplitude of the peak close to E_F decreases. Furthermore, as function temperature, the spatial extent of the state decreases upon temperature increase, from $\simeq 8.2$ nm at 15 K to $\simeq 2$ nm at 77 K. The distance where the amplitude of the peak tends to zero represents the spatial extent of the state. The next spectroscopy curve, acquired between 0.2 and 0.5 nm away from the last spectra where a peak in the DOS at the E_F was still observable, represents itself as the LDOS of clean graphite. Both the tunneling current and the bias voltage were kept constant for a specific temperature during the data acquisition.

Additionally, at 55 K (Figure 4.16c) STS curves were acquired at the same distance for a hydrogen patch, but in various directions (arbitrarily denoted as left, below or above, yet disposed in respect to each other under an angle of 90 or 180 degrees). For example, at 1 nm away from the hydrogen patch the STS curves show a strong resemblance in both peak intensity and peak position. This observation suggests that at this hydrogen coverage and at these experimental distances, there is no preferential direction of the underlying effect responsible for the appearance of this state that might be related to the crystallographic structure of graphite.

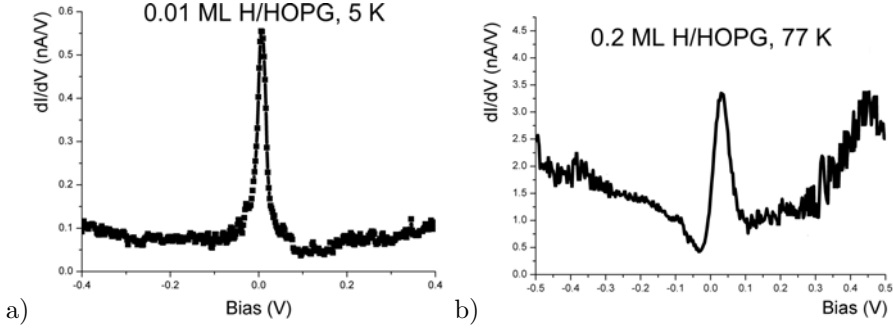


Figure 4.14: a) STS data acquired at 12 nm away from a H patch, at 5 K, depicting a sharp state close to the Fermi level. b) Same as a) but acquired at 1 nm away from a hydrogen patch at 77 K.

The interference state depicted in Figure 4.14b has been fitted with equation 2.5.1. The fitting parameters are: $E_{res} = 43 \text{ meV}$, $\Gamma_{res} = 80 \text{ meV}$ and $q = 1.31$. The Fano line profile describes well the interference feature observed.

Summarizing the experimental observations, at low hydrogen coverage (0.01 ML) on graphite and at various temperatures (5 K up to 77 K), the spatial extent of this peculiar state next to the E_F was determined. The spatial extent of the state increases with temperature decrease, as observable in Figure 4.17.

The STS data presented so far have been acquired on the graphite surface, in the vicinity of the hydrogen patches. Spectra acquired on top of a hydrogen patch are depicted in Figure 4.18. From previous experimental and theoretical work, it is expected that the most energetically stable dimer (thus highest occurrence rate) is dimer A (TDOS in Figure 4.10, dimer A exemplified in Figure 4.4a and Figure 2.4a, c, e) [31]. The LDA calculations predict a gap of about 400 meV while our measurement results on a gap of about 500 meV. Although there is not a 1:1 correlation, it is important to mention that the spectroscopy position was at a hydrogen patch edge and not on an isolated A-type dimer. A more detailed LDOS study of the hydrogen structures was not explored due to the structural complexity of the hydrogen patches (i.e. Figure 4.13b) which in turn impairs a good statistical analysis of the STS data. Future experimental work could reduce further the H coverage levels making easier to study the LDOS of hydrogen structures such as, single H atoms or dimers chemisorbed on HOPG. These experimental results could be correlated with the already available theoretical calculations.

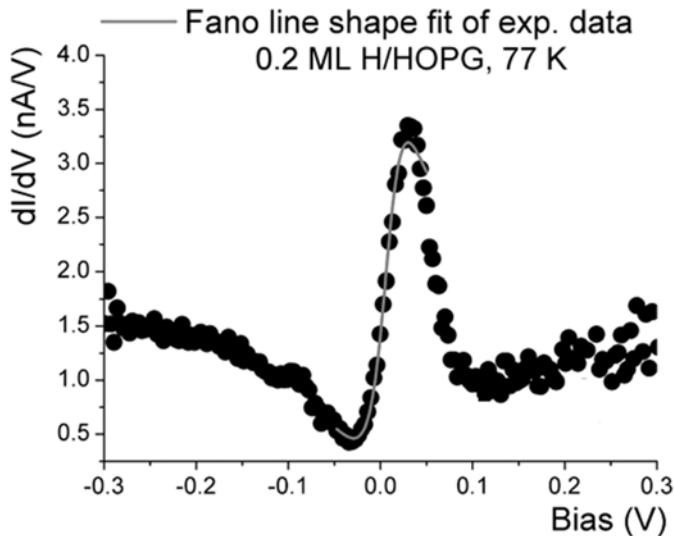


Figure 4.15: dI/dV spectra on graphite at less than 1.5 nm away hydrogen patch acquired at 77 K and fitted with the Fano formula (fitting depicted with the solid continuous line).

4.3.3 On the origin of the V-shaped gap and of the sharp localized state

To summarize the experimental observations, in addition to pure electronic states (Figure 4.9, lowest curve, -180, 200 and 600 meV peaks) upon hydrogen treatment of the HOPG (0001) surface, two different peculiarities in the LDOS of graphite have been observed. One represents itself as a V-shaped gap (i.e. Figure 4.11) while the other one is a pronounced, sharp state (i.e. Figure 4.14) to which we shall refer as being an interference state. Both are temperature dependent and H coverage dependent. The size of the V-shaped gap increases with about 10-12 meV for a temperature increase between 5 K and 77 K. Both, the V-shaped gap and the interference state can be observed further and further away from the hydrogen patches when the temperature decreases. The spatial extent of the interference state as a function of temperature has been summarized in Figure 4.17. With increasing hydrogen coverage on HOPG a transition between these two features is observed in the LDOS of graphite. At relatively low hydrogen coverage (0.01 ML) the interference state is predominant while at 0.2 ML the V-shaped gap dominates.

The electronic and vibrational properties of HOPG (0001) have been described in Section 2.1 of this thesis. Inelastic tunneling spectroscopy (IETS) measurements

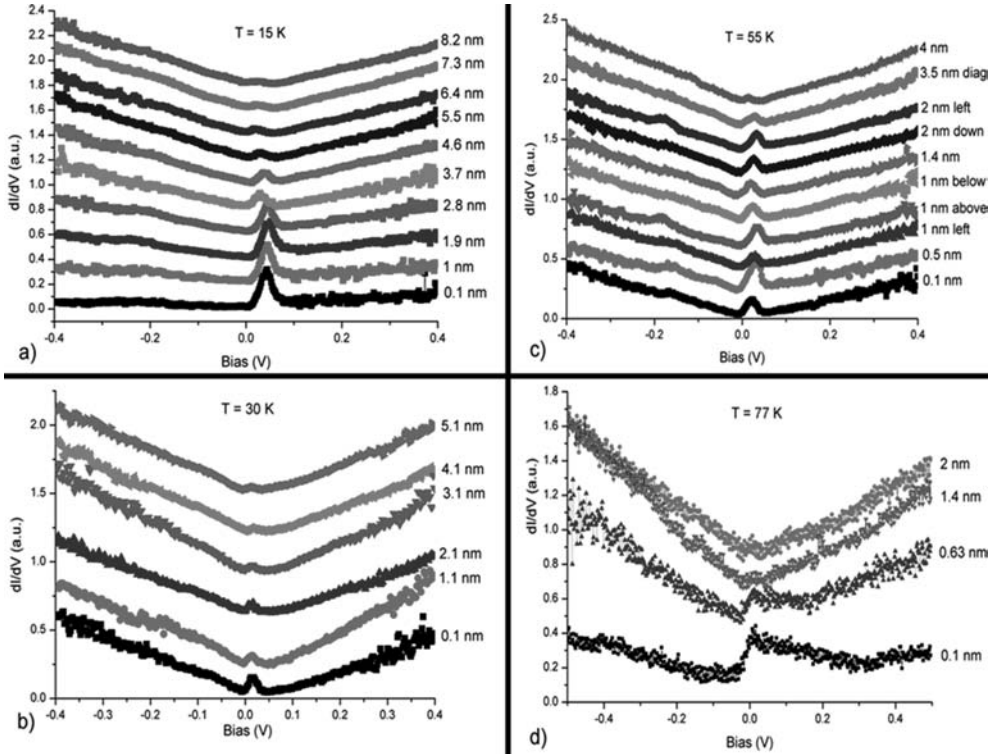


Figure 4.16: STS data acquired for 0.01 ML H/HOPG indicating the amplitude of the sharp state at the Fermi level as a function of distance from a hydrogen patch at the following temperatures: a) 77 K; b) 55 K; c) 30 K and d) 15 K. On the right hand side of each graph, the distance in nm between the hydrogen patch and the location where the spectrum was acquired is given.

4. The role of H-adsorbed atoms on graphite: zero bias anomaly in the density of electron states

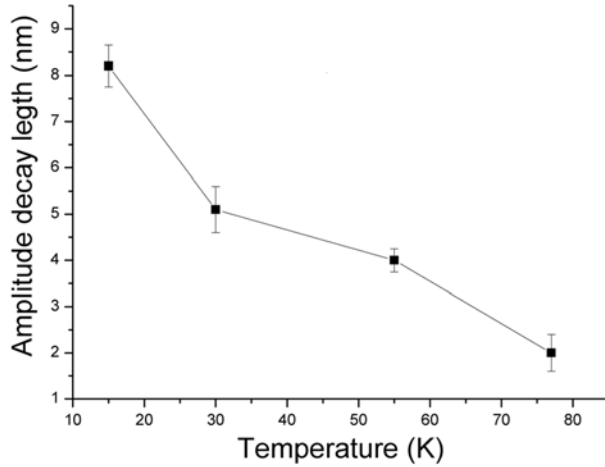


Figure 4.17: Spatial extent of the sharp state function of temperature measure with STS between 15 K and 77 K.

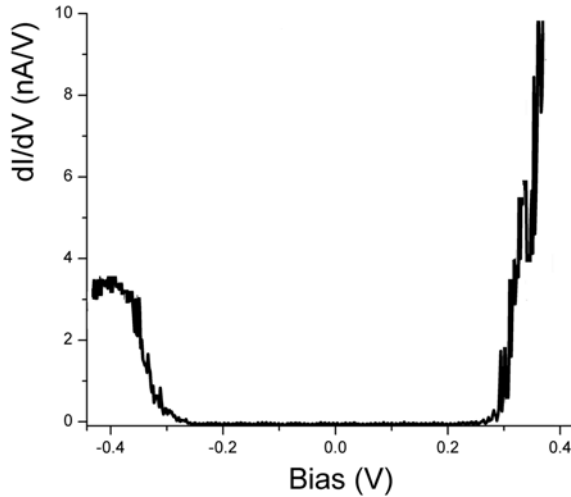


Figure 4.18: dI/dV spectra on top of a hydrogen patch. The DOS presents a band gap of ≈ 500 meV.

[37] and temperature dependent high resolution electron energy loss spectroscopy (HREELS) [38] reveal the presence of a 3D plasmon in graphite. The plasmon energy is 53 meV at room temperature (HREELS) and 40 meV at 6.5 K (IETS). From the HREELS data, the plasmon energy is expected at about 45 meV at 77 K. The variation in plasmon energy function of temperature is related to the semi-metallic character of HOPG. In general a semi-metal is characterized by a low number of charge carriers (about 10^{-5} electrons per atom). Jensen et al. [38] explained the plasmon energy shift by additional charge carriers thermally excited in graphite from the valence band to the conduction band. The 5-6 meV shift in the plasmon energy between 4 K and 77 K matches very well with temperature dependence observed for the edge of the V-shaped for the same temperature range. This 1:1 correlation is a hint that actually the V-shaped gap is delimited by the bulk HOPG plasmon.

Graphite can also be considered a layered electron gas (LEG) since the in-plane reduced electron mass is about 5×10^{-2} of the electron rest mass while the out of plane reduced electron mass is about 10 times the electron rest mass [58]. Yet, in a LEG the charge carrier system is in an intermediate state between a three-dimensional and a two-dimensional electron gas [59–61] where the 3D plasmon spectrum is characterized by an energy gap at $p = 0$ (with p the plasmon momentum) $\omega_{p=0} = \omega_0$. ω_0 is the plasma frequency, $\omega_0 = \sqrt{\frac{4\pi n e^2}{m}}$ where n is the charge carrier concentration and m is the electron mass. In a true two-dimensional carrier system, there is no energy gap and the plasmon frequency shows a square root behavior with the plasmon momentum [62]. The interlayer Coulomb interactions lead to the formation of plasmon bands, $\Omega(k, k_z)$, where k and k_z are the in-plane and perpendicular to plane wave vectors [61]. Kresin has also calculated the dispersion relation of plasmon density of states for a LEG:

$$\Omega(k, q_z) = \sqrt{s^2 k^2 + \frac{2\pi n e^2}{m} \frac{c k \sinh(kc)}{\cosh(kc) - \cosh(q_z c)}}, \quad (4.3.1)$$

where $s \simeq v_F$ and c is the interlayer distance.

There are several scenarios to explain the underlying mechanism responsible for the appearance of the V-shaped gap and the Fano interference. These scenarios are given below.

A first scenario involves an electron-phonon/plasmon coupling. Tediosi et al. have investigated changes in the plasmon frequency function of temperature induced by charge transfer between hole and electron pockets in bismuth, a LEG system [64]. They also treat graphite as LEG. They proposed a new type of quasi-particle, entitled plasmaron. It describes in LEG the interaction (scattering/coupling) between electrons and plasmons. The sharp peak in the Figure 4.14a can be the signature of

4. The role of H-adsorbed atoms on graphite: zero bias anomaly in the density of electron states

a the singularity of the one-dimensional plasmon DOS at both boundaries (U and L) of the LEG plasmon [61] which couples to the electron states. The L brach corresponds to the pure 2D plasmon and the U branch corresponds to the pure 3D plasmon. This might imply that an interaction between the L branch and a phonon would provide reasonable peak intensity. One available phonon mode is the 15 meV acoustic phonon of graphite, phonon mode reasonably dispersion-less at the Γ point. The modes would not cross but would split off from each other by a specific amount determined by the coupling strength. The interaction between the phonon branch and the acoustic plasmon can result in a dispersion-less 2D plasmon contribution with a gap in between. The size of the gap is determined by the strength of the coupling. Thus, the STS spectra might be explained by the presence of a strong peak close to 16 meV. A strong electron-phonon (acoustic at about 15 meV) coupling was attributed as the mechanism producing a well-defined quasi-particle peak in photoemission experiments on graphite at 20 meV [66]. The same photoemission experiments, showed a linear energy dependence of the quasi-particle scattering rate, an indicative of a deviation from the conventional Fermi liquid behavior.

At lower hydrogen coverage and at 5 K, a sharp localized state (Figure 4.14a) was measured 12 nm away from the H patch. This localized state changes its Fano line profile (Figure 4.14b) when increasing the temperature. Such a localized state is proposed up to a coverage of 90% hydrogen on HOPG [67]. The spatial extent of the localized state (12 nm or about 48.6 graphene lattice constants) is more difficult to understand, Figure 4.14a. However, Ruffieux et al. have observed standing waves extending for 25 graphene lattice constants in the local density of states of graphite induced by the backscattering of the electron wave functions at individual defects [69]. Their experiment was performed at room temperature. Since the electron mean free path is increasing with decreasing temperature, it may be expected that this C-H localized state might be visible even at 50 graphene lattice constants away. Upon temperature increase, a transition in between a localized state (visible at 4-5 K) to a Fano line profile might be triggered by an increasing number of charge carriers by thermal excitation. Still, the number of charge carriers is sufficiently low for the effect to be visible at 77 K. The decreasing special extent of the Fano signature, coupled with the change in the Fano line profile (Figure 4.16), is an indication that the number of free charge carriers is increasing with temperature and the charge depleted region is decreasing with temperature increase.

From studies of chemisorbed hydrogen on graphene [63,65] and chemisorbed hydrogen on bilayer and tri-layer graphene [67] a very localized state due to the C-H bond is shown at the Fermi level. The width of this state is slightly increasing if the interaction between graphene layers is enhanced and by increasing the hydrogen

coverage [67]. Thus an impurity band is formed at the Fermi level. In addition, the peak intensity is rising while the charge depletion region is increasing around the hydrogen patches [65]. From the electronic structure properties point of view, bilayer or tri-layer graphene behaves similar to graphite [68], thus one can expect that a similar behavior as described above is expected when H is chemisorbed on graphite. Thus, we expect that at relatively large hydrogen coverage on graphite the concentration of conduction electrons is small and an electron-depleted area around the hydrogen patches is created. It can be proposed that the V-shaped gap is observable below the 3D plasmon value of 40 meV at 5 K since there is no or small tunneling probability into the localized C-H electronic state at the Fermi level. Only phonon or LEG plasmon band tunneling assisted tunneling can occur. The net results of such an assisted tunneling can be the V-shaped gap that was experimentally measured. Indeed, Figure 4.12 reveals a strong contribution at 16 meV, the energy at which the out of plane acoustic phonon mode of HOPG lies.

Still, it is possible that the interference state is measured over the entire temperature range, from 4 K up to 77 K and the localized state is not visible. The localized state proposed by Yuan et. al. [67] is interacting with the free graphite electrons. The possibility of tunneling into the localized state and the continuum (the sea of free electrons) is quantifiable from the shape of the Fano resonance. As plotted in Figure 2.12, the Fano factor (q), is larger when tunneling occurs more into the localized state than in the continuum. Comparing the interference states measured and depicted in Figure 4.14 and Figure 4.16 the q factor seems to decrease when increasing temperature and/or distance. For example, at 77 K (Figure 4.14b) the q factor is just above 1 while at 5 K, the q factor is larger than 3-4. Fano factor values smaller than 1 translate in a dip around the resonant energy level. However this can not explain the V-shaped gap since the depletion region is higher at 4 K (Figure 4.11) thus it will be expected a Fano factor higher than 1, even higher than the q factor corresponding to the line shape depicted in Figure 4.14a. Thus, it is also proposed that by increasing the hydrogen concentration an electronic transition between the interference process (described as a Fano interference) to a plasmon and/or phonon assisted tunneling process occurs.

An alternative scenario for the appearance of the V-shaped gap is related to a possible Coulomb gap. The V-shaped gap might be a signature of a Coulomb gap. As mentioned in Section 2.4 of this thesis, in an under-screened regime and in the present of impurities electron-electron interaction effects are enhanced. Efros and Shklovskii proposed that for a Coulomb correlated system the density of states at the transition between metal and insulator will present a gap at the Fermi level with a shape dependent on system dimensionality [22]. Since graphite can be considered

4. The role of H-adsorbed atoms on graphite: zero bias anomaly in the density of electron states

quasi two-dimensional, the Coulomb gap should be linear. The first experimental observation of the LDOS linear behavior function of energy in a 2D system was made by Mark Lee et. al. [70]. They studied Si:B crystals. The boron doping was varied between 80% and 110%, while the experimental temperature was varied between 0.1 K and 10 K. In our experiments the doping levels are really low when compared to the experiment of Mark Lee et. al. They observed gap sizes of about 0.5 up to 1.6 meV. They also noticed a temperature dependence of the gap (apart from the thermal broadening). The Coulomb gap becomes wider and deeper as the temperature decreases. They showed it has a quadratic dependence on temperature. However we have observed that the gap size decreases function of temperature from 90 meV to 80 meV and is not increasing. This aspect strongly contradicts the hypothesis that this might be a Coulomb gap.

Another scenario possibly responsible for our observations involves the presence of supercritical impurities in graphene. As described by Shytov et al. [71, 72], charge impurities in graphene can generate a large family of Rydberg-like resonance states of massless Dirac particles. The Rydberg-like resonance states appear due to the strong coupling between the impurity states and the Dirac continuum states. Creating the impurity states is possible only if charge above the critical value, $\beta=0.5$, is available. It is known that H/HOPG results in very sharp electron states near the Fermi level [67]. Upon a single H chemisorption the HOPG lattice is relaxed by C-atom puckering with 0.3 Å [40]. Let us assume that this local puckering electronically decouples the top graphite layer from the bulk of the sample. In other words, the top layer to consider it graphene like. The relative permittivity of graphite is about 2.5 times larger than for graphene. When considering that all the impurity screening is solely done by the graphene/graphite electrons, the β value 2.5 times larger for graphite at the same Z_c equal to 1. Since we observe in our experiments a Fano localized state that is dependent on both temperature and distance from the H-patches we can state that screening in the H/HOPG system can be tuned. If the vacuum polarization and screening properties of graphene are valid for our system (H/HOPG), we propose the following. The LDOS for a supercritical charge impurity shows a resonance state at the Fermi level [72]. The results of Shytov also show that this resonance level should be visible over large distances, as we observe in Figures 4.14b and Figure 4.16. The change of the Fano shape might be induced by a change in the local screening of the impurity, as i.e. an increase in the π -plasmon screening upon temperature increase. An increase in the screening will decrease the β , thus moving the system away from the strong tunneling coupling regime. If the distance from the H-patch is increase the required screening is less and less, thus the H/HOPG system would leave the supercritical regime.

4.4 Charge density/mobility measurements of hydrogen treated graphite

From all the above-mentioned scenarios we consider that the electron - 2D plasmon coupling is the most likely cause of both the V-shaped gap and the Fano contribution. If the electron-phonon contribution would be strong in the conductance plots, the higher harmonics of this resonant tunneling would be most likely also observable, while they are not (Figure 4.14a). As function of temperature we also do not expect a drastic change in the electron-phonon coupling. Yet, when comparing Figure 4.14a and b, we observe that the position of the resonant state (equation 2.5.1) for the Fano line contribution is changing from about 4 meV (measured at 4 K) to about 45 meV (measured at 77 K). The transition between the Fano contribution and the V-shaped gap could be understood by considering that at higher hydrogen coverage, the 2D plasmon contribution for impurity screening becomes smaller and smaller. At this relatively high hydrogen coverage (0.2 ML) the HOPG acoustic phonon mode (16 meV) has also been observed, (Figure 4.12). Most likely only phonon and plasmon assisted tunneling is possible below the bulk HOPG plasmon energy (40 meV at 4 K).

4.4 Charge density/mobility measurements of hydrogen treated graphite

Since the results depicted in this chapter indicate changes in the LDOS of graphite upon hydrogen chemisorption is of interest to test if these changes have any influence on the macroscopic electronic behavior of HOPG. As presented, at a nanoscopic scale a Fano interference, a pseudo V-shaped gap or a band gap is opened. If these nanoscopic effects will manifest when measuring HOPG samples of about $15 \times 15 \text{ mm}^2$, it is expected that an increase in resistance will be measured as a function of sample temperature. The results on H-modified samples have to be benchmarked against clean HOPG samples.

4.4.1 Experimental procedure

The sample preparation procedure was kept constant during all the measurements described in this section. HOPG (0001) is cleaved under ambient conditions, prior to the application of contacts on top of the freshly exposed graphite surface. The contacts are positioned as exemplified in Figure 4.19. The position of the contacts on the sample is chosen to minimize artifacts induced by electric field inhomogeneity.

The contacts are made using very small droplets (two up to two-three millimeters in diameter) of silver glue placed on the sample surface with a relatively sharp needle. In the silver glue solution conductive copper wire, $d = 100 \text{ }\mu\text{m}$ are placed. Afterwards, the sample is left for approximately half an hour for the silver solution to dry and make reliable contacts between the graphite samples to be measured. The contact resistance

4. The role of H-adsorbed atoms on graphite: zero bias anomaly in the density of electron states

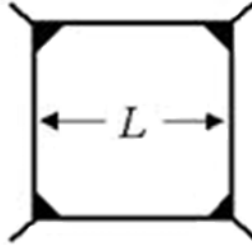


Figure 4.19: Contact geometry for the squared HOPG sample. L represents the sample size, 10 mm.

is measured before proceeding to the actual measurements. If the contact resistance showed deviations larger than 5% of the mean resistance, the sample was discarded. For the samples that contained hydrogen, the electrical contacts have been created either before, either after the hydrogen treatment. Creating the electrical contacts on the HOPG before the hydrogen chemisorption allows the measurements to be made for surface before and after hydrogen chemisorption. The reason to hydrogen treat HOPG with the silver contacts on will become obvious in the following section of this chapter.

4.4.2 Experimental results and discussion

Only the top layer of HOPG is chemically modified and not the entire sample since it is expected that hydrogen does not diffuse into the bulk of the HOPG, but rather binds at the surface.

The experimental setup and the theoretical considerations are described in Section 3.4 of this thesis. The setup can measure up to 4 samples in parallel. The first experimental runs involved measuring the resistivity and charge mobility/density on two samples treated with atomic hydrogen for 1 minute (about 0.2 ML of H) and two samples as reference. All the samples were ZYH quality HOPG. The resistivity measurements were not satisfactory since no particular trend was observable even when comparing the reference samples. The unmodified HOPG samples differed in the resistivity values one order of magnitude. For the hydrogen treated samples from 60 K to 4 K, the resistivity was decreasing for one sample, while for the other sample the resistivity presented a plateau. Furthermore, deviations from the initial resistivity curves were measured if the samples were left in the measurement setup for a longer time (e.g. 24 hours). In order to avoid the irreproducibility of the results it was decided to use only high quality HOPG (ZYA) samples. Additionally, the silver contacts were not removed during the H treatment and no cleaving of the HOPG

4.4 Charge density/mobility measurements of hydrogen treated graphite

surface was performed. This ensures measuring the same HOPG surface, H being the only addition between the measurements. The results became more reproducible and a set of this results for a single sample are depicted in Figure 4.20.

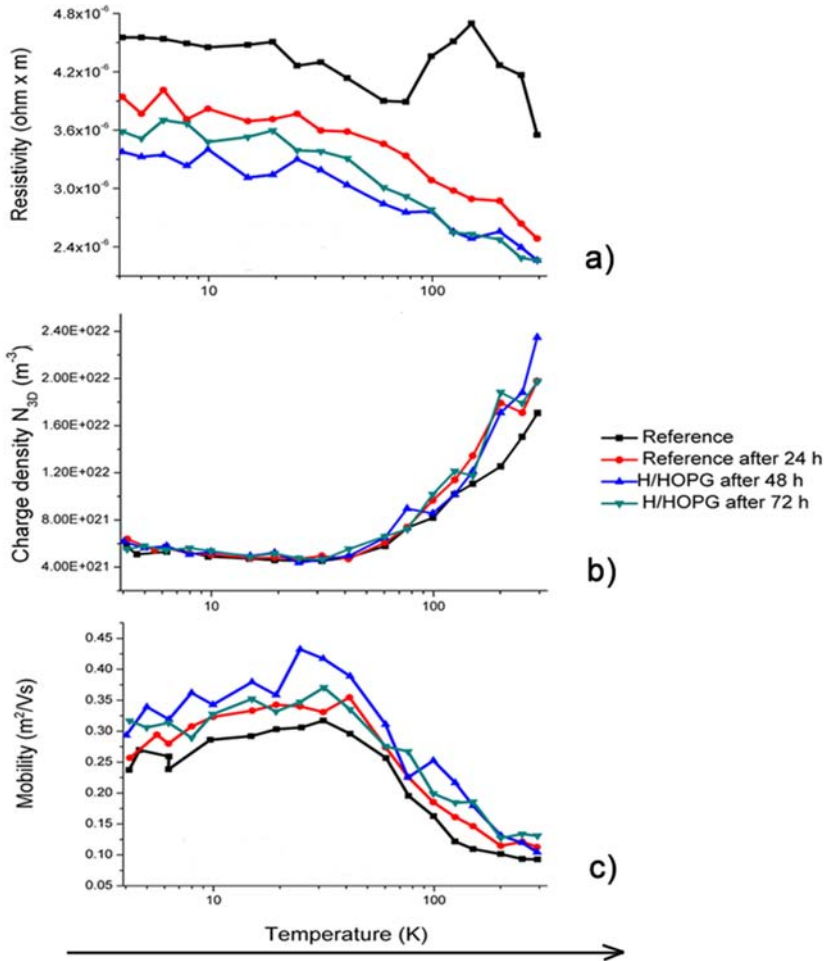


Figure 4.20: a) Resistivity measurement results on one samples (HOPG (ZYA), NTMDT) before and after hydrogen treatment. The value for the resistivity decreases after hydrogen exposure but also for the same reference after keeping it in a He environment for 24 hours. b) Mobility vs. temperature plot of the same sample presented in a). A slight apparent increase in the charge mobility is noticed. c) Charge density vs. temperature plot for the same sample described in a). No large differences between hydrogen treated and non-treated are observable. Note an increase in the sample s charge density from 20 K up to room temperature.

The results are obtained for a single high quality HOPG (ZYA) sample before and

4. The role of H-adsorbed atoms on graphite: zero bias anomaly in the density of electron states

after treatment. The time interval between the measurements was twenty-four hours for a reason that will be explained below. In between the measurements the sample was left in a He atmosphere, thus inert to the sample. The measured curves are the results of 18 data points/curve acquired for temperatures between room temperature RT and 4 K. The temperature scale is logarithmic.

The resistivity shows a decrease if the sample is left for 24 hours in the experimental setup. The first measurement showed an increase in the resistivity when going from 100 K up to RT, peaking at 180 K. After 24 hours, this peak is no longer observed in the next measurement of the same reference sample. Furthermore, the value of the resistivity at RT for the four measurements depicted in Figure 4.20 is not the same. The difference between the RT resistivity values diminishes after more than 24 hours. This observation implies that the sample resistivity is decreasing for the first 48 hours after cleaving. To understand the resistivity results for the H treated when compared to non-treated, the large difference between the reference resistivity measurements must be clarified.

Cleaving the HOPG sample with scotch tape induces in graphite mechanical stress in the surface and the planes underneath. Atmospheric gases can be trapped within the top graphite layers. As Martinez-Martin's scanning Kelvin probe microscopy (SKPM) results suggest [28], the surface and planes close to the surface are not in electrostatic equilibrium. While the trapped gasses escape from their pockets, the graphene layers reach an electrostatic equilibrium. If the sample has different local electrostatic potentials on a micrometer scale, then the local movement of charge is impaired. Hence, the resistivity of the material is increasing. With this qualitative explanation it is understandable that the resistivity of the HOPG sample decreases, after cleaving, until the sample reaches electrostatic equilibrium. The time scale until the surface reaches an electrostatic equilibrium is 21 hours at a pressure of 10^{-2} mbar [28]. Under atmospheric conditions, as in our case, the degassing time is larger than 21 hours since the pressure gradient is small towards non-existent. Since the resistivity difference is very small between 24 hours and 48 hours, the sample can be considered in electrostatic equilibrium after 24 hours. Important to notice is that the peak in the resistivity measured at 180 K for the first experimental run on the sample disappears completely after 24 hours, supporting the hypothesis that the sample is in electrostatic equilibrium 24 hours after cleaving. All the high quality HOPG samples presented an increase in the resistivity from RT to 20 K, where the resistivity reaches its maximum and then remains rather constant. The decrease in the resistivity can be understood accounting for the semimetal character of graphite, thus a rise in temperature implies an increase in the amount of thermally excited charge carriers. This is observed in Figure 4.20b, where the charge density is plotted against

temperature. Why does the resistivity show a plateau behavior in the 4 K to 20 K temperature interval? The electron's mean free path in HOPG is micrometers [56], comparable to the size of a grain. If an increase in the electron mean free path is no longer possible due to the grain boundaries, acting as scattering centers, a plateau behavior is expected. In other words, the electron transport within a graphite plane is ballistic up to the interface between the grain boundaries, where the charge is scattered. The charge scattering, attributed mainly due to the grain boundaries is experimentally confirmed by A.S. Bender et. al. [55]. For all the high quality samples measured before and after the hydrogen treatment, no significant difference of the resistivity was observed function of hydrogen coverage (0.01 up to 0.2 ML) and temperature. For example, as shown in Figure 4.20, the resistivity presents the same value at 8 K for both HOPG and H/HOPG. We expected that when hydrogen patches act as scattering centers, they would result in an increase in resistivity, but this is not observed experimentally. We speculate that our measurement method is not surface sensitive enough. Since only the top HOPG layer was modified by hydrogen chemisorption, a change in the resistivity cannot be observed. The mobility and charge density plots are related to the resistivity plot by formula 3.4.5. The charge density plot depicts a decrease up to 20 K, from which point a plateau behavior is observed up to 4 K. This result is consistent with the studies done by Jensen et. al. [38]. The mobility plot indicates the maximum value for the charge mobility at 20 K.

To summarize, the Hall probe measurements did not reveal noticeable differences between the HOPG and the H treated HOPG samples. In order to obtain reproducible results, the sample should first reach electrostatic equilibrium (more than 24 hours in ambient atmosphere). The same sample must be used (treated and non-treated), otherwise the results are not reliable since the crystallographic structure of graphite can vary much. Although the contacts were placed on the sample surface where the H treatment was performed, the measurement itself is sensitive to the bulk contribution, thus changes in the electronic structure properties of a single layer do not show up in our measurements. In order to check if any changes in the conduction properties are observable upon H treatment, we propose a measurement where either the contacts are created by lithography on the surface at small distances [56] or to replace the HOPG with graphene or bilayer graphene [57].

4.5 Conclusions

In this chapter we reported the results obtained on hydrogen chemisorbed on graphite. The samples have been studied mainly with STM, at temperatures ranging from 4 K

4. The role of H-adsorbed atoms on graphite: zero bias anomaly in the density of electron states

up to room temperature. The topology and the local density of states of clean and H functionalized HOPG samples have been studied.

For clean graphite, atomic resolution was achieved and the DOS was in good agreement with theoretical calculations and other experiments. Hydrogen has been controllably deposited on the HOPG surface, achieving hydrogen coverage between 0.01 and 0.2 ML. Removing the chemisorbed hydrogen in controlled desorption experiments revealed flat atomic terraces of graphite, free of structural defects. Previously reported metastable structures, dimers, have been observed. Isolated H atoms chemisorbed have been sporadically noticed only for low sample coverage and we have observed the island growth mechanism of hydrogen islands on graphite, consistent with reported theoretical and experimental work. We have also proposed structures consisting of 3, 4 or 5 atoms clustered together. The $(\sqrt{3} \times \sqrt{3})R30^\circ$ reconstruction pattern has been identified only at low coverage.

The local density of states of chemically modified graphite has been studied at the following temperatures: 5, 15, 30, 55, 77 and 120 K. Two particular states at the Fermi level attracted our attention. One of the states is a V-shaped gap and it was observed only at large hydrogen coverage on HOPG, especially at 5 K and with a low occurrence rate at 77 K. The other state that caught our interest manifested itself as a sharp state close to the Fermi level, predominantly localized in the empty states. Both states depend on temperature and hydrogen coverage. Upon decreasing the temperature both LDOS features become more pronounced in intensity and have a larger spatial extent. If the hydrogen coverage is low, only the sharp state is measured, while at 0.2 ML H coverage a transition between the V-shaped gap and the sharp state is noticed if the system temperature is increased from 5 K to 77 K. Mathematical differentiation of the dI/dV spectra of the V-shaped gaps results in clear IETS peaks, signature of the out of plane acoustic phonon of graphite. The V-shaped gap is limited in width by the 3D plasmon of graphite. Several physical mechanisms have been proposed to explain both states. To conclude, the linear density of state function of energy of the V-shaped gap indicates a Coulomb gap, originating from the reduction of 2D plasmon screening. This effect is not visible for the 0.2 ML coverage at 4 K where more localized electron states are expected due to the Coulomb gap, which would cause even an increase of the electron-phonon coupling. In the case of the low hydrogen coverage (0.01 ML), the electron-phonon coupling (linear to bare electron density of states) would increase, but also the 2D-plasmon density of states of the LEG. The fact that we do not see a strong IETS contribution on clean graphite at 15 meV (graphite phonon) indicates that the Fano shaped peak cannot be ascribed to an strong electron-phonon effect only, but that the difference in charge depletion around the H-clusters compared to clean graphite

points to the unique role of the 2d-plasmon of the LEG interacting with electrons in this layered compound.

Charge density/mobility measurements were conducted between 4 and 300 K. The method we used to test for hydrogen-induced changes in charge carrier mobility/density proved to be not sensitive enough to relate to the the surface effects seen in STM and STS . No significant difference has been observed between hydrogen treated and non-treated samples.

Bibliography

- [1] T. Valla, P.D. Johnson, Z. Yusof, B. Wells, Q. Li, S.M. Loureiro, R.J. Cava, M. Mikami, Y. Mori, M. Yoshimura, and T. Sasaki. *Nature* 417, 627 (2002).
- [2] H. Kempa, P. Esquinazi, and Y. Kopelevich. *Phys. Rev. B* 65, 241101(R) (2002).
- [3] P. Hawrylak, G. Eliasson, and J.J. Quinn. *Phys. Rev. B* 37, 10187 (1988).
- [4] Y. Kopelevich, J.H. Torres, R.R. da Silva, F. Mrowka, H. Kempa, P. Esquinazi. *Phys. Rev. Lett.* 90, 156402 (2003); Y. Kopelevich, J.C. Medina Pantoja, R.R. da Silva, F. Mrowka, and P. Esquinazi. *Physics Lett. A* 355, 233 (2006).
- [5] S. Xu, J. Cao, C.C. Miller, D.A. Mantell, R.J.D. Miller, and Y. Gao. *Phys. Rev. Lett.* 76, 483 (1996).
- [6] H. Kempa, Y. Kopelevich, F. Mrowka, A. Setzer, J.H.S. Torres, R. Hohne, and P. Esquinazi. *Solid State Commun.* 115, 539 (2000); Y. Kopelevich, P. Esquinazi, J.H.S. Torres, and S. Moehlecke. *J. Low Temp. Phys.* 119, 691 (2000); R. Ricardo da Silva, J.H.S. Torres, and Y. Kopelevich. *Phys.Rev. Lett.* 87, 147001 (2001).
- [7] J. Gonzalez, F. Guinea, and M.A.H. Vozmediano. *Nucl. Phys. B* 406, 771 (1993); *ibid.*, *Nucl. Phys. B* 424, 595 (1994); *ibid.*, *Phys. Rev. Lett.* 77, 3589 (1996);
- [8] J. Gonzalez, F. Guinea, and M.A.H. Vozmediano. *Phys. Rev. B* 59, 2474 (R) (1999).
- [9] K.S. Novoselov, A.K. Geim, S.V. Morozov, D. Jiang, Y. Zhang, S.V. Dubonos, I.V. Gregorieva, and A.A. Firsov. *Science* 306, 666 (2004).
- [10] K.S. Novoselov, A.K. Geim, S.V. Morozov, D. Jiang, M.I. Katsnelson, I.V. Grigorieva, S.V. Dubonos, and A.A. Firsov. *Nature* 438, 201 (2005).
- [11] G. Ingold and Y. V. Nazarov, H. Grabert, and M.H. Devoret. *In Single Charge Tunnelling*, eds. Plenum Press, New York (1992).

4. The role of H-adsorbed atoms on graphite: zero bias anomaly in the density of electron states

- [12] X.G. Wen. *Phys. Rev. B* 42, 6623 (1990).
- [13] C.L. Kane and M.P.A. Fisher, *Phys. Rev. Lett.* 68, 1220 (1992). *ibid.* *Phys. Rev. B* 46, 15233 (1992).
- [14] F. Guinea and G. Zimanyi. *Phys. Rev. B* 47, 501 (1993); J.M.P. Carmelo, P.D. Sacramento, and F. Guinea. *Phys. Rev. B* 55, 7565 (1997); A.H. Castro Neto and F. Guinea, *Phys. Rev. Lett.* 80, 4040 (1998).
- [15] M. Sassetti, F. Napoli, and U. Weiss. *Phys. Rev. B* 52, 11213 (1995).
- [16] J. Rollbuhler and H. Grabert. *Phys. Rev. Lett.* 87, 126804 (2001).
- [17] S.V. Kravchenko, D. Simonian, M.P. Sarachik, W. Mason, and J.E. Furneaux. *Phys. Rev. Lett.* 77, 4938 (1996).
- [18] B.L. Altshuler, A.G. Aronov, M.E. Gershenson, and Y. V. Sharvin. *Sov. Sci. Rev. A* 9, 223 (1987).
- [19] Y. Imry and Z. Ovadyahu. *Phys. Rev. Lett.* 49, 841 (1982).
- [20] M.E. Gershenson, V.N. Gubankov, and M.I. Falei. *Zh. Eksp. Teor. Fiz.* 41, 435 (1985). *ibid.*, *JETP Lett.* 41, 535 (1985).
- [21] A.E. White, R.C. Dynes, and J. P. Garno. *Phys. Rev. B* 31, 1174 (1985).
- [22] A.L. Efros and B.I. Shklovskii. *J. Phys. C* 8, L49 (1975).
- [23] B.I. Shklovskii and A.L. Efros. *Electronic Properties of Doped Semiconductors*, Springer, New York (1984).
- [24] J.G. Massey and M. Lee. *Phys. Rev. Lett.* 75, 4266 (1995).
- [25] J.G. Massey and M. Lee. *Phys. Rev. Lett.* 77, 3399 (1996).
- [26] V.Y. Butko, J.F. DiTusa, P.W. Adams. *Phys.Rev. Lett.* 84, 1543 (2000).
- [27] www.ntmdt-tips.com/catalog/hopg.html
- [28] D. Martinez-Martin and J. Gomez-Herrero, arXiv:0708.2994v2.
- [29] P. Esquinazi, D. Spemann, R. Hohne, A. Setzer, K.H. Han, and T. Butz. *Phys. Rev. Lett.* 91, 227201 (2003).
- [30] D. Tomanek and S.G. Louie. *Phys. Rev. B* 37, 8327 (1988).
- [31] L. Hornakær, E. Rauls, W. Xu, Ž. Šljivančanin, R. Otero, I. Stensgaard, E. Lægsgaard, B. Hammer, and F. Besenbacher. *Phys. Rev. Lett.* 97, 186102 (2006).

-
- [32] L. Hornekær, Ž. Šljivančanin, W. Xu, R. Otero, E. Rauls, I. Stensgaard, E. Lægsgaard, B. Hammer, and F. Besenbacher. *Phys. Rev. Lett.* 96, 156104 (2006).
- [33] X. Sha and B. Jackson. *Surf. Sci.* 496, 318 (2002).
- [34] Y. Kobayashi, K-I. Fukui, T. Enoki, and Y. Kaburagi. *Phys. Rev. B* 71, 193406 (2005).
- [35] private communication Ž. Šljivančanin, 2007.
- [36] N. Ooi, A. Rairkar, and J. B. Adams. *Carbon* 44, 231, (2006).
- [37] L. Vitali, M.A. Schneider, and K. Kern. *Phys. Rev. B* 69, 121414(R) (2004).
- [38] E.T. Jensen, R.E. Palmer, and W. Allison. *Phys. Rev. Lett.* 66, 492 (1991).
- [39] D.W. Boukhvalov, M.I. Katsnelson, and A.I. Lichtenstein. *Phys. Rev. B* 78, 085413 (2008).
- [40] Y. Ferro, F. Marinelli, and A. Allouche. *J. Chem. Phys.* 116, 8124 (2002).
- [41] M.S. Dresselhaus and G. Dresselhaus. *Adv. Phys.* 30, 139 (1981).
- [42] B.T. Kelly. *Physics of Graphite*, Applied Science Publishers LTD (1981).
- [43] S.J. Williamson, S. Foner, and M.S. Dresselhaus. *Phys. Rev.* 140, A1429 (1965).
- [44] M.P. Sharma, L.G. Johnson, and J.W. McClure. *Phys. Rev. B* 9, 2467 (1974).
- [45] U. Fano. *Nuovo Cimento* 12, 156 (1935).
- [46] G. Breit and E. Wigner. *Phys. Rev* 49, 519 (1936).
- [47] J.M. Blatt and V.F. Weisskopf. *Theoretical Nuclear Physics*, John Wiley & Sons Inc. New York, pp. 379 and pp. 401, (1952).
- [48] H. Feshbach. *Ann. Phys. N.Y.* 5, 357 (1958).
- [49] H.B. Heersche, Z. de Groot, J.A. Folk, L.P. Kouwenhoven, and H.S.J. van der Zant. *Phys. Rev. Lett.* 96, 017205 (2006).
- [50] P. Wahl, L. Diekhoner, G. Wittich, M.A. Schneider and K. Kern. *Phys. Rev. Lett.* 95, 166601 (2005).
- [51] M.A. Schneider, L. Vitali, P. Wahl, N. Knorr, L. Diekhoner, G. Wittich, M. Vogelgesang, and K. Kern. *Appl. Phys. A* 80, 937 (2005).

4. The role of H-adsorbed atoms on graphite: zero bias anomaly in the density of electron states

- [52] A. Gruneis, C. Attaccalite, T. Pichler, V. Zabolotnyy, H. Shiozawa, S.L. Molodtsov, D. Inosov, A. Koitzsch, M. Knupfer, J. Schiessling, R. Follath, R. Weber, P. Rudolf, L. Wirtz, and A. Rubio. *Phys. Rev. Lett.* 100, 037601 (2008).
- [53] T.D. Stanescu, V. Galitski, and H.D. Drew. *Phys. Rev. Lett.* 101, 066405 (2008).
- [54] P. Phillips, T.-P. Choy, and R.G. Leigh. *Rep. Prog. Phys.* 72, 036501 (2009).
- [55] I.L. Spain, A.R. Ubbelohde, and D.A. Young. *Phil. Trans. Roy. Soc. (London)* A262, 345 (1967).
- [56] N. Garcia, P. Esquinazi, J. Barzola-Quiquia, B. Ming, and D. Spoddig. *Phys. Rev. B* 78, 035413 (2008).
- [57] D.C. Elias, R.R. Nair, T.M.G. Mohiuddin, S.V. Morozov, P. Blake, M.P. Halsall, A.C. Ferrari, D.W. Boukhvalov, M.I. Katsnelson, A.G. Heim, and K.S. Novoselov. *Science* 323, 610 (2009).
- [58] S. Cho, Y. Kim, A.J. Freeman, G.K.L. Wong, J.B. Ketterson, L.J. Olafsen, I. Vurgaftman, J.R. Meyer, and C.A. Hoffman. *Appl. Phys. Lett.* 79, 3651 (2001).
- [59] P.B. Visscher and L.M. Falicov. *Phys. Rev. B* 3, 2541 (1971); A.L. Fetter. *Ann. Phys* (NY) 88, 1 (1974); S. Das Sarma and J.J. Quinn. *Ann. Phys.* (NY) 25, 7603 (1982); A.C. Tselis and J.J. Quinn. *Ann. Phys.* (NY) 29, 3318 (1984); J.K. Kain and P.B. Allen. *Phys. Rev. Lett.* 51, 919 (1985); J.-W. Wu and J.J. Quinn. *Phys. Rev. B* 32, 4272 (1985).
- [60] D. Grecu. *Phys. Rev. B* 8, 1958 (1973).
- [61] V.Z. Kresin and H. Morawitz. *J. Opt. Soc. Am. B* 6, 490 (1989).
- [62] F. Stern. *Phys. Rev. Lett.* 18, 546 (1967).
- [63] T.O. Wehling, S. Yuan, A.I. Lichtenstein, A.K. Geim, and M.I. Katsnelson. *Phys. Rev. Lett.* 105, 056802 (2010).
- [64] R. Tediosi, N.P. Armitage, E. Giannini, and D. van der Marel. *Phys. Rev. Lett.* 99, 016406 (2007).
- [65] S. Yuan, S. De Raedt, and M.I. Katsnelson. *Phys. Rev. B* 82, 115448 (2010).
- [66] K. Sugawara, T. Sato, S. Souma, T. Takahashi, and H. Suematsu. *Phys. Rev. Lett.* 98, 036801 (2007).
- [67] S. Yuan, S. De Raedt, and M.I. Katsnelson. *Phys. Rev. B* 82, 235409 (2010).

- [68] private communication with M.I. Katsnelson, Dec. 2010.
- [69] P. Ruffieux, M. Melle-Franco, O. Groning, M. Bielman, F. Zerbetto, and P. Groning. *Phys. Rev. B* 71, 153403 (2005).
- [70] M. Lee, J.G. Massey, V.L. Nguyen, and B.I. Shklovskii. *Phys. Rev. B* 60, 1582 (1999).
- [71] A.V. Shytov, M.I. Katsnelson, and L.S. Levitov. *Phys. Rev. Lett.* 99, 236801 (2007).
- [72] A.V. Shytov, M.I. Katsnelson, and L.S. Levitov. *Phys. Rev. Lett.* 99, 246802 (2007).

Chapter 5

Tailoring the electronic structure properties of single walled carbon nanotubes by H chemisorption

5.1 Introduction

Nowadays, carbon based materials, namely graphene, fullerenes and carbon nanotubes attract the scientific community due to their intrinsic electronic structure properties, for both applied and fundamental research [1–4]. Particularly interesting, carbon nanotubes present a wide variety of electronic structure properties making them interesting for future development of carbon nanotube based electronics [5]. The single walled carbon nanotubes are the most interesting since they have a more elegant and simpler geometrical structure and more importantly, they are easier to model from a theoretical point of view, thus making it possible to achieve a good resemblance between experimental and theoretical works.

In this chapter, the effects of hydrogen chemisorption on single-walled carbon nanotubes (SWCNT) will be explored mainly from two points of view: topological changes induced in the nanotubes and local modifications of the electronic structure properties of the nanotubes. In Chapter 2 the electronic structure properties of metallic and semiconducting carbon nanotubes were introduced. In addition, the effects of dopants (for e.g. adsorbed foreign chemical species, structural defects) on the local density of states of carbon nanotubes were briefly discussed. This chapter summarizes results obtained in studying the effects of hydrogen chemisorption on single-walled carbon nanotubes. Topics covered range from choosing a suitable substrate for tube deposi-

5. Tailoring the electronic structure properties of single walled carbon nanotubes by H chemisorption

tion, to the determination of carbon nanotube chirality, to hydrogen treatment of the tubes and investigation of the electronic structure properties of hydrogen treated and non-treated SWCNTs. We present local changes in the electronic structure properties for hydrogen treated metallic and semiconducting SWCNT, determined with STS at low temperature. Understanding how the electronic structure properties of carbon nanotubes can be altered at a nano-scale can be important for the future carbon based electronics.

5.2 Sample preparation procedure

5.2.1 Gold substrate preparation

STM experiments require a conductive, clean and flat substrate. If the sample preparation is done in ambient conditions, the substrate must not be reactive to the environmental gasses (e.g. oxidation). A commonly used surface for STM experiments is a gold (111) film on mica or glass substrates. Gold is thermally evaporated onto a substrate and it can be made atomically flat either in ambient conditions (flame-annealing) or by repeated cycles of sputtering and annealing under UHV conditions. The gold substrates were supplied by Arrandee and the flame-annealing procedure was suggested by the manufacturer [6]. The substrate material of these samples consists of a borosilicate glass slide (1.1 mm). On this glass substrate, a thin – 1 up to 4 nm - chromium layer is deposited for an optimal adhesion of the gold layer to the glass. The thickness of the gold layer is reported by the manufacturer to be between 200 and 300 nm.

Flame-annealing was used to create atomically flat Au (111) terraces. The substrate was heated in a propane or butane flame until the surface has a dark red glow. Afterwards, the substrate was allowed to cool for approximately 30 s. Repeating this procedure two or three times provided flat gold (111) terraces of about 100 nm in diameter, separated by rough grain boundaries [6]. STM images of the flame-annealed Au (111) reveal atomically flat terraces, as depicted in Figure 5.1. The size of the terraces is sufficient for deposition and investigation of carbon nanotubes.

Another conductive substrate that was used in this work is HOPG. The preparation procedure of this substrate is very fast and easy (cleaving with scotch tape) but the major drawback is the weak interaction between the HOPG and the nanotubes. The binding energy of SWCNT on HOPG is similar to the interaction between two graphite planes, thus it is weak, van der Waals in origin [7]. An interaction energy of 1.6 eV per nanometer tube length was calculated for tube diameters in the order of 1.5 nm [8]. The interaction between nanotubes and gold is shown to be in the order of 8 eV per nanometer [9]. Due to the weak bonding between nanotubes and HOPG,

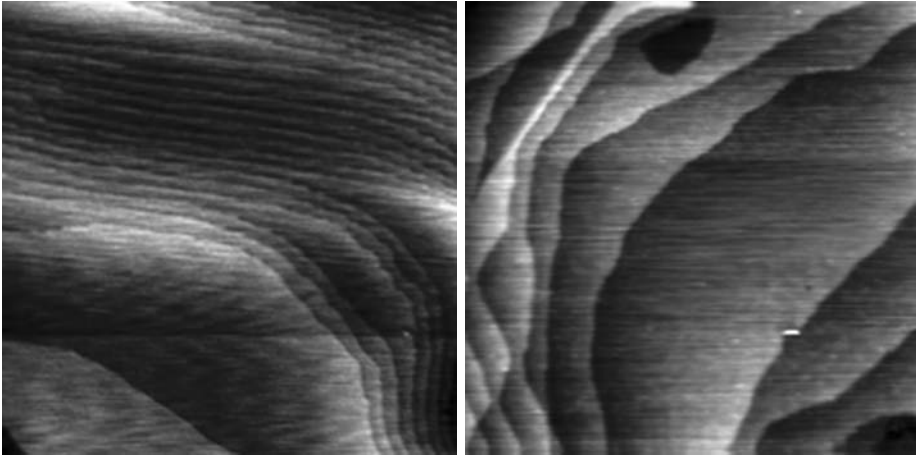


Figure 5.1: Topographic STM images of Au (111) terraces on flame annealed gold-on-glass substrates, where the atomic steps separating terraces are clearly visible. The scanning parameters are: $V_{gap}=0.82$ V, $I_t=0.1$ nA, scan size is 200×200 nm².

during STM experiments the nanotubes are quite mobile, thus unstable experimental conditions are very often encountered. For this reason, all the STM work reported in this thesis on SWCNT will be on a gold covered substrate.

5.2.2 Nanotube dispersion

Carbon nanotubes are usually supplied in freeze-dried powder form. The nanotube samples used in this study are arc discharge and were supplied by Y. X. Liang and Professor Z. J. Shi ¹ or are commercial CVD nanotube material from South West Nanotechnologies Inc. [13]. To investigate the SWCNT by STM and STS, one must be able to isolate individual nanotubes and place them on a suitable surface. This can be achieved by dissolving the nanotube powder in 1,2-di-chloroethene ($C_2H_2Cl_2$, DCE) while assisted by ultrasound. A small amount of the dry nanotubes material (0.5 mg) was put in a small glass bottle using a clean glass pipette. Afterwards, the glass bottle is filled with approximately 1 ml of DCE and is sonicated for 2 h. After the sonication procedure, larger agglomerates of nanotubes will be sticking on the glass or will be lying at the bottom of the bottle. However, the smaller aggregates will be dispensed in. By taking out a small amount of this more homogenous part of the dispersion, light gray in color, and mix it again with new DCE solution, a better mixture of CNT and DCE is produced. After one more hour of sonication the

¹Department of Chemistry, Peking University, Beijing 100871, Peoples Republic of China

5. Tailoring the electronic structure properties of single walled carbon nanotubes by H chemisorption

solution was of a uniform light gray color, thus lacking black large conglomerates. This nanotube dispersion was applied on the SPM substrate by applying a drop on the surface using a pipette under ambient conditions. The DCE evaporates in air, while the nanotubes stick to the surface. Upon drop-casting, the coffee-stain effect is visible on the substrate, meaning that a larger concentration of nanotube material is present towards the edge of the drop. To prevent this effect, two procedures were used: either tilting the substrate under an angle or gently blowing dry N_2 during the solvent evaporation [10]. Another method of CNT deposition is spin-coating. However, this method appeared not to be very efficient and the procedure was abandoned in an early stage. Due to the differences in the sample preparation, the exact preparation parameters will be specified for each sample that will be discussed in this thesis.

5.2.3 Hydrogen deposition

One impediment in ionic induced defect studies on CNTs is the determination of the exact nature of the defect [10, 11]. As an example, a hydrogen ion with a kinetic energy of 1 eV can create a single vacancy or a carbon-hydrogen complex or a chemisorbed hydrogen atom structure on the nanotube. The RF ion source (Oxford Applied Research Atom/Radical Beam source [12]) utilized for hydrogen decoration of SWCNT is provided with a porous quartz glass that is thermalizing the hydrogen ions. The thermal hydrogen ions can only bind to the CNT by chemisorption since their kinetic energy is low, tens or hundreds of meV. The RF power input in the plasma is about 350 W, the RF excitation is 13.56 MHz. The same ion source is used for the H deposition on HOPG, discussed in Chapter 4. The Au substrate is inert to the hydrogen treatment. Any other surface contaminants will react with the H ions, which in turn can be beneficial as it creates an inert environment for the CNTs. The exposure time of the CNT to the H ions was the only variable during H deposition. The exposure time was chosen as a first guess by the experience gained in the work summarized in Chapter 4. Quantitatively, an exposure time of HOPG to H of about 10 s created roughly 10 structures on a $50 \times 50 \text{ nm}^2$ area.

5.3 Experimental results and discussion

5.3.1 Determining the chiral indexes of arc-discharge carbon nanotubes

To test how well dispersed the CNTs have been dispersed in the solvent, the nanotubes were first deposited on HOPG and studied with AFM. One resulting topography is depicted in Figure 5.2. In this case, the nanotube solution was sonicated for 16 h. The AFM results indicate that the surface has a quite good density of CNT but mostly

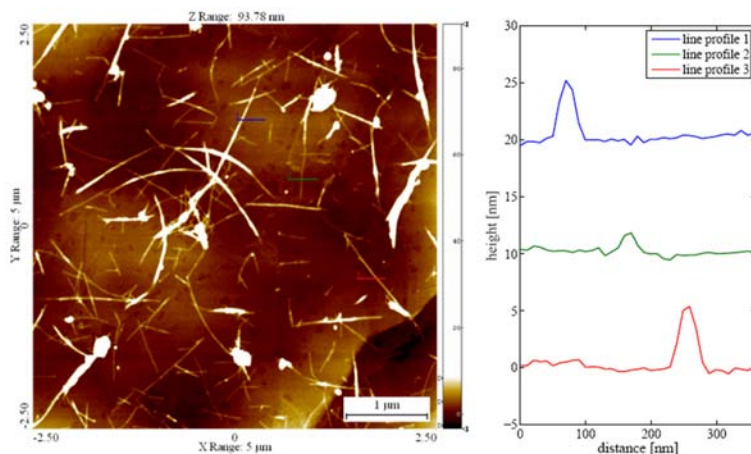


Figure 5.2: Topographic AFM image of arc discharge nanotube bundles on HOPG. The image size is $5 \times 5 \mu\text{m}^2$, height of the bundles vary between 2 and 5 nm, as it can be seen in the cross-section line profile from the right hand side. Contamination particles (brightest features) measure up to 80 nm in height.

the CNT are present in bundles. This solution was also used to prepare samples for STM.

For STM experiments, a gold substrate was prepared by flame annealing procedure and a drop of the nanotubes in DCE was placed on the surface. After the solvent was evaporated, the sample was loaded in the UHV setup and annealed for about 15 min. at 120°C . The STS experiments were conducted at 77 K. As expected from the AFM results shown above, CNT in bundles are observable also with STM, as in Figure 5.3.

To check the chirality of a nanotube, the chiral angle should be measured in the STM image. Due to tip convolution in the STM imaging, the tubes are stretched in the direction perpendicular to the tube-axis. Due to this effect, the chiral angle in a STM image differs from the actual chiral angle. In order to compensate for the above mentioned effect, the solution is to shrink the image in the direction perpendicular to the tube axis [14, 15]. Making use of procedure, it is possible to fit the angles of the tube-pattern. Furthermore, when the angles are correct, the chiral angle measured in the shrunken image will resemble the chiral angle of the nanotube.

For the chiral angle determination, one image with available STS data was selected for analysis. From all the available bundles we will focus on only two nanotubes. Next, we will determine the chirality of those two nanotubes. For tube 1 (the left tube in Figure 5.4a and b) the angle was measured to be $\simeq 7^\circ$, while the chiral angle of tube 2 is $\simeq 9^\circ$. The Figure 5.4c and d are the cutouts from Figure 5.4a and b and were

5. Tailoring the electronic structure properties of single walled carbon nanotubes by H chemisorption

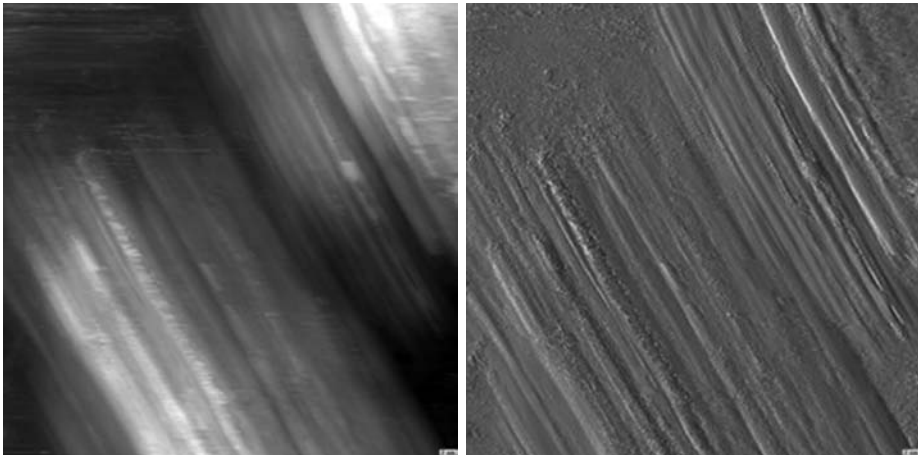


Figure 5.3: Topographic (left) and current (right) STM image of a nanotube bundle on gold. Both images show a clear view of the orientation of the tubes in the bundle as well as an indication for a pattern on the nanotubes formed by the individual carbon atoms. The scanning parameters are: $U_{gap}=100$ mV, $I_t=0.5$ nA, scan size: 50×50 nm².

shrunk in the horizontal direction in order to get the angles of the triangles correct, thus making it possible to measure the chiral angles from these STM images.

To determine the (m, n) indices of a nanotube, the chiral angle and the tube diameter have to be known. Determining the tube diameter is challenging especially when the tube is in a bundle. Due to tip-tube interaction the width of the tube appears somewhat larger. A rough estimation of the width of the tubes, from Figure 5.4, is 1.2 nm. However another approach might provide a better determination of the (n, m) . If the chiral angle is known, then one can look up which tubes have a chiral angle close to the measured angle. This, in combination with a certain range in diameter, will provide a selection of possible tubes.

For angles between 5.8° and 10.2° and a diameter between 0.5 nm and 2 nm, there are 27 possible nanotubes [16]. In order to precisely determine the chiral indexes of the nanotubes extra information can be gathered by STS experiments. These provide information about the metallic or insulating behavior of the carbon nanotubes.

The spectroscopy points are depicted in Figure 5.4 a as dots. Both nanotubes show van Hove singularity (VHS) peaks or onsets relatively close to the Fermi level with a separation of $\simeq 0.69$ eV for tube 1 and $\simeq 0.61$ eV for tube 2. Unless the conductance in between the peaks was not entirely zero, then both tubes are semiconducting. If

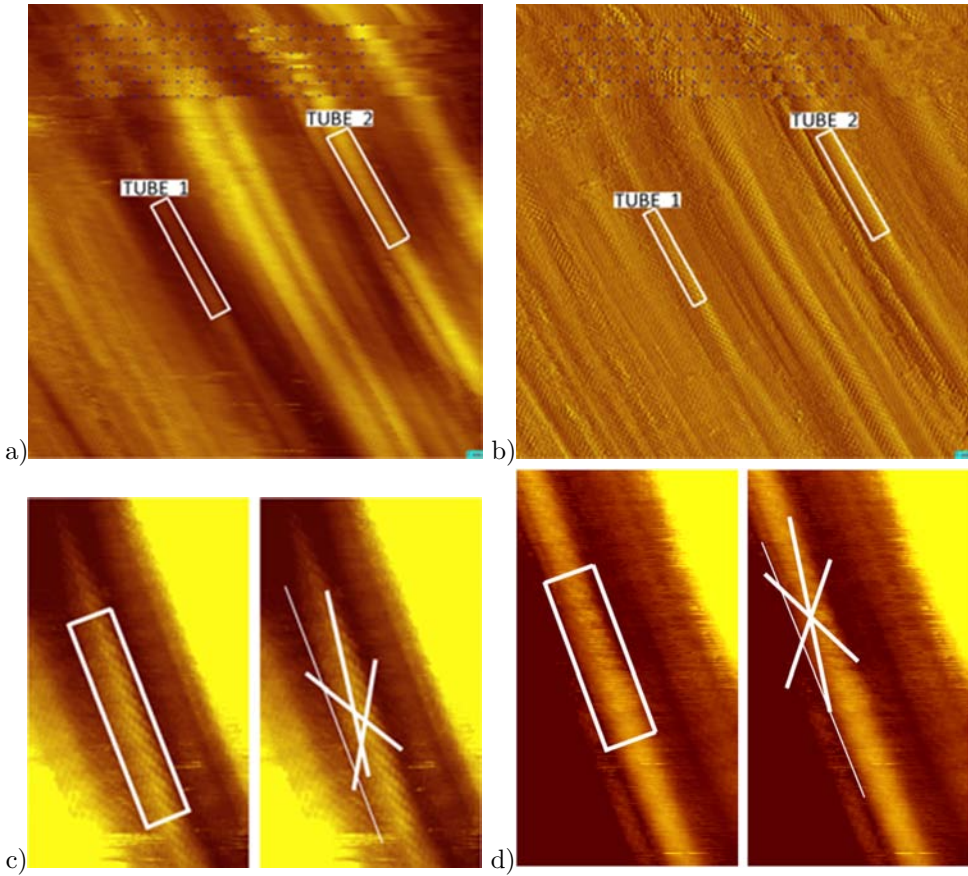


Figure 5.4: Topographic (a) and current (b) of a nanotube bundle on gold. Scanning parameters are: $U_{gap}=102$ mV, $I_t=488$ pA, scan size 30×30 nm². The blue dots in the upper part of (a) are spectroscopy grid-points. Images (c) and (d) are cutouts of the topographic image and shrunk in horizontal direction to match the 60° angle in the hexagonal carbon lattice, enabling a more accurate measurement of the chiral angle. Chiral angles are measured to be $\simeq 7^\circ$ and 9° for tube 1 and respectively 2.

5. Tailoring the electronic structure properties of single walled carbon nanotubes by H chemisorption

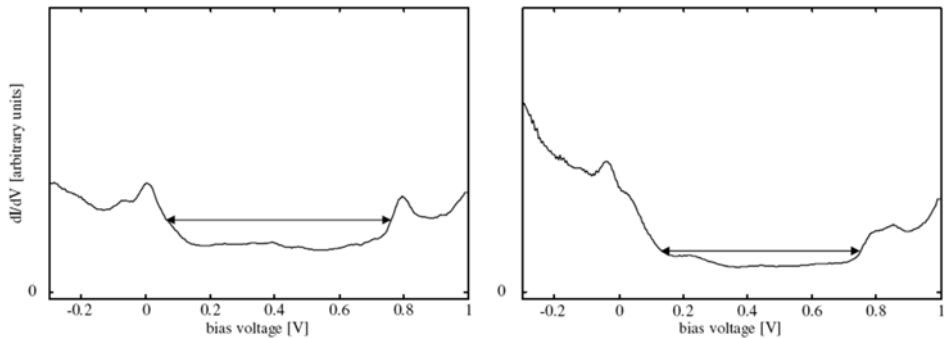


Figure 5.5: Tunneling conductance data, dI/dV , for tube 1 (left panel) and tube 2 (right panel). The data was recorded as the in-phase component of I directly by a lock-in amplifier with a 1.3 kHz modulation signal of 8 mV peak-to-peak amplitude to the bias voltage, at $T=77$ K. The gap widths are measured to be $\simeq 0.69$ eV and $\simeq 0.61$ eV for tube 1 and 2, respectively.

the tubes would be metallic² then the separation between the peaks would be around 2 eV. Table 6.1 provides information regarding the semiconducting nanotubes in a diameter range from 0.5 to 2 nm and a chiral angle in a range from 5.8° to 10.2° .

Thus, for tube 1 (7° , 0.5-2 nm, 0.69 eV) the best match is made with a tube that has a chiral indices (12,2) that has a chiral angle of 7.59° , a diameter of 1.03 nm and an energy gap of 0.68 eV. For tube 2 (9° , 0.5-2 nm, 0.61 eV) the (14,3) tube with a chiral angle of 9.52° , a diameter of 1.23 nm and an energy gap of 0.59 is the best candidate.

5.3.2 Chemisorbed hydrogen on metallic CNT

Topological effects. CNT identification

The available arc-discharge produced carbon nanotube material was limited and most of the CNT were in bundles. To continue this study differently produced SWCNTs were ordered. The following results from this chapter are obtained on CoMoCat SWCNTs, from SWENT [13]. Due to the growth method (CoMoCat [37–39]), the nanotubes are less entangled than the arc discharge grown nanotubes. The dispersion method was adjusted to compensate for the above-mentioned fact. A small amount ($\simeq 0.5$ mg) of dry material was dispersed in DCE and sonicated for approximately 2 h. Afterwards, the mixture of DCE and SWCNT was left to settle for half an hour and then a small amount of this dispersion was taken out using a glass

²For a metallic (12,3) nanotube - with a diameter of 1.15 nm - the separation between the first VHS peaks is 2.0 eV.

Table 5.1: Semiconducting nanotubes with diameters ranging from 0.5 to 2 nm and a chiral angle ranging from 5.8 to 10.2°

(n, m)	chiral angle	diameter (nm)	E_{gap}
(8,1)	5.82	0.67	1.02
(16,2)	5.82	1.34	0.54
(15,2)	6.18	1.26	0.55
(22,3)	6.31	1.85	0.38
(20,3)	6.89	1.70	0.42
(13,2)	7.05	1.11	0.65
(19,3)	7.22	1.62	0.43
(6,1)	7.59	0.51	1.43
(12,2)	7.59	1.03	0.68
(17,3)	7.99	1.46	0.49
(16,3)	8.44	1.39	0.50
(21,4)	8.57	1.82	0.39
(10,2)	8.95	0.87	0.83
(20,4)	8.95	1.74	0.40
(14,3)	9.52	1.23	0.59
(9,2)	9.83	0.80	0.87
(18,4)	9.83	1.59	0.45
(22,5)	10.02	1.95	0.37
(13,3)	10.16	1.15	0.60

5. Tailoring the electronic structure properties of single walled carbon nanotubes by H chemisorption

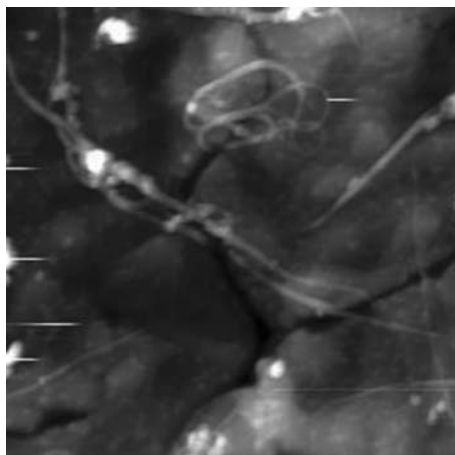


Figure 5.6: Topographic AFM image of CoMoCat carbon nanotubes on a flame-annealed gold substrate. Image size is $1 \times 1 \mu\text{m}^2$. The image shows both individual tubes and bundles.

pipette and put in a new, clean glass bottle. Another the sonication procedure was performed afterwards, for 1 h, while some extra DCE solvent was added. A few drops of dispersion were placed on a flamed-annealed gold substrate and investigated by AFM to check if the nanotubes are well dispersed on the substrate. Figure 5.6 shows that the preparation method results in reasonably well dispersed CNT s. It is estimated that this preparation procedure yields a bundle to individual SWCNT ratio of about 8:1. A similarly prepared sample was investigated by STM with a freshly mechanically cut PtIr tip. Nanotubes are present on most of the regions of the gold substrate. From now on the main focus will be on isolated CNT. Figure 5.7 shows a large and a small scan area with CNT. Furthermore the nanotubes present a smooth surface, consistent with a lack of structural defects. These nanotubes are good candidates for hydrogen deposition.

The creation of H patches on CNT offers an interesting possibility to study the role of chemisorbed foreign atomic species on the modification of CNT LDOS. The information on the changes of the LDOS of CNT upon H chemisorption will be provided by STS experiments. Similarly to the deposition method of H on HOPG (see Chapter 4), Au substrates with CNT deposited on top are exposed to hydrogen. STM measurements can provide information regarding the density of hydrogen structures on CNT for a certain exposure time to the RF source. Two identical samples were prepared and exposed to hydrogen for 10 s and respectively 20 s. Comparing the topographic results from Figure 5.8 and Figure 5.7, it is clear that due to the exposure

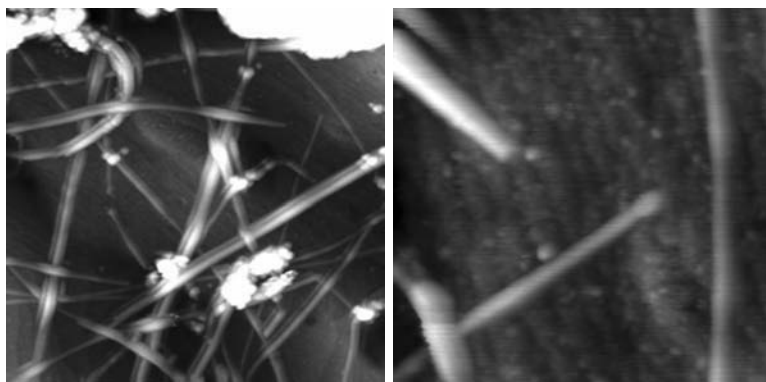


Figure 5.7: Topographic STM images of CoMoCat nanotubes on gold. Scanning parameters: $U_{gap}=1.1$ V, $I_t=0.15$ nA, image size - 200×200 nm² (left) and 50×50 nm² (right image). The left STM image shows a multitude of individual nanotubes, while the right hand-side image shows sections of CNT being smooth and defect-free.

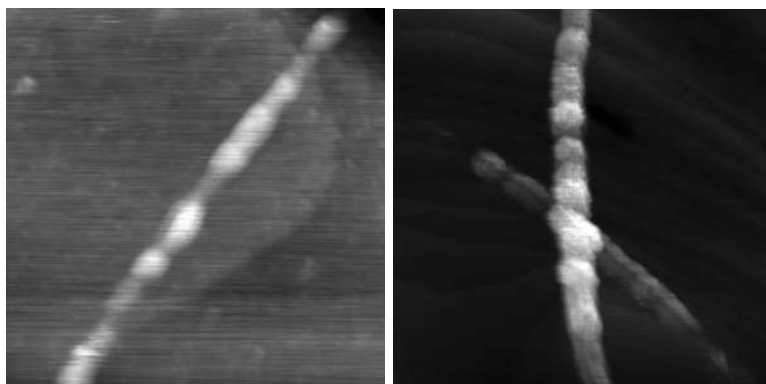


Figure 5.8: Topographic STM images of plasma treated CNT for 10 s (left-hand side image) and 20 s (right-hand side). On both images hillock like features can be observed that were not present on CNT before H treatment. The density of the H-induced features is larger for the sample with 20 s exposure time to the atomizing source. Scan sizes: 50×50 nm² (left image) and 80×80 nm² (right image).

5. Tailoring the electronic structure properties of single walled carbon nanotubes by H chemisorption

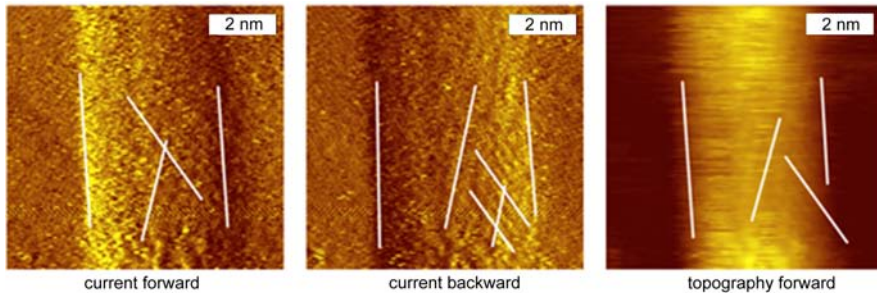


Figure 5.9: A pattern corresponding to the carbon atoms is visible in all three images, making it possible to determine the chiral angle as being $7.2 \pm 0.9^\circ$. Scanning parameters: $U_{gap}=0.9$ V, $I_t=0.1$ nA.

to H the topography of the CNT is changed. The hillock like features are similar to the topographical features observed when HOPG is treated with H, i.e. Figure 4.2. More compelling evidence that the H is adsorbed on the CNT is brought by the fact that all the tubes present on the surface show the presence of this hillock like features. Increasing the exposure time (from 10 s to 20 s) results in an increase of the features density and size, clearly observable from Figure 5.8.

First, we shall study the case when CNT are exposed to a short time to hydrogen atoms. For this purpose, a sample was exposed for 2 s to the atomic H environment. This sample was studied with STM and STS at both 77 and 5 K. A nanotube with a small H patch was identified as being metallic, as follows. First, the chiral index of the nanotube was determined by the method described in the previous section. By averaging 10 cross-sections of the topography scan over the tube depicted in Figure 5.9 the diameter is measured to be 1.12 ± 0.18 nm. The chiral angle is measured in the upper part of the nanotube and it is determined to be $\simeq 7.2 \pm 0.9^\circ$, as depicted in Figure 5.9. The chiral angle measured from these images is multiplied by a factor to correct for the deviation from the 60-degree angle [15] between the crossing lines from Figure 5.9.

Combining the above mentioned information regarding the nanotube (metallic, 1.12 nm in diameter and a chiral angle of $7.2 \pm 0.9^\circ$), a few options for the chirality index of the tube is presented in Table 5.2. The table provides a selection of metallic nanotubes with diameters in the range from 0.7 to 1.4 nm and chiral angles from 4.5 to 11° from a complete nanotube table presented elsewhere [16]. As it can be observed, the best candidate is the nanotube with the chiral index (14,2).

Table 5.2: Metallic nanotubes with diameters ranging from 0.8 to 1.5 nm and a chiral angle ranging from 4 to 11°

(n, m)	chiral angle	diameter (nm)	E_{gap}
(10,1)	4.72	0.83	0
(17,2)	5.50	1.42	0
(14,2)	6.59	1.18	0
(11,2)	8.21	0.95	0
(15,3)	8.95	1.31	0
(12,3)	10.89	1.08	0

5.3.3 Zero bias anomaly and Fano interference in hydrogen treated metallic SWCNT

On this tube, a hillock-like feature was identified, Figure 5.10. The apparent height of the hillock feature is about 0.4 nm. This value is very close to the apparent height of the hydrogen hillock features measured on HOPG, as reported in Chapter 4. Mediating over seven STS spectra acquired around the hydrogen patch, in the LDOS a dip feature around the Fermi level (Figure 5.10b) is observable at 77 K. To understand the origin of the dip feature, a position resolved STS experiment was conducted.

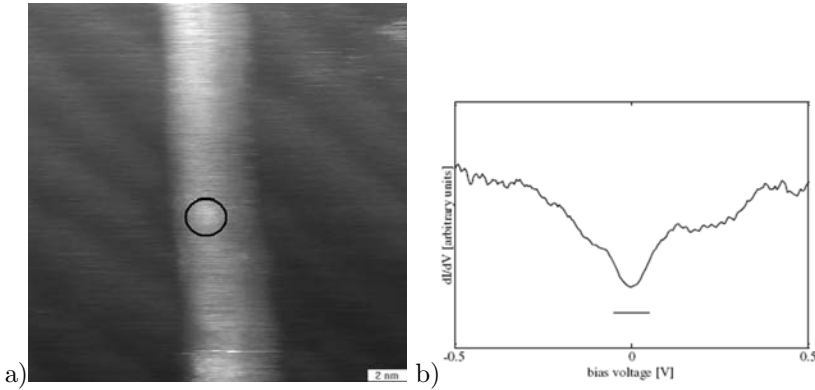


Figure 5.10: a) Topographic STM image ($20 \times 20 \text{ nm}^2$) of a chiral metallic nanotube section with a hydrogen feature (bright spot with an apparent height of 0.4 nm) measured at 77 K. $U_{gap}=495 \text{ mV}$, $I_t=0.97 \text{ nA}$. b) Tunneling conductance data, dI/dV , measured with the lock-in technique (1.3 kHz modulation signal and 12 mV peak-to-peak amplitude) showing the metallic behavior with an unexpected but pronounced dip at the Fermi level. The short horizontal line indicates the 0 level in the dI/dV .

In the tunneling spectra depicted in Figure 5.11, two classes of spectra attract

5. Tailoring the electronic structure properties of single walled carbon nanotubes by H chemisorption

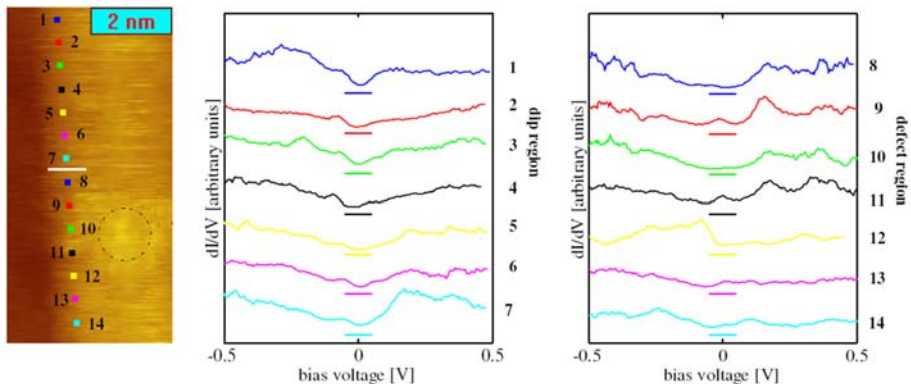


Figure 5.11: a) Topographic STM image with spectroscopy locations and the tunneling conductance spectra, dI/dV , recorded in these points. The scanning parameters are: $U_{gap}=495$ mV, $I_t=0.97$ nA, image size 2×9 nm². The hydrogen patch is located next to points 9, 10 and 11. Three different regions can be observed. In the top part of the tube (spectra 1-6) a dip is present at the fermi level, while two peaks are observable close to E_F and at $\simeq 150$ meV. In spectra 13 and 14 the DOS is flat and corresponds to the bulk DOS of the CNT.

interest. First, the spectra recorded in the upper part of the tube, namely spectra 1–6, show a suppression of the tunneling conductance at the Fermi level. Second, the spectra recorded close to the hydrogen patch, especially spectra 9–12 show two peaks, one at the Fermi level and one at about 150 meV. For the consistency of the data obtained, these results were reproduced during three subsequent measurements.

First we will discuss the presence of the dip present at the Fermi level. This dip -feature is unexpected since a chemisorbed H should introduce in the LDOS quasisubband or virtual electronic states and not an actual suppression of the electronic states at the Fermi level. Second, although on the sidewalls of the CNT, hydrogen might be chemisorbed, the effect of H patches on the LDOS of the metallic CNT appears to be for at least 4 nm of the CNT rather uniform. The width of the dip is $\simeq 185$ meV, measured from the edge to the edge of the dip. This dip feature does not imply a lack of conductance at the E_F . A more detailed view of this feature in the DOS can be observed in Figure 5.12. Simulated LDOS and experimental tunneling conductance spectroscopy results show small gaps (non-zero gaps) in metallic nanotubes at the Fermi level, assigned to a coupling effect with states of neighboring nanotubes [18–22] or substrate [21, 23]. Different from the gaps originating from these interactions between the individual SWNT and neighboring objects, Ouyang presented experimental proof for the existence of an intrinsic curvature induced gap in metallic carbon nanotubes [19].

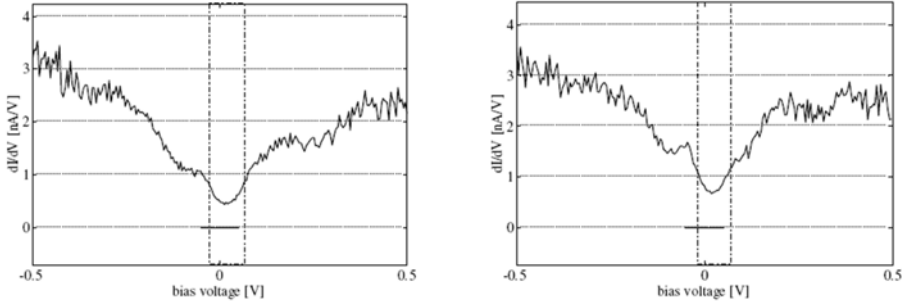


Figure 5.12: a) Two single tunneling conductance spectra, dI/dV , both recorded on the upper part of the metallic (14,2) nanotubes with the lock-in technique. The width of the dip is $\simeq 190$ meV in the left panel and $\simeq 180$ meV in the right panel.

Third, in a region located 1-2 nm away from chemisorbed hydrogen patches the spectroscopy data recorded on the metallic CNT (14,2) (see Figure 5.11), two peaks in the LDOS are noticed. One of them is located very close to the E_F and the second one is located at $\simeq 140$ mV. The spectroscopy locations are not on top of the H patch but at a distance of around 1.2 nm. These data were recorded at 77 K. Figure 5.13 presents the experimental data acquired.

On the possible physical origin of the zero bias anomaly and Fano interference state

Tube-tube interaction originated gaps were predicted in the work of Delaney [21]. The gap is induced by broken symmetry caused by tube-tube interactions (the inter-tube overlapping of the π orbitals and the van der Waals interactions). In theoretical calculations including the full interaction between the tubes, using both the ab initio pseudo-potential local-density-functional method and the empirical pseudo-potential method (EPM), gaps with a width of $\simeq 0.1$ eV and a non-zero minimum of about one third of the average of the DOS at E_F are observed [21]. Experimental results presented by Ouyang [19] showed the magnitude of the gaps ranging from 80 meV for (10,10) to 100 meV for (7,7) SWNT characterized by STM and STS. The gap magnitude of the studied CNT exhibited an inverse dependence on the tube radius. The shape, width and depth of the tube-tube pseudo-gap is similar to the zero bias anomaly measured on the (14,2) tube in our experiments. However, the similarities between them does not necessarily mean that the origin of the gaps is the same, since the hydrogen decorated nanotubes where the gap was measured are isolated and not in a bundle, like the gap observed by Ouyang [19].

Chemisorbed hydrogen on CNT s might modify the overlap of the π orbitals due

5. Tailoring the electronic structure properties of single walled carbon nanotubes by H chemisorption

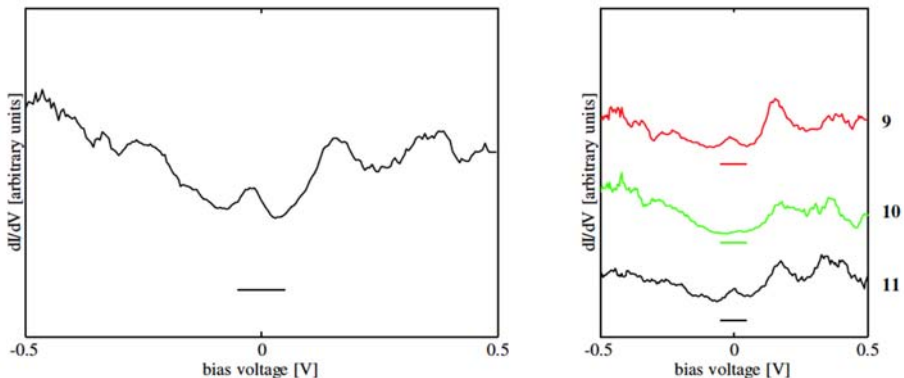


Figure 5.13: Tunneling conductance, dI/dV , depicting in the left panel the mean spectra of the spectra shown in the right panel (data in the right panel was subsequently shifted by an offset) The data shows a peak at around -20 meV and another peak at around 140 meV.

to curvature effects. Briefly, a finite curvature reduces the overlap of the nearest π orbitals by a factor of $\cos^2 \alpha$, where α is the angle between the two neighboring π orbitals as exemplified in Figure 5.14. This reduction in the orbital overlap shifts the Fermi wave-vector, k_F , from the first Brillouin zone corner (K -point) of the 2D graphene sheet. For a metallic zigzag nanotube, k_F moves away from the K -point along the circumferential direction such that the allowed one-dimensional sub-band no longer passes through the K -point, resulting in the opening of a small gap at the Fermi level. The simple model that explains the presence of such a gap concludes that the energy gaps of the metallic zigzag CNTs should scale with $1/R^2$, with R the tube radius. This result is consistent with analytical calculations for the Hamiltonian on a curved surface [24].

The widths of these gaps were extracted from the measured spectra and yielded averaged energies of 80 ± 5 , 42 ± 4 and 29 ± 4 meV for (9,0), (12,0), and (15,0) SWNTs, respectively. The measured gap magnitudes multiplied by a factor proportional to the squared diameter (3^2 , 4^2 and 5^2) equal 720, 672 and 725 for respectively the (9,0), (12,0), and (15,0) SWNTs, showing the inverse dependence on the squared tube radius. This implies that these gaps arise indeed from curvature in the graphene sheet [19]. Similar gap values were obtained by ab initio calculations, predicting gap widths of 93 meV for (9,0) and 28 meV for (15,0) SWNTs [17]. The gap value for the (12,0) nanotube was found to be 78 meV, deviating quite a lot from the experimental value of 185 meV.

The gap width is inversely proportional with the radius squared of the CNT. In

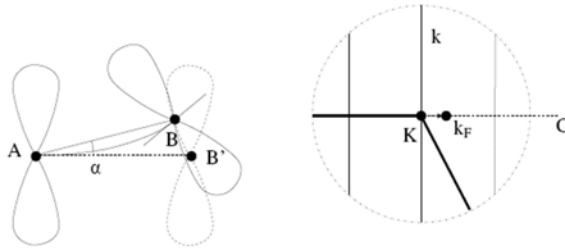


Figure 5.14: a) k_F shift for the curved CNT. In the left panel A and B represent the parallel π orbitals of the nearest-neighbor carbon atom on a flat graphene sheet, while B denotes the p orbital of a nearest-neighbor atom on a curved surface. The angle α is the angle between AB and AB and represents a measure of the local curvature. In the right panel, the bolded lines represent two slides of the hexagonal first Brillouin zone on a flat graphene sheet, the vertical lines are the allowed k -states which form the energy bands of a nanotube. C denotes the circumferential direction. In metallic zigzag SWCNTs k_F moves along the C direction away from the K point, resulting in the opening of a small gap in the DOS of the tube [19].

the case of a (14,2) tube, with the diameter close to the diameter of the (15,0) tube, this means that a curvature-induced gap would measure about 30 meV. Without discussing the presence of such a curvature induced gap [25,26], it is safe to state that the zero bias anomaly in the spectroscopic data recorded on the metallic (14,2) tube is not related to the curvature of the nanotube wall.

In the Ph.D. thesis of Venema [15], a gap feature was observed in some, but not all, tunneling spectra recorded on metallic nanotubes. The gap or suppression of the tunneling DOS, at the Fermi energy for disorder conductors is a well-known problem in literature [27]. It was found that electron-electron interactions in the presence of impurities result in a negative correction of the DOS, which is singular at the Fermi level. The explanation given by Venema et al. [28] treats the metallic nanotube as normal conductor, and the tip as the element bringing in the low energy feature by the disorder in the tip material. In the case of the nanotube with a hydrogen defect, the nanotube itself can be thought of as the disordered conductor. The electron - electron interactions in the presence of the hydrogen defect would possibly be the origin of the zero bias anomalies at the Fermi energy. In addition, the V-shaped gap found in tunneling conductance data for hydrogen decorated HOPG was recorded with different tips. In these experiments, both etched tungsten (W) tips and mechanically cut platinum iridium alloy (Pt 90%, Ir 10%) STM tips were used. The presence of the zero bias anomaly - not depending on the tip used in the experiment is an argument to reject the option that the dip is a negative correction of the DOS because of electron

5. Tailoring the electronic structure properties of single walled carbon nanotubes by H chemisorption

- electron interactions in the presence of impurities in the tip material itself.

A more pronounced peak at $\simeq -40$ meV was reported for the measurement on a (high-energy) hydrogen plasma treated metallic nanotube by Buchs [10]. The authors assign the presence of this peak to the presence of a vacancy that may or may not be saturated with a H atom. The dangling bond in this vacancy defect would be responsible for states near the Fermi level in a very small region (less than 1 nm away) surrounding the defect. Since we work with low energetic H ions or atoms, chemisorption of H should not induce the appearance of dangling bonds. Thus, although the peaks reported by others [10] are similar to ours, the nature of the causality determining the appearance of the peak close to the Fermi level is to our belief different. In addition Buchs compares his experimental results with an STS simulation based on the tight-binding Green's function technique for a tip positioned on a single vacancy in a metallic (10,10) SWCNT [36]. To our interpretation, both the shape and position of the peak observed in their experiments and our experiments is fundamentally different than the expected theoretical peak as calculated by Krasheninnikov [36].

Carbon nanotubes present a rich spectrum of plasmon modes. For metallic SWCNT gapless plasmon modes (far infrared frequency range) exist [30], in addition to the high frequency modes (UV range) and the depolarization van Hove plasma resonances. Bommeli et al. conducted reflectivity measurements on carbon nanotubes, from far-infrared up to ultraviolet [31], and detected the low-energy π -plasmon contribution around 115 meV. The dispersion relation of such a quasi-1D plasmon mode for a (9,0) SWNT is linear [32]. We propose that the zero bias anomaly is possibly the cumulative result of a charge depleted region around the H-patches and a quasi 1D plasmon assisted tunneling regime. The extent of charge depleted region on carbon based materials has been discussed in detail in Section 4.3.3 of this thesis. The extent of the charge depleted region might be smaller than on the H/HOPG system since these SWCNTs are deposited on gold surface and charge transfer could facilitate the screening of the H impurity. As already observed for the H/HOPG system, in the H/CNT system the same transition between the zero bias anomaly signature and Fano interference is present. Function of distance from the H patch, this transition was quantifiable for the H/HOPG system. However, hydrogen can be chemisorbed on CNT and not be visible in the STM topography since not all the CNT is visible to STM imaging. Thus, quantifying the transition between the aforementioned signatures in the LDOS function of distance from the H patch is not trivial. The STS curves 1 - 3 from Figure 5.11 might be located in a H rich region and a strong under-screened regime leads to the zero bias anomaly. We propose that the experimental data 7 - 13 from Figure 5.11 are acquired in a region where screening is more efficient than where ZBA is observed. Spectra 6, 7, 9, 11 and 12 from Figure 5.11

exhibit a Fano line-shape. The topography imaging of this H-patch is insufficient to correctly estimate the H-coverage but sufficient to estimate the distance between the hydrogen patch and the lateral position where the STS data was acquired. Thus we estimate from the topography in Figure 5.11 that spectra 9, 11 and 12 are acquired at less than 0.2 nm away from the hydrogen patch. Similarly, spectrum 10 is at about 0.4 nm away. The results of Buchs et al. [10, 11] reveal a very sharp peak next to structural defects, centered at the Fermi level. Their data is acquired at less than 0.5 nm away, or at about 3 nm away. At 3 nm away from the defect sites, the LDOS around the Fermi level is flat as in our experimental observations. They interpret the peak as due to a defect induced localized state. Similar to the V-shaped gap observed in the hydrogen on HOPG system, we interpret the dip at the Fermi-level as a possible result of the electron-phonon or electron-phonon and 2D-plasmon coupling. The width of this dip at the Fermi level of about 190 meV is more or less equivalent to the flat acoustic phonon band region at 109 meV [33] or plasmon/phonon peak. In our opinion, the transition between the zero bias anomaly and the Fano line-shape is a signature of a possible increase in the charge density available for screening with in turn will represent the same electron - phonon or electron - phonon and 2D-plasmon coupling as a Fano line-shape in the LDOS. As STS data 12 presented in Figure 5.11 show the E_{res} (equation 2.5.1) is located at about -100 meV. This value is also in good agreement with the flat acoustic phonon band region at 109 meV or plasmon/phonon peak.

Confined states in a metallic nanotube section

A short nanotube section, enclosed by a kink and a defect region on a metallic nanotube, was observed with STM. Figure 5.15 shows this nanotube, where the topographical features have a duplicate image due to convolution with a double tip. Although the image quality was rather poor, a series of tunneling conductance spectra were recorded on the tube to find out if the H patches on the tube would have an effect on the LDOS. In the top part of the image, there is a kink in the tube indicated by A. The first section of this tube to be discussed is the part between this kink and the first defect region found from A downwards in the image, marked by B. The tube section between A and B is defect-free and has a length of $\simeq 14$ nm. Tunneling conductance spectra were recorded at the positions indicated by dots in Figure 5.15. Spectra recorded between the points A and B show features close to the E_F as shown in Figure 5.16 and these features are identified as oscillations caused by electron confinement, a quantum size effect as explained below.

Experiments on shortened nanotubes with lengths of $\simeq 30$ nm showed the presence of quantum size effects [29]. In a macroscopic conductor, the resistivity and the

5. Tailoring the electronic structure properties of single walled carbon nanotubes by H chemisorption

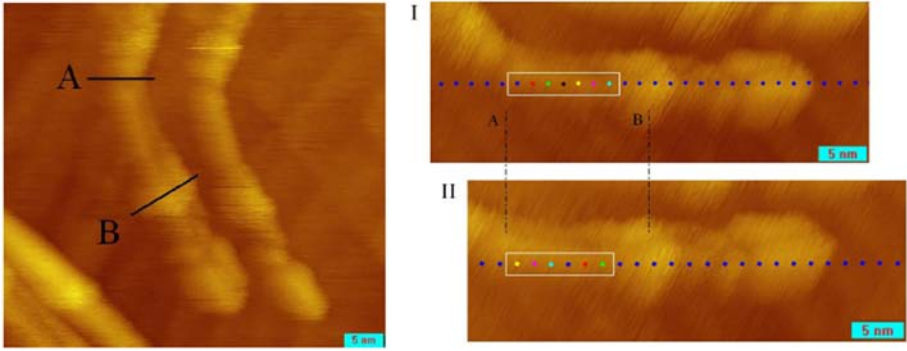


Figure 5.15: Topographic STM images of a short metallic nanotube section enclosed by a kink and a hydrogen patch. Topography acquired at 77 K with $U_{gap}=1.10$ V and $I_t=1.07$ nA. Left image: 50×50 nm², right image: 35×15 nm². Because of the double ending of the STM tip, an identical shadow image of the tube is observed in the image of the left. The upper image (I) is a rotated cut-out of the left image, the lower image (II) is an STM image recorded direct after image I. The dots in I and II indicate spectroscopy locations.

conductivity are physical properties which do not generally depend on either the length of the wire L or the applied voltage to the sample but only on the material. However, when the size of the wire becomes small compared with the characteristic lengths for the motion of electrons (mean free path), then both the resistivity and conductivity will depend on the length L through quantum effects. In the quantum regime, the electrons act like waves that show interference effects, depending on the boundary conditions. In this case, the boundaries are formed by the impurities and defects that are present in the nanotube. Peak-peak separation in the spectra in Figure 5.16 is in the order of 140 meV, and the length of the nanotube section between the points A (kink in the tube) and B (hydrogen induced defect) is 14 nm. Using the simple approximate formula $E = hv_F/2L$ with $v_F = 8\times 10^5$ m/s the Fermi velocity and $L = 14$ nm, peak separation ΔE should be $\simeq 120$ meV [34]. This separation does not fit too well with the peak separation for the first peaks around the Fermi level, but for the next peaks the value of 120 meV is quite a good approximation. Thus, we conclude that for a section of a metallic nanotube we observed the confinement of electrons due to the boundaries created by hydrogen patches and a topological kink.

Metal to insulator transition in a metallic CNT due to hydrogen chemisorption

Tunneling conductance spectroscopy recorded on dense hydrogen decorated sections of metallic nanotubes provided spectra that bear resemblance with the semiconductor

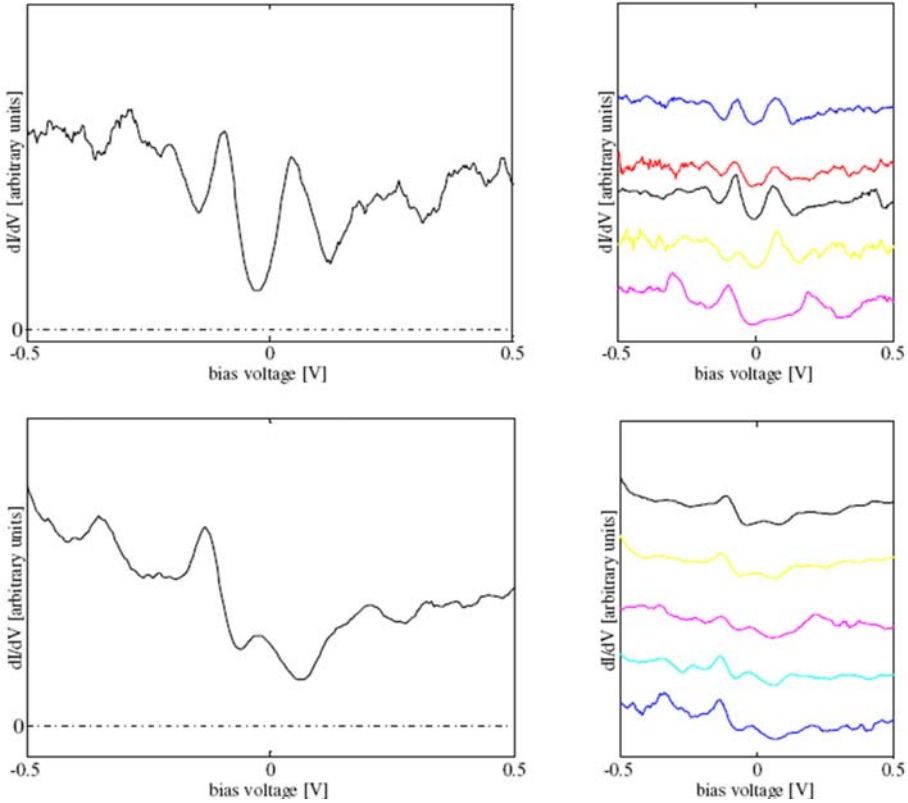


Figure 5.16: Tunneling conductance data, dI/dV , showing wide and equidistant peaks with a separation of $\simeq 120\text{-}140$ meV. The spectra shown in the large panels is the mean of the spectra shown in the insets (data in the insets is subsequently shifted by an offset). The frequency of the modulation signal was 1.232 kHz and the amplitude was 12 mV peak-to-peak.

5. Tailoring the electronic structure properties of single walled carbon nanotubes by H chemisorption

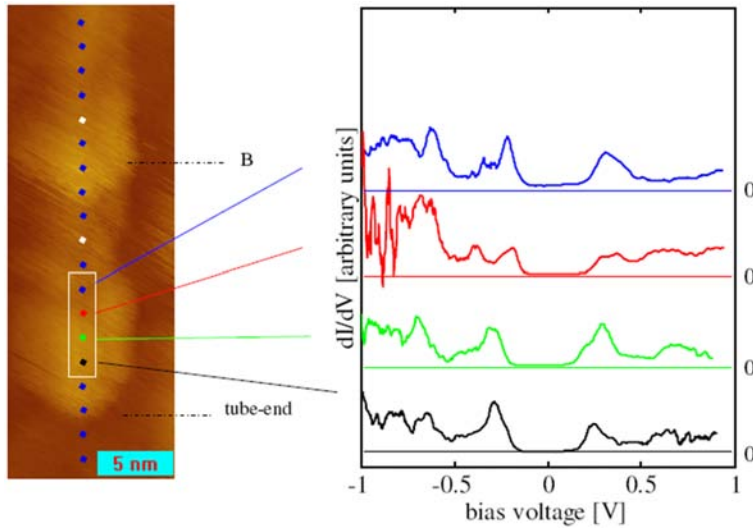


Figure 5.17: STM image and tunneling conductance data, dI/dV , recorded in the hydrogen patch region, towards the end of the nanotube. The four spectra shown in the right panel are subsequently shifted by an offset. The tunneling spectra show a semiconductor-like peak arrangement, with a zero conductance plateau centered around the Fermi level. The width of the energy gap is $\simeq 0.55$ eV, the zero level is indicated by the horizontal lines. $U_{gap}=1.10$ V, $I_t=1.07$ nA, image size: 12×32 nm².

nanotube spectra.

Spectroscopy measurements at the tube end - STM image with spectroscopy point depicted in Figure 5.17 - provided a spectrum with a band gap of $\simeq 0.5$ eV. A band gap of about 0.5 eV would correspond to a semiconducting nanotube with a diameter of 1.26 ($E_{gap} = 0.55$ eV) to 1.59 nm ($E_{gap} = 0.45$ eV). The diameter measured on the topographic image is indeed in this diameter range, but the not-hydrogen covered regions show a metallic behavior as indicated by the previous subsection. In order to exclude measurement uncertainty, the data was recorded several times, in a row, and the results have shown a good reproducibility. Furthermore, there is a resemblance with the LDOS of the metallic tube with the (14,2) chiral index presented above. A semiconducting fingerprint was also measured on the hydrogen decorated metallic nanotube with a small H patch.

These semiconductor-like spectra recorded on the metallic nanotube indicate that the nanotube's conducting behavior is locally changed. The transformation from a metallic character of the CNT to a semiconducting character, although not unexpected [35], is nevertheless interesting. Calculations studying the DOS of hydrogen

decorated CNT s, in particular on a (5,5) armchair nanotube, predicted a transition to a semiconducting behavior for specific hydrogen coverage on the CNT [35]. However, in comparison to the theoretical work of Park, the CNT is not orderly covered with H and furthermore the CNT itself has a different chiral index. The new semiconducting character of the CNT can be rather easily understood when knowing that, in similitude to the experiments conducted on H/HOPG, upon hydrogen chemisorption the sp^2 character of the C atom in the lattice of the CNT changes to an sp^3 character. As the sp^2 character presents π electrons (that are delocalized in the carbon lattice), while a sp^3 character consists of σ electrons (localized electrons) a lack of free charge carriers translates in a band gap opening.

In conclusion, locally, as a function of hydrogen coverage, a metallic nanotube can be transformed into a semiconducting one just by hydrogen chemisorption. A more detailed investigation of this phenomenon was not pursued, but nevertheless it may prove to be an efficient method to transform the metallic character of the nanotubes into a semiconducting one, since during the fabrication process of CNTs it is hard to produce only semiconducting carbon nanotubes.

5.3.4 Chemisorbed hydrogen on semiconducting CNT

All the experimental results presented in the previous three subsections explored the influence of chemisorbed hydrogen on metallic nanotubes. This subsection will address the question if any changes in the LDOS of a semiconducting nanotube can be observed when hydrogen is chemisorbed. A nanotube with a few hydrogen patches was identified as a semiconducting nanotube. On this tube, tunneling conductance spectra were recorded in a rectangular measurement grid. The quality of the imaging was poor, thus a correct determination of the chiral index was not possible. Figure 5.18 shows in the left image, marked by ellipses typical hydrogen patches. The right hand side image, from the above-mentioned figure, depicts with dots the spatial locations where spectroscopy data was collected and it is the same region as depicted in the left-hand side image. The separation distance between two neighboring measurement points is approximately 0.9 nm.

There is a high correlation between the tunneling conductance spectra recorded at horizontally equal positions, e.g. the spectrum recorded in the most left points in the three white rectangles is very similar. The data recorded in the three white triangles is shown in Figure 5.19. The resemblance between the lines of the same color, in the three panels from Figure 5.19, indicate that the tunneling conductance measurements are not too much position dependent in respect to the direction perpendicular to the tube axis. The evolution of the tunneling conduction spectra shows peaks arising in the gap, very close to the first VHS pair. These additional peaks are more pronounced

5. Tailoring the electronic structure properties of single walled carbon nanotubes by H chemisorption

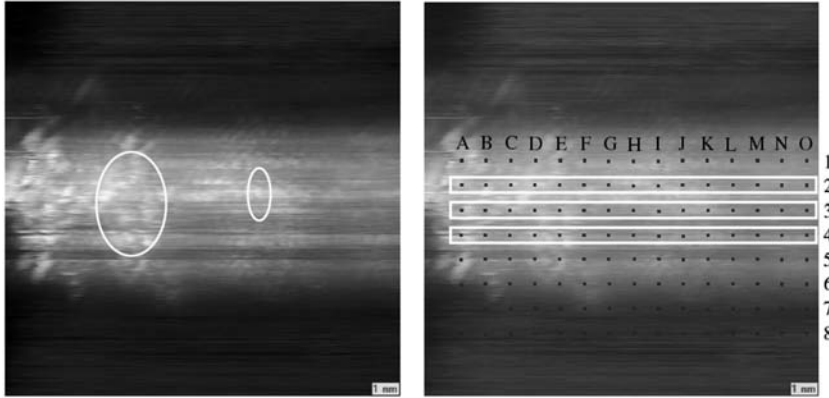


Figure 5.18: Topographic STM image ($2\times$) of a semiconductor nanotube at 77 K. Left panel: The ellipses indicate the hydrogen patches. Right panel: The dots indicate the spectroscopy locations on a rectangular measurement grid. Rows 2, 3 and 4 of the grid are enclosed by the long white rectangles. Scanning parameters: $U_{gap} = 0.7$ V, $I_t = 469$ pA, scanning size is 15×15 nm².

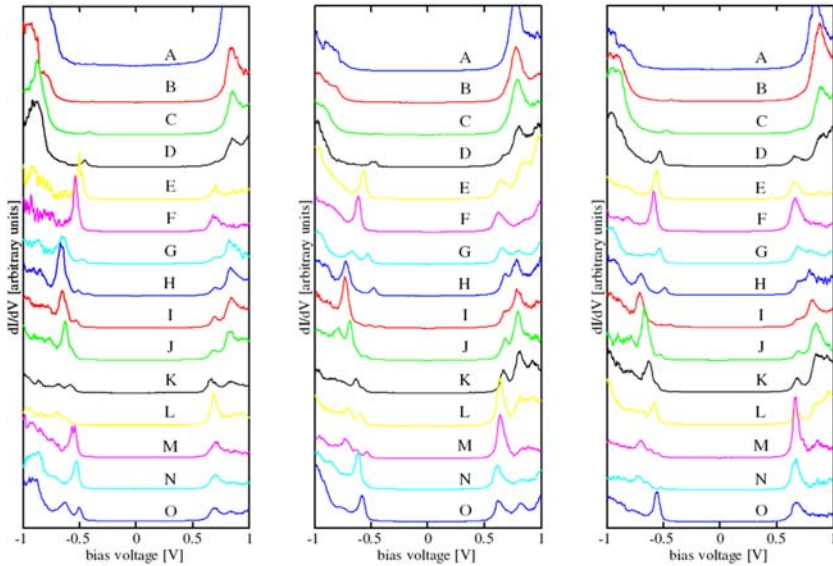


Figure 5.19: Tunneling conductance spectra, dI/dV , recorded on a semiconductor nanotube with two different regions. The STS data presented were recorded in the second, third and fourth row (1, 2, 3) of dots in Figure 5.18. The horizontal positions are indicated by A, B, C, ... The Spectra from D, E and F indicate the presence of extra peaks in the gap, resulting in a reduction of the band gap.

in the spectroscopic data recorded in positions D, E and F. The net result given by the appearance of new electronic states within the gap is a reduction of the CNT band gap. The positions of these points correspond with the position of the hydrogen patches indicated by the ellipses in Figure 5.18.

The measurements on semiconducting nanotubes decorated with hydrogen indicate a reduction in the intrinsic CNT band gap by the appearance of new states in the vicinity of the first VHS. Due to the poor topography imaging more experiments are required in order to confirm this observation. In addition, the chiral index is necessary to be determined before the hydrogen treatment. These electronic states are similar to the quasibound electronic states introduced by Stone-Wales defects in SWCNT [40], as described in Paragraph 2.2 of this thesis and exemplified in Figure 2.10.

5.4 Conclusions

A major part of the work was dedicated to the sample preparation procedure. The substrate for SWCNT deposition was prepared by flame annealing, creating clean and atomically flat Au(111) terraces. Carbon nanotubes were dispersed in 1,2-dichloroethene (DCE) solvent for deposition. One or two droplets of the sonicated dispersion were applied on the gold surface. The results on arc-discharge carbon nanotubes reveal that these are mostly present as bundles. Individual CoMoCat carbon nanotubes were easier to separate from conglomerates with DCE. Consequently, the STS results presented in this chapter used this method. The carbon nanotube surface density achieved, with this preparation procedure, varied between 1 and 10 per square micrometer.

Hydrogen deposition using the RF plasma discharge setup resulted in the creation of hydrogen patches on the nanotube walls. While high-energy ion treatment of CNT reveal the creation of structural defects, the RF plasma discharge source creates H atoms and low energetic H^+ ions. Thus, the structures observed on the CNT walls are induced by H chemisorption. More evidence supporting this reasoning has been given in Section 4.2 of this thesis. Topographic differences between the clean nanotubes and the H treated nanotubes suggests that these features arose from the H exposure since a longer exposure induces more hillock features, as observed in our STM topography images.

Tunneling conductance data coupled with atomically resolved STM imaging of CNT enabled the identification of the chiral number indices of the SWCNT s. Both metallic and semiconductor carbon nanotubes have been observed. With STS we studied the influence of chemisorbed H on the electronic structure properties of SWCNT s, metallic and semiconducting. In a semiconducting SWCNT hydrogen treatment cre-

5. Tailoring the electronic structure properties of single walled carbon nanotubes by H chemisorption

ates new electronic states that are arising in the band gap, close to the first VHS. These electronic states reduce the band gap of the SWCNT with about 200 meV. In the case of hydrogen chemisorbed on metallic SWCNT, several effects have been observed. First, towards the end of a metallic SWCNT a large patch of hydrogen was observed. STS performed on that patch indicated a full metal to insulator transition. The measured band gap was about 0.55 eV. The opening of the band gap in the metallic SWCNT is attributed to the local re-hybridization of the C bonds from sp^2 to sp^3 upon H chemisorption. Third, on the same metallic SWCNT, STS data acquired in between two patches with high concentration of chemisorbed H revealed the presence of confined electronic states. Signature of a quantum behavior of the electrons, interference of the electron wave scattering on H patches (acting as wave barriers) was observed. Upon H deposition on metallic SWCNT s two features have been observed at the Fermi level. First, a zero bias anomaly. Second, a Fano-like line shape at very small distances from the H patches. We propose that these features arise from the possible electron - phonon or electron - phonon and 2D-plasmon coupling. We expect that the zero bias anomaly and the Fano resonance are H-coverage dependent and a transition in between the two features could be controlled by the amount of chemisorbed hydrogen. For future experiments it would be interesting to make, as for the H/HOPG system, a temperature dependent investigation on the role of H tailoring of the SWCNT LDOS. With additional support of theoretical studies, the nature of this zero bias anomaly might be fully understood. Since charge conductivity in metallic individual SWCNT can be characterized with transport measurements, it would be interesting to verify the role of H chemisorption on metallic SWCNT conductance. We expect that a metal to insulator transition should be visible upon H chemisorption. This transition could be easily reversible by temperature desorption of the H from the CNT.

Bibliography

- [1] Z. Zhang and C.M. Lieber. *Appl. Phys. Lett.* 62, 2792 (1993).
- [2] H.W.Ch. Postma, T. Teepen, Z. Yao, M. Grifoni, and C. Dekker. *Science* 293, 76 (2001).
- [3] C. Dekker. *Physics Today*, 22 (1999).
- [4] A. Rubio, D. Sanchez-Portal, E. Artacho, P. Ordejn, and J.M. Soler. *Phys. Rev. Lett.* 82, 3520 (1999).
- [5] R. Saito, M. Fujita, G. Dresselhaus, and M.S. Dresselhaus. *Phys. Rev. B* 46, 1804 (1992).

- [6] www.arrandee.com
- [7] C. Rettig, M. Bodecker, and H. Hovel. *J. Phys. D.: Appl. Phys.* 36, 818 (2003).
- [8] A. Buldum and J.P. Lu. *Phys. Rev. Lett.* 83, 5050 (1999).
- [9] J.W. Janssen, S.G. Lemay, L.P. Kouwenhoven, and C. Dekker. *Phys. Rev. B* 65, 115423 (2002).
- [10] G. Buchs, P. Ruffieux, P. Groning, and O. Groning. *J. of Physics: Conference Series* 61, 160 (2007).
- [11] G. Buchs, P. Ruffieux, P. Groning, and O. Groning. *Appl. Phys. Lett* 90, 013104 (2007).
- [12] www.oaresearch.co.uk
- [13] www.swnano.com
- [14] L.C. Venema, V. Meunier, P. Lambin, and C. Dekker. *Phys. Rev. B* 61, 2991 (2000).
- [15] L.C. Venema. *Ph.D. Thesis*, Delft University (2000).
- [16] F. Wittebrood. *Master Thesis*, Eindhoven University of Technology (2007).
- [17] O. Gulseren, T. Yildirim, and S. Ciraci. *Phys. Rev. B* 65, 153405 (2002).
- [18] P. Lambin, V. Meunier, and A. Rubio. *Science and Application of Nanotubes*, pages 17-33, Springer US (2002).
- [19] M. Ouyang, J.-L. Huang, C.L. Cheung, and C.M. Lieber. *Science* 292, 702 (2001).
- [20] P. Lambin, G.I. Márk, V. Meunier, and L.P. Biró. *Int. J. Quantum Chem.* 95, 493 (2003).
- [21] P. Delaney, H.J. Choi, J. Ihm, S.G. Louie, and M.L. Cohen. *Nature* 391, 466 (1998).
- [22] P. Delaney, H.J. Choi, J. Ihm, S.G. Louie, and M.L. Cohen. *J. Mat. Res.* 13, 2389 (1998).
- [23] A. Rubio, D. Sanchez-Portal, E. Artacho, P. Ordeijn, and J.M. Soler. *Phys. Rev. Lett.* 82, 3520 (1999).
- [24] C.L. Kane and E.J. Mele. *Phys. Rev. Lett.* 92, 225502 (2004).

5. Tailoring the electronic structure properties of single walled carbon nanotubes by H chemisorption

- [25] E.J. Duplock, M. Scheffler, and P.J.D. Lindan. *Phys. Rev. Lett.* 92, 225502 (2004).
- [26] V.H. Crespi and M.L. Cohen. *Phys. Rev. Lett.* 79, 2093 (1997).
- [27] B.L. Altshuler and A.G. Aronov. *Phys. Rev. Lett.* 44, 1288 (1980).
- [28] L.C. Venema, J.W. Janssen, M.R. Buitelaar, J.W.G. Wildoer, S.G. Lemay, L.P. Kouwenhoven, and C. Dekker. *Phys. Rev. B* 62, 5238 (2000).
- [29] L.C. Venema, J.W.G. Wildoer, J.W. Janssen, S.J. Tans, H.L.J. Temminck Tuinstra, L.P. Kouwenhoven, and C. Dekker. *Science* 283, 52 (1999).
- [30] K. Kempa. *Phys. Rev. B* 66, 195406 (2002).
- [31] F. Bommeli, L. Degiorgi, P. Wachter, W.S. Bacsa, W.A. de Heer, and L. Forro. *Solid State Commun.* 99, 513 (1996).
- [32] L.M. Liz-Marzán and M. Giersig. Low dimensional systems: theory, preparation, and some applications. *Luwer Academic Publishers*, 40-41 (2002).
- [33] M.S. Dresselhaus and P.C. Eklund. *Adv. in Phys.* 49, 705 (2000).
- [34] T. Maltezopoulos, A. Kubetzka, M. Morgenstern, R. Wiesendanger, S.G. Lemay, and C. Dekker. *Appl. Phys. Lett.* 83, 1011 (2003).
- [35] K.A. Park, K. Seo, and Y.H. Lee. *J. Phys. Chem. B* 109, 8967 (2005).
- [36] A.V. Krasheninnikov, K. Nordlund, M. Srivio, E. Salonen, and J. Keinonen. *Phys. Rev. B* 63, 245405 (2001).
- [37] B. Kitiyanan, W.E. Alvarez, J.H. Harwell, and D.E. Resasco. *Chem. Phys. Lett.* 317, 497 (2000).
- [38] www.ou.edu/engineering/nanotube/comocat.html.
- [39] D.E. Resasco, W.E. Alvarez, F. Pompeo, L. Balzano, J.E. Herrera, B. Kitiyanan, and A. Borgna. *J. Nanopart. Res.* 4, 131 (2002).
- [40] H.-T. Yang, L. Yang, J. CHen, and J. Dong. *Phys. Lett. A* 325, 287 (2004).

Chapter 6

Towards persistent current measurements on nanoscopic gold rings

6.1 Introduction

Persistent currents (PC) in normal metal rings have been intensively studied in the last two decades in the quest to bridge the gap between the theory and experiment [1–7]. PC give rise to a periodic orbital magnetic moment with a periodicity corresponding to one flux quanta, h/e . Experimentally, persistent currents have been measured on both ensembles of rings and on individual rings [8, 9]. Surprisingly, on ensembles of rings the magnetic moment is periodic with $h/2e$, since ensemble averaging imposes a zero total magnetic moment. GaAs/AlGaAs rings (semiconducting) have shown a good concordance between theory and experiment. Recent measurements on metallic nano-rings (Al and Au) show a good concordance between theory and experiment [10, 11]. In contrast to the nano-rings measured in the experiments of Bluhm and Bleszynski-Jayich (micrometers in diameter), the gold nano-rings we intend to study have the Fermi wavelength almost equal to the electron mean. The criterium of ballistic electron conduction regime is required to test the PC theory for metallic rings. To achieve a ballistic conduction regime for a gold nano-ring, a first requirement is to decrease the size of the ring (the perimeter), to nanometers instead of micrometers. For nanoscopic-dimensioned rings, the signature of the persistent current is expected to be about 100 times larger than for the microscopic sized rings. Usually, the micrometrical rings are created by standard lithographic techniques. These techniques do not yet allow creating nanoscopic-sized rings on a substrate. If persistent currents can be measured in these nanoscopic rings the en-

6. Towards persistent current measurements on nanoscopic gold rings

semble averaging effect might disappear due to the transition to a ballistic electron conduction regime where theory predicts a h/e periodicity of the magnetic moment. Another fundamental question that this experiments might answer, is related to the nature of the magnetic response from the ensemble. Is it a diamagnetic response as suggested by theory? This chapter summarizes preliminary magnetic measurements results obtained on ensembles of metallic Au nano-rings created by colloidal lithography. We found that colloidal lithography offers experimentalists the possibility to create ensembles of nano structures that theoretically approach the ballistic electron conduction regime.

6.2 Experimental

Colloidal lithography [12] is a self-assembly technique mainly based on the interaction between polystyrene particles (PP) and substrate. The driving force of the self-assembly process is the electrostatic force. In a buffer solution the electrostatic force is repulsive for PP - PP interaction, while between PP and the substrate the electrostatic force is attractive.

The substrate used in the experiments was SiOx. The samples were cut from a Si wafer that presents a ~ 1 micrometer thick silicon oxide layer on top. The sample dimension is kept $\sim 5 \times 5$ mm². To prepare the substrate for PP deposition, sequential sessions of ultrasonic treatment with solutions (sulphuric acid, acetone and methanol) were used. The minimum sonication time was 15 minutes. Prior to PP deposition, the cleaning process of the substrate was checked with atomic force microscopy (AFM) on random samples from a batch. The vast majority of the samples ($\sim 90\%$) presented a RMS roughness of less than 0.5 nm. This value was considered to be sufficient to proceed with PP deposition since the minimum height expected for Au nanorings is ~ 3 nm. Samples that did not pass the surface roughness criteria have been disregarded at this initial step. As mentioned above, the PP self-assembly process relies on the electrostatic attraction between the PP and the substrate. In order to achieve this, the silicon oxide surface has been sequentially treated with three aqueous solutions (tri-layer), 30 s each. In between the steps, the sample was washed with a gentle rinse of milli-Q water and blown dry with dry nitrogen. The solutions in order of usage are: 2% (by weight) of poly(diallyldimethylammoniumchloride) (PDDA, MW 200000 - 350000), [13], then 2 % (by weight) in poly(sodium 4-styrenesulfonate) (PSS, MW 70000) [13] and finally 5 % (by weight) aluminum chloride hydroxide (ACH) [14]. After this preparation step the sample roughness has been studied again yielding no significant roughness increase.

The absorption of PP onto the chemically modified SiOx substrate is done from

6.3 AFM studies of polystyrene particles and gold nanostructures

an aqueous solution. Two differently sized (in diameter) PP were used: 19 nm and 110 nm. The concentration of the PP in the aqueous solution was varied between 0.001% and 0.5% by volume. The adsorption time of the PP onto the substrate was varied between 10 s and 15 min. Flushing the sample with milli-Q water stopped the adsorption of the PP. In order to dry the sample, two methods have been used. Either by blowing the sample dry with a gentle flow of N₂ gas, or by slowly evaporating the liquid by placing the sample in an oven, at 85 °C.

Summarizing, at this point of the preparation procedure, the sample consists of PP adsorbed on a thin triple layer on top of the silicon oxide. To create gold nano-rings on the surface, the following step was the thermal evaporation of a thin gold layer, under HV environment, 10⁻⁶ mbar. During deposition, the thickness of the Au film is controlled with a quartz balance. The height of the gold layer was chosen according to the height of the PP deposited on the sample. The film thickness is chosen to be about two thirds of the PP height (according to PP manufacturer). It can be assumed that since gold is mobile on the surface during the evaporation process, it is diffusing also underneath the PP. After the sample has been covered with the gold layer, the gold layer that is not shadow masked by the PP is removed by Ar⁺ sputtering. That step was made in another UHV chamber (base pressure 10⁻¹⁰ mbar) at an incoming sputtering beam energy of 1.5 keV. The sputtering process is considered finished when the collected sample current drops to values smaller than 1 μA. In this step the PP are used as a shadow mask for the underlying gold layer. It is not known if the tri-layer is sputtered along with the Au layer. It can be speculated that sputtering of the tri-layer occurs, yet since we do not expect a very closed packed structure, most of the tri-layer or fragments of its constituents will be present on the surface. A complete sputtering of the tri-layer is not foreseen since both the SiO_x and the tri-layer is insulating, the sputtering process would be self-stopping due to surface charging.

The last step in the preparation procedure was the removal of the PP by making use of an ozone treatment. The ozone is generated with an UV lamp. To completely remove PP from the surface, the samples are flushed with demineralized water. After all the above-mentioned steps, the sample's surface should present Au nano-rings.

6.3 AFM studies of polystyrene particles and gold nanostructures

6.3.1 AFM characterization of the polystyrene particles

Before proceeding to the PP deposition onto the substrate, AFM topography studies were used to check the roughness of the samples after the cleaning of the silicon oxide

6. Towards persistent current measurements on nanoscopic gold rings

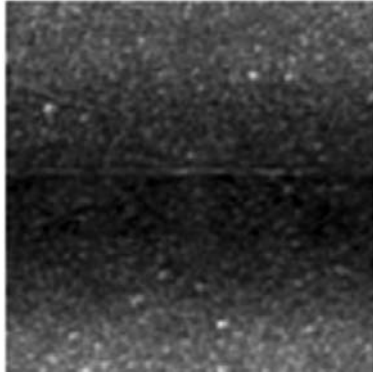


Figure 6.1: Topographic AFM image of $1 \times 1 \mu\text{m}^2$ of silicon oxide with the triple layer deposited on top. The roughness is measured to be smaller than 0.5 nm.

and the triple layer deposition. Several samples were scanned with AFM. The surface roughness was found to be around 0.5 nm or less, as shown in Figure 6.1. This implies that the substrate is suitable for PP deposition and the PP should be easily identifiable by AFM topography measurements. For all samples, the preparation procedure up to the PP deposition was kept identical.

First, 110 nm in diameter PP were adsorbed on the substrate. A batch of five samples was prepared. The PP solution concentration was kept constant while the adsorption time was varied between 40 s and 300 s. In order to check if the drying method of the sample induces coverage difference, two of the five samples were dried out differently. One of the samples was dried in the oven while the other one was dried by a gentle flow of dry N_2 gas. The samples were again investigated with AFM. As it can be observed from Figure 6.2 all five samples present nicely dispersed PP, with a PP coverage (footprint) of about 32%. The coverage (C) was measured on the topographic image but the result did not take into account AFM tip corrugation. However, counting the PP on a specific area, yields the correct number (N) of PP. N varies for this five samples between 100 and 138 particles per $9 \mu\text{m}^2$. In this experiment it was observed that the immersion time (T) of the substrate in the PP solution does not drastically influence the number of PP found on the substrate since no large differences in PP concentration were observed between samples immersed in the solution for 40 s or 300 s. One might expect that the surface concentration of PP increases with time. This was not observed in our experiments for the particular case of placing only a drop of solution on the sample surface. At the aforementioned PP concentration in solution, if the sample is immersed in the solution, at least several layers of PP are observed on the surface with AFM topography. We assume that in

6.3 AFM studies of polystyrene particles and gold nanostructures

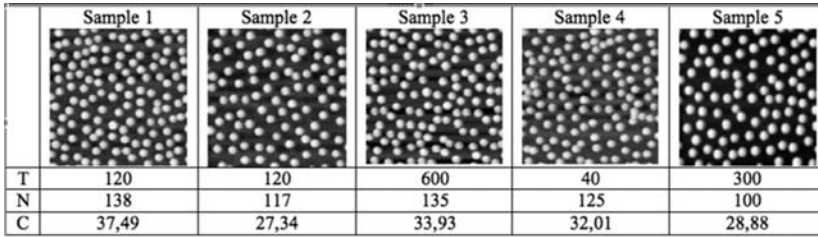


Figure 6.2: Topographic AFM images of $3 \times 3 \mu\text{m}^2$ of 110 nm PP adsorbed on the substrate, labeled Sample 1 to 5. Sample 1 is dried in the oven at 85°C while the rest are dried with a gentle flow of dry N_2 . T represents the deposition time of the PP from the aqueous solution, in s . N represents the number of PP found on one squared micrometer of each sample, while C represents the coverage of the sample with PP, expressed in % .

case of a single droplet, covering the entire surface, the equilibrium between particles bound to the surface and in solution is reached reasonably fast. The equilibrium, thus the concentration of PP on the sample surface is given by the quantity of charge within triple layer and the number of PP found in the droplet.

These early fruitful results paved the way to test if making use of the colloidal lithography technique can produce gold nano-structures with smaller dimensions. The PP aqueous solution concentration and PP deposition time were kept similar with the parameters mentioned above while trying to produce gold nano-structures from PP with a diameter of 19 nm. However, the first samples were far from successful. The samples presented either a very low amount of PP, or more than 1 ML of particles on the substrate and/or clustering. It was also identified that blowing the sample with a gentle flow of dry N_2 gas removed the weakly electrostatic bounded PP from the substrate. A first solution was to evaporate the aqueous solution from the sample by placing the sample in the oven, at 105°C . Although, PP were identified on all the samples, clustering or several monolayers of PP were still observed. In order to reduce the amount of PP attached on the substrate, the aqueous solution was further diluted until the concentration by volume was 0.02%. AFM topography investigations revealed properly dispersed PP as depicted in Figure 6.3. According to the manufacturer of the PP [15] the diameter should be $19 \text{ nm} \pm 1\%$. In the next section a detailed analysis of the PP height distribution is carried out.

6.3.2 AFM characterization of gold nano-structures

On the samples with 110 nm PP, a 40 nm layer of Au was evaporated. Subsequently the samples were sputtered with Ar^+ for half an hour and UV treated for another 2 h.

6. Towards persistent current measurements on nanoscopic gold rings

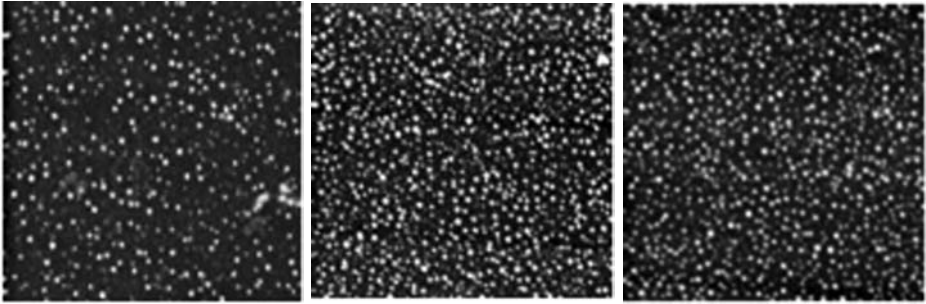


Figure 6.3: Topographic AFM image of $3 \times 3 \mu\text{m}^2$ of PP. The deposition time from the aqueous solution was 30 s and the solution concentration 0.02% by volume.

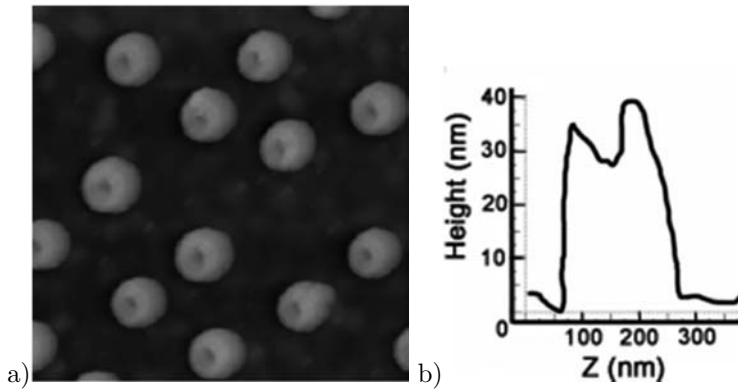


Figure 6.4: a) Topographic AFM image of $1.3 \times 1.3 \mu\text{m}^2$ of Au nano-structures. b) Cross section made over a gold nanostructure indicating the height.

Afterwards, the samples were investigated with AFM. Topographic images revealed the presence of different structures than previously measured on the surface. Results are depicted in Figure 6.4. First, one must notice the similitude between the structures. Second, in the middle of the structures a depression is measured; more clearly visible in the cross-section from Figure 6.4b. Third, the height of these structures is slightly less than half of the PP height. In conclusion, it is reasonable to conclude that the new structures are Au nano-structures left after the PP removal.

However, a full opening in the Au nano-structures could not be measured with the AFM tips (NSC12, Ultrasharp, NT-MDT) used to produce these results due to the tip convolution.

Following the same nano-rings preparation procedure but for PP with a diameter of 19 nm, the AFM topography yielded images as shown in Figure 6.5. The height

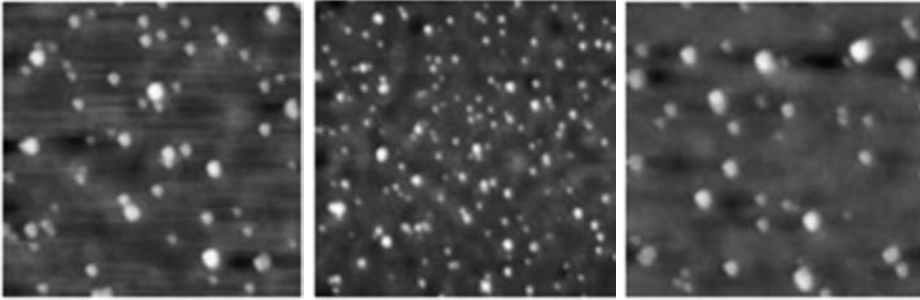


Figure 6.5: Topographic AFM image of $0.5 \times 0.5 \mu\text{m}^2$ of Au nano-structures. As it can be observed from all three images the height of the structures is not similar.

of the Au layer deposited for the 19 nm PP was about 10 nm. There are two important observations to be made when examining the topography images. The first observation is that there is no dip visible in the middle of the structure. The second observation is that the heights and widths of the structures differ in contrast to what is observed in Figure 6.4 for the larger structures. The first observation is rather easy to understand due to the fact that the gold rings have a diameter comparable with the AFM tip radius (in the order of 10 nm), thus due to convolution the opening may never be observed with such blunt AFM tips.

To understand the second observation of the previous paragraph, a statistical analysis of the AFM measured heights for PP and nano-structures was done. The results are depicted in Figure 6.6. According to manufacturer datasheet, the diameter of the PP is $19 \text{ nm} \pm 1\%$. However, the normal distribution measured suggests that PP diameters between 10 nm and 28 nm are expected too. Since the PP are used as a mask for creating the gold nano-structures, smaller PP will produce smaller Au structures. This is what has been observed by scanning with the AFM the gold structures. Statistics on many structures is not only useful to understand the size distribution of the gold nano-structures but a one to one correlation between the PP size and the gold nano-structures size might provide a hint regarding the true diameter of the gold nano-structures. As a remark, if one would like to create identical nano-structures using this method, the PP particle would have to have smaller diameter dispersion.

The ratio between the height of the gold nano-structures and the height of the PP is about 0.26 (Figure 6.6). Since it can be easily understood that all the gold material that was deposited by evaporation is going to be sputtered unless masked by the PP, then accounting for the ring height the true diameter of the diameter of the gold nanostructure is around 17 nm. If the PP is considered to be spherical, a

6. Towards persistent current measurements on nanoscopic gold rings

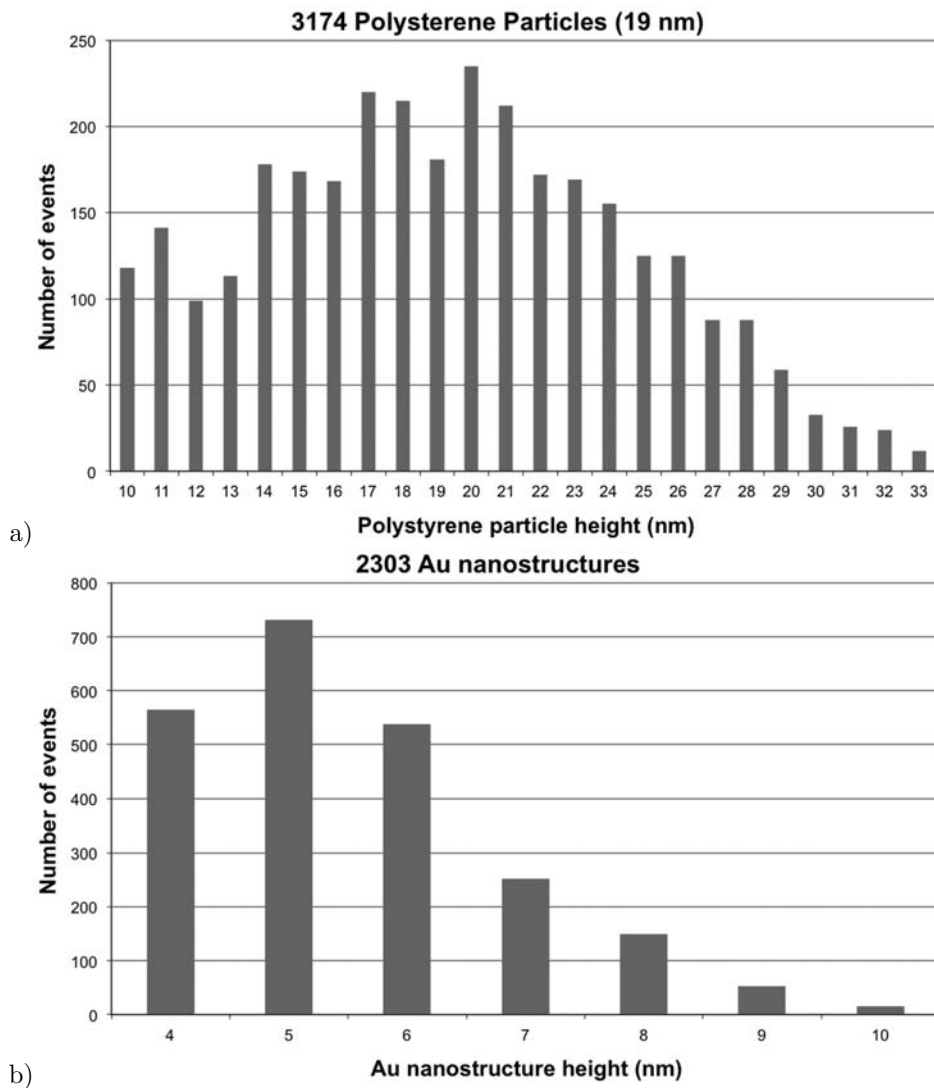


Figure 6.6: Height distribution of: a) 3174 PP, b) 2303 gold nanostructures. The PP diameter is normally distributed, mean diameter value is 19 nm.

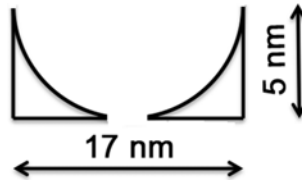


Figure 6.7: Au ring cross-section with characteristic dimensions.

cross-section of the gold ring might have the dimensions depicted in Figure 6.7.

Since preparing the Au nano-structures involved nine sequential steps, difficult sample handling, ultra-clean manipulation and preparation steps, the rate of success was rather limited (less than 10 % of the samples were useful from more than 300 samples prepared). From this percentage only around 10 samples were studied with SQUID. The preparation process has proved to be time-consuming and not to be easily reproducible due to the large amount of variables involved in the preparation procedure. Under more controlled conditions (solutions, UHV sputtering and environment, fast analyzing times, large batching) the success rate in sample preparation may be drastically improved.

6.4 DC SQUID measurements on ensemble of gold rings

The DC SQUID technique has been described in Chapter 3 of this thesis. To make the DC SQUID experiments comparable, some of the experimental variables were kept constant: sample size ($5 \times 5 \text{ mm}^2$), experimental temperature (4.9 K), maximum magnetic field strength (up to 5 T, setup limited), sample translation steps (32), translation distance (4 cm), PP size (19 mm). A reference sample accounts for the non-Au-ring-structures related sample magnetism. The reference sample for this experiments consists of a 2 nm Au layer deposited on top of the SiOx substrate and fragments of the tri-layer and PP. The thickness of the Au layer was estimated knowing the volume of a single Au nano-ring and the Au nano-rings surface density. At this thickness the Au layer are far from perfect as exemplified in Figure 6.8. Grooves in the Au layer appear. Although by UHV annealing at elevated temperatures (450 °C) the Au layer can be made atomically flat, the high temperature would destroy the PP. That is why no UHV annealing step was employed during samples preparation.

As observable in Figure 6.9, the DC SQUID measurements yield rather a large variation in magnetic moment response from the samples considered to be equivalent.

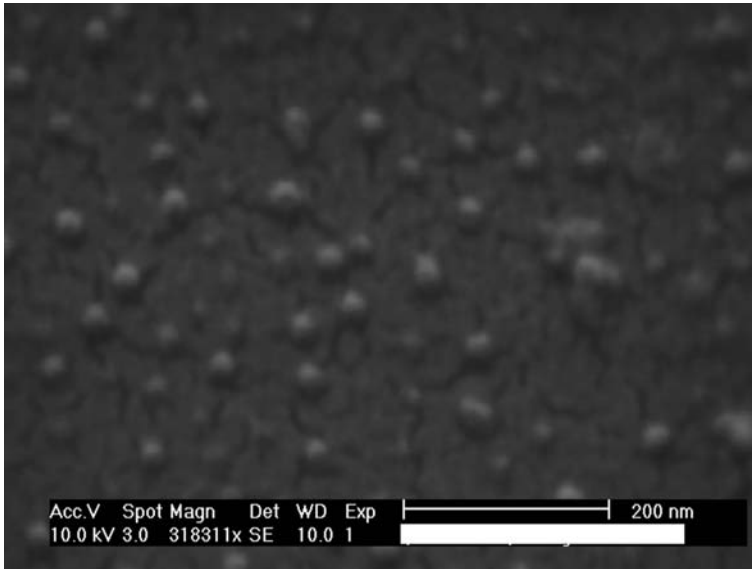


Figure 6.8: Scanning electron microscopy imaging of 8 nm thick Au layer on SiOx and PP.

The numbering of the samples is random, however sample 2 and 5 have been prepared in the same batch. Sample 6 presents a strong diamagnetic response when compared to sample 2 or sample 4 that appear to be slightly more diamagnetic than the reference sample. Samples 1 and 5 give a paramagnetic response while sample 3 appears to have a very weak paramagnetic signal. At 3.5 T sample 3 presents a kink from the linear dependency observable. This should be regarded as a measurement error since it is the only sample that did not presented a linear dependence. Samples 2 and 4 are more diamagnetic when compared to the reference sample with a relative variation of 3 to 6.5 %.

If it is assumed that the reference sample defines the total diamagnetic contribution expected from the substrate (Si+SiOx) and the thin Au layer. Subtracting the diamagnetic contribution, the magnetic measurement results can be made clearer as in Figure 6.10.

6.5 Discussion

Figure 6.10 clearly shows that DC SQUID measurements do not yield similar results for various samples prepared as much as possible in a similar manner. Unfortunately, at this stage of our research it is extremely difficult to draw conclusions regarding the

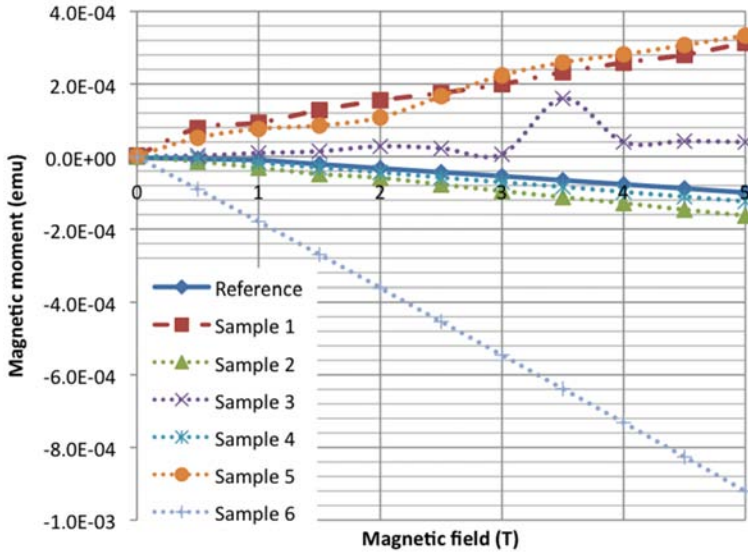


Figure 6.9: DC SQUID measurements of six samples with Au nano-rings and reference sample.

magnetic response of Au nano-rings. However, several interpretations are given. Of course, future work might validate or provide a different explanation to the results presented in this chapter.

One has to consider that AFM is a very localized technique for surface investigation. The maximum scan range available was $100 \times 100 \mu\text{m}^2$. However the sample surface size is roughly two thousand times bigger than the scan size. Clearly, it is impossible to state that the sample has on all its surface only the typical ring structures as depicted in Figure 6.4 or Figure 6.5. Within the same sample, some of the regions presented less dense Au nano-structures while other regions presented intricate dense Au structures (not necessarily rings). Decreasing the surface size can increase the sample homogeneity. However, decreasing the surface size will further complicate the already complex sample preparation procedure. For this reason, smaller samples have not been investigated by DC SQUID. One might consider preparing the Au rings directly on the cantilever used in the cantilever magnetometry technique, a valuable technique that could be able to detect the PC signature arising from the Au nanorings.

Sample contaminations with paramagnetic or ferromagnetic materials can also yield the broad dispersion of samples when studied with DC SQUID. For this purpose, two samples prepared in the same batch have been studied. Both samples have been

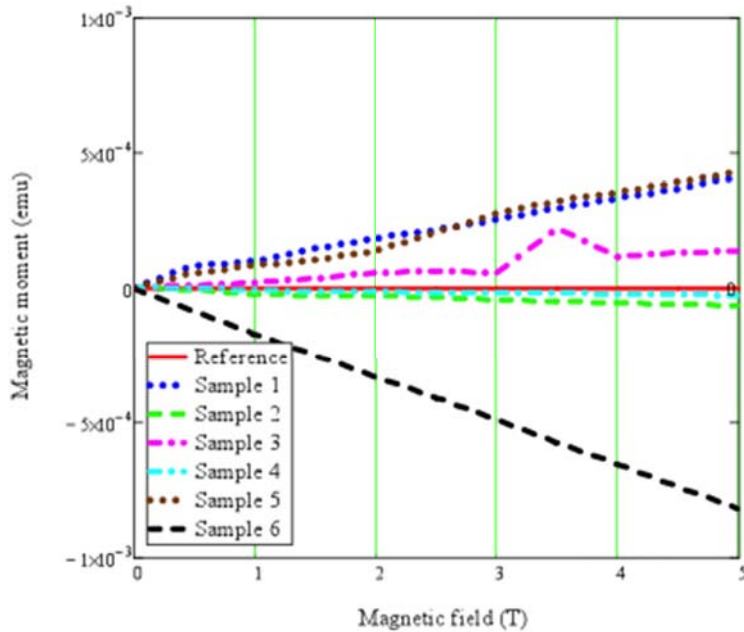


Figure 6.10: Magnetic moment measured from the six samples after the diamagnetic contribution was subtracted.

exposed to the exact same environment up to the point of insertion into the DC SQUID setup. The samples under discussion are samples number 2 and number 5, Figure 6.10. Since both samples under discussion have been prepared in exactly the same environment, have been prepared with the same glasswork, manipulated with the same tweezers, etc., sample contamination with para/fero magnetic materials can be excluded.

As recently suggested by, Smolyaninov et al. [16,17], surface plasmons influence the magnetic properties of mesoscopic metallic samples such as, in our case, nanorings. As an example, they shows for a thin Au layer that the Pauli paramagnetic contribution is equal to the surface plasmon vacuum diamagnetic contribution if the thickness of a thin gold layer deposited on an insulating surface is 2 nm. In addition, Smolyaninov predicts that for a thickness of the Au layer of 6 nm, the Landau diamagnetic contribution equals the plasmon vacuum diamagnetism. Reich et. al. [18] report on direct magnetization measurements performed on gold thin films (27 nm thick) deposited on polypropylene and Pyrex at 5 K and RT. It was found that at 5 K the magnetic response varies as function of substrate, yielding a strong paramagnetic response when the thin Au layer is deposited on Pyrex. Pyrex contains roughly 70%

silicon oxide. Furthermore, at RT, the magnetic response of a bulk sample of Au was of the same order as the noise level (10^{-6} emu).

The work of Smolyaninov and Reich give insight in the complexity of the magnetic moment response of the samples under investigation. First of all, the 25 mm^2 samples are rather difficult to fully characterize at a nanoscale. It is extremely difficult to make a 1:1 relationship between the structures present on the surface sample and the DC SQUID measurement results of the entire sample. Nonetheless, Smolyaninov calculates that the paramagnetic to a diamagnetic shift in the sample's magnetic moment response can be attributed to a variation of several nanometers of the gold layer thickness. Interestingly enough, under the assumption that Figure 6.5 correctly reproduces the Au nano-structures density than the Au enclosed within the structures would cover the sample with a 2 nm thin Au layer. Under these findings it is possible to explain the large variation between samples. For example, if the sample sputtering process is not removing all the Au in between the nanostructures, it is possible that a thin Au layer might still be present. This thin gold layer may create a shift in the magnetic response from paramagnetic to diamagnetic. In addition, plasmon modes of individual rings may couple. The surface plasmon wavelengths can be roughly estimated as $\lambda_p \sim L/n$, where L is the perimeter of the ring. Under the assumption that the ring diameter is 18 nm than the plasmon field decay outside the ring is 9 nm. Although difficult to achieve with AFM a lateral resolution of several nanometers, given Figure 6.5 one can speculate over the distance between Au structures and might assume in future calculations that plasmon coupling will alter the expected theoretical values of the ensemble magnetic moment.

6.6 Conclusions and remarks

Colloidal lithography technique was successfully used to create tens, hundreds of squared micrometers of well dispersed gold nano-structures. It was estimated that a region of $1 \times 1 \mu \text{ m}^2$ contains about 500 rings with a diameter varying between 12 nm and 26 nm. The large surface size of a single sample may contain up to 10^9 Au nano-structures. When large arrays of Au nanostructures are desired, the technique proves to be fast in comparison to traditional photolithography, in addition yielding smaller structures. However several limitations has been observed. First, the large number of preparation steps and the importance of each preparation step impose strict preparation procedures, recipes and chemical solutions. Second, the large PP diameter dispersion induces large variation in the Au nanostructure size. A better PP diameter definition would reduce the number of variables with one when true ensemble persistent current measurements would be pursued. Moreover contaminants on the

6. Towards persistent current measurements on nanoscopic gold rings

sample surface are in the Au nano structure is expected to be higher than for Au nano-structures prepared with, for e.g. the photolithographic technique.

The DC SQUID measurements yield a large variation in sample magnetic moment, from diamagnetic to paramagnetic. We propose that the most probable source of this behavior is given by the surface plasmons influence over the magnetic properties of mesoscopic metallic samples. To better understand and validate this expected variation of the magnetic moment function of thin metal thickness, dedicated experiments must be performed. In addition, one would first measure a possible signature of the persistent current starting from a single isolated Au ring. As previously mentioned, to our knowledge, this fabrication technique is the first one being able to produce Au rings where the electron should approach ballistic conduction regime. Persistent current measurements on ensemble of Au nano-rings would follow and hopefully bridge the gap between theory and experiment.

Bibliography

- [1] M. Buttiker, Y. Imry, R. Landauer, and S. Pinhas. *Phys. Rev. B* 31, 6207 (1985).
- [2] L.P. Lévy, G. Dolan, J. Dunsmuir, and H. Bouchiat. *Phys. Rev. Lett.* 64, 2074 (1990).
- [3] V. Chandrasekhar, R.A. Webb, M.J. Brandy, M.B. Ketchen, W.J. Gallagher, and A. Kleinsasser. *Phys. Rev. Lett.* 67, 3578 (1991).
- [4] B. Reulet, M. Ramin, H. Bouchiat, and D. Mailly. *Phys. Rev. Lett.* 75, 124 (1995).
- [5] E.M.Q. Jariwala, P. Miahanty, M.B. Ketchen, and R.A. Webb. *Phys. Rev. Lett.* 86, 3124 (2001).
- [6] W. Rabaut, L. Saminadayar, D. Mailly, K. Hasselbach, A. Benot, and B. Etienne. *Phys. Rev. Lett.* 102, 136802 (2009).
- [7] R. Deblock, R. Bel, B. Reulet, H. Bouchiat, and D. Mailly. *Phys. Rev. Lett.* 89, 206803 (2002).
- [8] D. Mailly, C. Chapelier, and A. Benoit. *Phys. Rev. Lett.* 70, 2020 (1993).
- [9] M. Buttiker, Y. Imry, and R. Landauer. *Phys. Lett. A* 96, 365 (1983).
- [10] H. Bluhm, N.C. Koshnick, J.A. Bert, M.E. Huber, and K.A. Moler. *Phys. Rev. Lett.* 102, 136802 (2009).
- [11] A.C. Bleszynski-Jaych, W.E. Shanks, B. Peaudecerf, E. Ginossar, F. von Oppen, L. Glazman, and J.G.E. Harris. *Science* 362, 272 (2009).

- [12] P. Hanarp and J. Aizpurua. *Phys. Rev. Lett.* 90, 057401 (2003).
- [13] www.sigmaaldrich.com
- [14] www.reheis.com
- [15] www.idclatex.com
- [16] I.I. Smolyaninov, C.D. Davis, V.N. Smolyaninova, D. Schaefer, J. Elliott, and A.V. Zayats. *Phys. Rev. B* 71, 035425 (2005).
- [17] I.I. Smolyaninov. [arXiv:cond-mat/0308507v1](https://arxiv.org/abs/cond-mat/0308507v1).
- [18] S. Reich, G. Leitus, and Y. Feldman. arxiv.org/pdf/cond-mat/0606375

Summary

Tailoring the electronic structure properties of carbon based materials

Graphene, a two-dimensional layer of carbon atoms arranged in a honeycomb lattice is the building block of graphite, carbon nanotubes and fullerenes. Prototypes of graphene electronic devices have been already made in various laboratories worldwide, outperforming the conventional semiconductor transistor technology. However, at this point, the lack of a true energy gap in graphene makes the integration of such electronic devices in commercial products (e.g. computers) impossible. It is well established that structural defects or adsorbents lead to a local change in the density of states of materials. This work describes and quantifies the role of chemisorbed atoms on the local density of states carbon based materials, such as graphite and carbon nanotubes as a function of material dimensionality. The thesis first presents a general introduction, followed by two chapters related to more specific theoretical and experimental knowledge on the subjects discussed in the thesis.

Highly Oriented Pyrolytic Graphite (HOPG) has been extensively studied over the last decades but the role of structural defects and/or chemisorbed species on its electron local density of states (LDOS) has not been well understood. Chapter four is focused on characterizing the LDOS of HOPG after chemisorption of hydrogen and deuterium atoms using a scanning tunneling microscope. The electronic structure study was performed in the temperature regime of 4 K to 120 K and as a function of hydrogen coverage on HOPG. The results show that the LDOS of HOPG is reduced around the formed H-islands. If the hydrogen coverage is relatively large and the sample temperature is low (4 K), an energy gap is observed. However, for low hydrogen concentrations and hence smaller H-islands, the LDOS at the Fermi-level has an unexpected Fano-lineshape, indicating that localized electron states of HOPG character are coupled to continuum states such as phonons. At low temperatures, the LDOS at the Fermi-level is reduced over a larger spatial region around the H-islands compared to the high H-coverage case.

Since their discovery, carbon nanotubes have attracted the interest of both fundamental and applied research due to some interesting physical properties like: the elastic modulus, the tensile strength, the high thermal conductivity and the ballistic conduction regime. Single walled carbon nanotubes (SWCNT) can be semiconduct-

6. Summary

ing or metallic depending on their chirality which is reflected in the DOS. In the quest for understanding the influence of chemisorbed species on the LDOS of carbon based materials, chapter five summarizes the results obtained on hydrogen decorated metallic SWCNT. It has been observed that upon hydrogenation, metallic SWNCTs can become locally semiconducting. Furthermore, for a short section (delimited by hydrogen patches) of a metallic SWCNT quantum confinement of electrons has been measured. The results obtained for both carbon-based materials upon hydrogenation are compared in the last part of this chapter.

Chapter six of the thesis is aimed at examining the possibility of measuring persistent currents on an ensemble of gold nano-rings prepared by a colloidal lithography method. This method allows the preparation of metallic nanostructures bringing the system more towards the ballistic conduction regime, which facilitates the comparison between theory and experiment. Although persistent current measurements were not performed, the magnetic response of the various prepared samples is intriguing. The origin of largely varying magnetic responses is not fully understood yet but the observations hint to peculiar magnetic behavior of thin metallic film deposited on insulating substrates.

Samenvatting

Grafeen, een enkellaagsvlak van koolstofatomen in een honingraatrooster, is de bouwsteen van grafiet, koolstof nanobuizen en fullerenen. Wereldwijd zijn in diverse laboratoria prototypen van grafeen transistors gerealiseerd die de werking van transistors gebaseerd op conventionele halfgeleidertechnologie overtreffen. Het gebrek aan een echte bandkloof in grafeen maakt de integratie van grafeen transistors in commerciële toepassingen (bijv. computers) onmogelijk. Het is bekend dat structuurdefecten of adsorbenten aanleiding geven tot een lokale verandering van de toestandsdichtheid in materialen. Dit proefschrift beschrijft en kwantificeert de rol van chemisch geadsorbeerde atomen op de lokale toestandsdichtheid van koolstofgebaseerde materialen zoals grafiet en koolstof nanobuizen als functie van de dimensionaliteit van het materiaal. Het proefschrift geeft eerst een algemene inleiding, gevolgd door twee hoofdstukken die gerelateerd zijn aan de specifieke theoretische en experimentele achtergrond met betrekking tot de onderwerpen die in het proefschrift aan bod komen.

Hoog geordend pyrolytisch grafiet (HOPG) is in de afgelopen jaren uitgebreid bestudeerd, maar de rol van structuurdefecten of van chemisch geadsorbeerde atomen op de lokale toestandsdichtheid is niet goed begrepen. Hoofdstuk vier beschrijft de karakterisering van de lokale toestandsdichtheid van HOPG na chemisorptie van waterstof- en deuteriumatomen met rastertunnelmicroscopie. De elektronische structuur is bestudeerd in een temperatuursbereik van 4 tot 120 K en als functie van de hoeveelheid waterstof geadsorbeerd op HOPG. De resultaten tonen aan dat de lokale toestandsdichtheid afneemt rond de gevormde waterstofeilanden. Bij een hoge bedekking met waterstofatomen en bij lage temperatuur (4 K) wordt een bandkloof waargenomen. Bij een lage bedekking en dus kleinere waterstofeilanden heeft de lokale toestandsdichtheid aan het Fermi-niveau een Fano-lijnform die aangeeft dat gelokaliseerde elektronische toestanden van HOPG gekoppeld zijn aan continuumtoestanden zoals fononen. Bij lage temperaturen wordt de afname van de lokale toestandsdichtheid bij het Fermi-niveau over een groter ruimtelijk gebied rond de waterstofeilanden waargenomen dan bij een hoge waterstofbedekking.

Sinds hun ontdekking hebben koolstof nanobuizen de aandacht getrokken in fundamenteel en toegepast onderzoek vanwege een aantal interessante fysische eigenschappen zoals: de elasticiteitsmodulus, de treksterkte, de hoge warmtegeleiding en ballistische geleiding. Enkelwandige koolstof nanobuizen (SWCNT) kunnen halfgeleidend of metallisch zijn afhankelijk van hun chiraliteit die tot uitdrukking komt in de toestandsdichtheid. Opzoek naar de invloed van chemisch gebonden deeltjes op de lokale toestandsdichtheid van koolstofgebaseerde materialen, beschrijft hoofd-

6. Samenvatting

stuk vijf de resultaten die verkregen zijn voor waterstof geadsorbeerd op metallische koolstof nanobuizen. Na hydrogenering worden de metallische koolstof nanobuizen lokaal halfgeleidend. Voorts is voor een klein stukje van een metallische koolstof nanobuis (ingeklemd tussen twee waterstof eilanden) kwantum opsluiting van elektronen waargenomen. In het laatste deel van hoofdstuk vijf worden de resultaten van chemisorptie van waterstof op grafiet en koolstof nanobuizen met elkaar vergeleken.

Hoofdstuk zes van het proefschrift is gericht op het bestuderen van de mogelijkheid om persisterende stroom te meten aan een verzameling van goud nanoringen die gemaakt zijn met collodale lithografie. Deze methode maakt het mogelijke metallische nanostructuren te maken die het systeem dichterbij het ballistische regime brengen, waar theorie en experiment beter met elkaar vergeleken kunnen worden. Ofschon persisterende-stroommetingen niet uitgevoerd zijn, is de magnetische respons van de diverse gemaakte structuren intrigerend. De oorzaak van de sterke verschillen in magnetische eigenschappen is niet goed begrepen, maar de waarnemingen suggereren bijzondere magnetische eigenschappen van dunne metallische films op isolerende substraten.

Acknowledgements

It has been an honor and a privilege to be an M2N-er. I met the Molecular Materials and Nanosystems group during my six-month internship at the Eindhoven University of Technology. The dedication, enthusiasm, friendliness, diversity and ambiance experienced in the M2N group strongly motivated me to start my PhD studies with the group. Now, as it ends, I would like to seize the opportunity and thank you all.

First, I would like to express my appreciation for my supervisor, Dr. Kees Flipse. Thank you for giving me the opportunity to work with you, to learn from you and to grow under your guidance. I will never forget your enthusiasm for the new and the undiscovered, as I will not forget your kindness. Your drive and constant support helped me tackle and understand the challenging experimental results obtained throughout my PhD studies. Once again, thank you.

Always busy, yet always available, to my copromotor, Prof. Dr. René Janssen, I would like to thank for the extensive help provided during my PhD. Thank you for the many hours spent correcting and improving the manuscript. You have always succeeded in bridging the gap between Physics and Chemistry and taught me that nowadays you can hardly do one without the other. I can only hope that the chance you gave me to be a part of your group was put to good use.

Some of the results presented in this thesis have been obtained with setups of other groups from the TU/e. I would like to thank Marc van Maris (Mechanical Engineering) for the SEM experiments and for allowing me to use their AFM setup. I am grateful to Reinoud Lavrijsen for performing the SQUID measurements. Many thanks go to Prof. Dr. Hidde Brongersma for fruitful discussions and experiments related to hydrogen production by RF plasma ion source. Special thanks go to Friso Wittebrood and Yingxin Liang for their hard work on H/CNT. With their help I was able to study the effect of chemisorbed hydrogen on carbon-based materials in 3D and 1D. I am grateful for the theoretical support provided by Ž. Šljivančanin (EPFL). I am particular grateful to Prof. M.I. Katsnelson for his theoretical support related to Chapters 4 and 5.

I would like to express my gratitude to the core committee members who provided me with insightful comments during review of the manuscript.

For four years Rik van Laarhoven has been a great office colleague. I will never forget our exchange of ideas regarding life-cars-sports-gadgets-office pets and some unmentionables. Did the table golf catch on? Once again, thank you Rik. I would also like to thank Jiří Červenka for the wonderful time during the six years overlap and for the fruitful discussions. Joris, I would like to thank you for all your support with

6. Acknowledgements

the LT STM and for your refined sense of humor. During my internship and a part of my PhD, George Tănasă has helped me in countless occasions, thank you! Special thanks also go to Oleg Kurnosikov for always extending a helping hand. I would also like to thank Martijn Kemerink and Reinder Coehoorn for the group meeting discussions.

The experiments have been greatly supported by Gerard Wijers and Wijnand Dijkstra. Without you, our experimental setups would have never produced results. Thank you for your promptitude and expertise. Fruitful discussions or not, Rein Rumphorst has always managed to be interesting and challenging. From electronics to Sneeuwkapje, I had fun and learned a little bit of Dutch. Hartelijk bedankt Rein en tot ziens!

As mentioned, the M2N group was outstanding. I would like to thank Erwin Rossen, Kevin van de Ruit, Ron Willems, Erik Roeling, Siebe van Mensfoort, Klára Maturová, Jean-Michel Wulveryck, Juan Amir, Marco de Ridder, Hans Gommans, Frank Janssen, Alexander Nardes, Dimitri Charrier, Marco Carvelli and Cristina Popa for all the pleasant moments we shared.

I would like to express my gratitude to Prof. Dr. Dumitru Luca from the University Al. I. Cuza, Iași, Romania, for giving me the chance to do my internship at M2N, TU/e.

Special thanks to NanoNED for the financial support, a wonderful Dutch network for science and technology.

To my parents, Dumitru and Viorica I would like to thank for helping me become the person I am today. Vă mulțumesc!

Most importantly, I would like to thank my wife Andreea for all the happiness and support she brought into my life.

Curriculum Vitae

- December 6 1979 Born in Iasi, Iasi county, Romania
- 1994 Graduated from Gymnasium Vasile Conta , Iasi
- 1998 Graduated from Grup Scolar Tehnic Cuza Voda , Iasi
- 1998 - 2004 M.Sc. in Plasma Physics, Al. I. Cuza University, Iasi. Researcher at the National Institute of Research and Development for Technical Physics, Iasi
- Traineeship at the group of Molecular Materials and Nanosystems (M2N) of the department of Applied Physics, Eindhoven University of Technology, The Netherlands. Subject: *Single molecule conductance measurements - bridging the gap*, supervised by Dr. Ir. C.F.J. Flipse and Prof. Dr. Ir. R.A.J. Janssen.
- Master thesis project at the group of Plasma Physics, Faculty of Physics, Al. I. Cuza University, Iasi. Subject: *Au nanoparticle manipulation by atomic force microscopy*, supervisor: Prof. Dr. D. Luca.
- 2004 - 2009 PhD project at the group of Molecular Materials and Nanosystems (M2N) of the department of Applied Physics, Eindhoven University of Technology, The Netherlands. Subject: *Tailoring the electronic structure properties of carbon based materials*, supervised by Dr. Ir. C.F.J. Flipse and Prof. Dr. Ir. R.A.J. Janssen.
- 2009 - Present Accelerator physicist at High Voltage Engineering Europa B.V., Amersfoort, The Netherlands.

